

## ABSTRACT

Title of Dissertation: A STUDY OF REMOTELY SENSED  
AEROSOL PROPERTIES FROM GROUND-  
BASED SUN AND SKY SCANNING  
RADIOMETERS

David M. Giles, Doctor of Philosophy, 2012

Directed By: Professor Russell R. Dickerson and  
Professor Anne M. Thompson,  
Department of Atmospheric and Oceanic Science

Aerosol particles impact human health by degrading air quality and affect climate by heating or cooling the atmosphere. The Indo-Gangetic Plain (IGP) of Northern India, one of the most populous regions in the world, produces and is impacted by a variety of aerosols including pollution, smoke, dust, and mixtures of them. The NASA Aerosol Robotic Network (AERONET) mesoscale distribution of Sun and sky-pointing instruments in India was established to measure aerosol characteristics at sites across the IGP and around Kanpur, India, a large urban and industrial center in the IGP, during the 2008 pre-monsoon (April-June). This study focused on detecting spatial and temporal variability of aerosols, validating satellite retrievals, and classifying the dominant aerosol mixing states and origins. The Kanpur region typically experiences high aerosol loading due to pollution and smoke during the winter and high aerosol loading due to the addition of dust to the pollution and smoke mixture during the pre-monsoon. Aerosol emissions

in Kanpur likely contribute up to 20% of the aerosol loading during the pre-monsoon over the IGP. Aerosol absorption also increases significantly downwind of Kanpur indicating the possibility of the black carbon emissions from aerosol sources such as coal-fired power plants and brick kilns. Aerosol retrievals from satellite show a high bias when compared to the mesoscale distributed instruments around Kanpur during the pre-monsoon with few high quality retrievals due to imperfect aerosol type and land surface characteristic assumptions. Aerosol type classification using the aerosol absorption, size, and shape properties can identify dominant aerosol mixing states of absorbing dust and black carbon particles. Using 19 long-term AERONET sites near various aerosol source regions (Dust, Mixed, Urban/Industrial, and Biomass Burning), aerosol absorption property statistics are expanded upon and show significant differences when compared to previous work. The sensitivity of absorption properties is evaluated and quantified with respect to aerosol retrieval uncertainty. Using clustering analysis, aerosol absorption and size relationships provide a simple method to classify aerosol mixing states and origins and potentially improve aerosol retrievals from ground-based and satellite-based instrumentation.

A STUDY OF REMOTELY SENSED AEROSOL PROPERTIES FROM GROUND-  
BASED SUN AND SKY SCANNING RADIOMETERS

by

David M. Giles

Dissertation submitted to the Faculty of the Graduate School of the  
University of Maryland, College Park, in partial fulfillment  
of the requirements for the degree of  
Doctor of Philosophy  
2012

Advisory Committee:

Professor Russell R. Dickerson, Chair/Advisor

Professor Rachel T. Pinker

Professor Ross J. Salawitch

Professor Anne M. Thompson, Co-Advisor

Mr. Brent N. Holben, Research Advisor

Professor Kaye L. Brubaker, Dean's Representative

© Copyright by  
David M. Giles  
2012

## Preface

This document contains original scientific content produced by the author and collaborators. Significant scientific findings were reached by:

- Analyzing measurements and retrievals from ground-based Sun/sky scanning radiometers distributed around Kanpur, India, to show detectable changes in aerosol properties and quantify increases in aerosol concentration attributed to emissions from the Kanpur region with respect to the background pollution and dust in the Indo-Gangetic Plain (IGP). (Chapter 2: *Giles et al.*, 2011)
- Validating 3 km and 10 km MODIS retrievals and AERONET measurements of aerosol loading over Kanpur and the surrounding IGP in the midst of complex land surface brightness and mixed aerosol types during the pre-monsoon (April-June). (Chapter 3: *Giles et al.*, 2011)
- Demonstrating that the aerosol absorption and particle size relationship can estimate the dominant absorbing aerosol type in Kanpur. Analysis shows the spectral single scattering albedo (SSA) varies smoothly with changing aerosol types (i.e., from dust to black carbon). (Chapter 4: *Giles et al.*, 2011)
- Comparing the aerosol absorption at AERONET sites worldwide located near aerosol source regions shows significant differences compared to previous work (up to 0.02 SSA) and reveals that aerosol mixtures (e.g., dust and black carbon) exhibit stronger spectral absorption and increased dominance of absorbing carbonaceous particles than for dust alone. (Chapter 5: *Giles et al.*, 2012)
- Analyzing absorption Ångström exponent (AAE) for Urban/Industrial pollution and Biomass Burning smoke shows similar distributions and the analysis shows approximately 10% of the retrievals had AAE values below 1.0 for most categories but as high as 22% for Urban/Industrial. (Chapter 5: *Giles et al.*, 2012)
- Performing a sensitivity study by perturbing the SSA shows significant AAE changes (up to  $\pm 0.6$ ) and quantifies the improvement of AAE resulting from reducing the SSA uncertainty. (Chapter 5: *Giles et al.*, 2012)
- Comparing the results of a cluster analysis for aerosol absorption and size relationships that show at least five distinct aerosol type clusters [Dust, Mixed-Large Particle, Mixed-Small Particle, Urban/Industrial, and Biomass Burning (with two sub-clusters)]. (Chapter 5: *Giles et al.*, 2012)

Published papers based on this work:

Giles, D. M., et al. (2011), Aerosol properties over the Indo-Gangetic Plain: A mesoscale perspective from the TIGERZ experiment, *J. Geophys. Res.*, *116*, D18203, doi:10.1029/2011JD015809. Copyright 2011 American Geophysical Union.

Giles, D. M., B. N. Holben, T. F. Eck, A. Sinyuk, A. Smirnov, I. Slutsker, R. R. Dickerson, A. M. Thompson, and J. S. Schafer (2012), An Analysis of AERONET Aerosol Absorption Properties and Classifications Representative of Aerosol Source Regions, *J. Geophys. Res.*, *117*, D17203, doi:10.1029/2012JD018127. Copyright 2012 American Geophysical Union.

## **Dedication**

To my wife, Lauren, and children, Amanda and Evan, who gave their love, affection, and support allowing me to reach this milestone.

To my parents, sister, grandparents, and family, who gave me the opportunity to pursue my goals and offered encouragement through the years.

## Acknowledgements

I would like to thank my two advisors, Dr. Russell Dickerson and Dr. Anne Thompson, for their suggestions, feedback, and guidance with respect to developing content, analysis, and figures for the dissertation and support throughout my graduate career. I would also like to thank Brent Holben (NASA/GSFC) and my current and former employers (Sigma Space Corporation and SSAI) for allowing me the opportunity to achieve graduate degrees in combination with my efforts on the NASA AERONET project. Further, I would like to thank Brent Holben, Thomas Eck, Ilya Slutsker, Aliaksandr Sinyuk, and Alexander Smirnov for many lengthy and constructive discussions about aerosols and AERONET data. I also thank the AERONET team for calibrating and maintaining instrumentation and processing these data.

I would like thank all of the more than 30 participants and collaborators in the NASA/GSFC TIGERZ experiment including many Indian researchers and graduate students as well as other national and international agencies providing personnel and equipment to perform the study. I would like to thank Dr. Jeffrey Reid and Dr. Philip Russell for providing peer-reviewed journal article comments on portions of this study.

I would like to thank Vanderlei Martins for use of the scanning electron microscope (SEM) at the University of Maryland-Baltimore County and Adriana Lima for assisting in performing the SEM imaging of Kanpur filters collected during the TIGERZ experiment.

I would like to thank the following principal investigators and their staff for maintaining the following sites and for use of these data in this study: Didier Tanre (Banizoumbou, Capo Verde, Dakar, and Ouagadougou), Naif Al-Abbadi (Solar Village), Rachel Pinker (Ilorin), Sachi Tripathi and Ramesh Singh (Kanpur), Arnon Karnieli (SEDE BOKER), Pucui Wang (XiangHe), Giuseppe Zibordi (Ispra), Amando L. Contreras (Mexico City), Alexander Aculinin (Moldova), Itaru Sano (Shirahama), Paulo Artaxo (Abracos Hill and Alta Floresta), John Vande Castle (Bonanza Creek), and Ross Mitchell (Lake Argyle).

I gratefully acknowledge the NOAA Air Resources Laboratory (ARL) for the provision of the HYSPLIT transport and dispersion model and/or READY website (<http://www.arl.noaa.gov/ready.php>) used in this publication.

Portions of Chapter 1 and Chapter 6.1 were reproduced with modifications from *Giles et al.* [2011, 2012]. Chapters 2, 3, and 4 were reproduced with modifications from *Giles et al.* [2011]. Chapter 5 was reproduced with modifications from *Giles et al.* [2012]. *Giles et al.* [2011, 2012] are reproduced by permission of the American Geophysical Union.

## Table of Contents

Preface.....	ii
Dedication.....	iii
Acknowledgements.....	iv
List of Tables.....	vi
List of Figures.....	vii
Chapter 1: Introduction.....	1
1.1 Motivation.....	1
1.2 Aerosol and Water Vapor Properties from Collimated Solar Measurements.....	3
1.3 Aerosol Properties Using Almuqantar Sky Radiance Measurements.....	9
1.4 TIGERZ Experiment in the Indo-Gangetic Plain.....	11
1.5 Scientific Objectives and Outline of Dissertation.....	16
Chapter 2: Aerosol Properties in Kanpur during TIGERZ.....	18
2.1 Motivation and Methodology.....	18
2.2 Aerosol Variability and Transport over Kanpur, India.....	20
2.3 Comparison of Microtops and AERONET.....	25
2.4 Spatial and Temporal Variability of AOD.....	26
2.5 Spatial and Temporal Variability of Absorption and Size Properties.....	30
Chapter 3: Evaluation of MODIS over Kanpur during TIGERZ.....	34
3.1 Motivation.....	34
3.2 Analysis Technique.....	36
3.3 Comparison of MODIS and AERONET.....	36
Chapter 4: Dominant Absorbing Aerosol Types over Kanpur.....	44
4.1 Motivation.....	44
4.2 Aerosol Absorption and Size Relationships.....	45
4.3 Absorption Wavelength Dependence Effects on Aerosol Properties.....	48
Chapter 5: Classifications of Aerosol Dominant Mixing States and Origins.....	53
5.1 Motivation.....	53
5.2 Methodology.....	55
5.3 Climatology of Aerosol Absorption Properties.....	59
5.4 Sensitivity of Absorption Ångstrom Exponent to Single Scattering Albedo.....	70
5.5 Cluster Analysis of Absorption and Size Properties.....	75
Chapter 6: Summary, Conclusions, and Future Work.....	83
6.1 Summary and Conclusions.....	83
6.2 Future Work.....	86
Bibliography.....	89

## List of Tables

Table 1.1 Instrument inventory and availability during the 2008 TIGERZ IOP.....	14
Table 2.1 Mesoscale deployment day area averages of aerosol properties for coincident measurement periods .....	30
Table 2.2 Area-averaged aerosol volume size distribution quantities for fine mode ( <i>f</i> ) and coarse mode ( <i>c</i> ) aerosols on 30 May 2008.....	33
Table 3.1 Potential and actual MODIS, AERONET Level 2.0 (L2), and Level 2.0 + Level 1.0 screened (L2+L1) matchups from 1 May to 23 June 2008.....	42
Table 5.1 Previous studies identifying regional aerosol sources affecting AERONET sites. ....	57
Table 5.2 Average aerosol absorption and size properties by aerosol type category from AERONET Version 2 almucantar retrievals.....	64
Table 5.3 Sensitivity of the absorption Ångström exponent ( $\alpha_{\text{abs}}$ ) to perturbations of single scattering albedo ( $\omega_0$ ) for each dominant aerosol particle type.....	73

## List of Figures

Figure 1.1 Cimel Sun/sky Radiometers deployed in Kanpur, India. ....	5
Figure 1.2 Atmospheric flow originating over the Thar Desert, Arabian Sea, and Bay of Bengal is restricted by the Himalayan Mountains to the north of the Indo-Gangetic Plain (IGP) allowing aerosols to accumulate here. Map (a) shows the regional distribution of Cimel sites within the IGP and map (b) shows the distribution of sites around Kanpur, India (26.51°N, 80.23°E). ....	15
Figure 2.1 The 2001-2009 Kanpur multi-year monthly averages are plotted for aerosol optical depth and water vapor (a,e) and spectral deconvolution algorithm (SDA) retrievals (b-d) at the Level 2.0 quality level. ....	21
Figure 2.2 The NOAA HYSPLIT 3-day back trajectory analyses are shown for Kanpur, India (26.51°N, 80.23°E). ....	22
Figure 2.3 Fossil fuel aerosol sources, such as the coal-fired Panki power plant (top panel) and a coal-fired mix of agricultural waste and/or wood in a Bull's Trench kiln (bottom panel), emit black carbon particles and precursor gases (e.g. nitrogen oxides and sulfur dioxide) to form nitrates and sulfates contributing to aerosol loading in the atmosphere over Kanpur, India. ....	24
Figure 2.4 Cimel and Microtops aerosol optical depth at 500 nm ( $\tau_{500\text{nm}}$ ) measurements were compared to an arbitrary Cimel #83 (C83) at IIT-Kanpur between 05:19 UTC and 05:49 UTC on 25 May 2008, and ranged within the stated uncertainty. ....	26
Figure 2.5 Substantial day-to-day variation of aerosol loading occurred during the TIGERZ IOP possibly due to dust transport, dry deposition, and precipitation. Aerosol optical depth (AOD) daily averages of AERONET Level 2.0 are plotted for IIT-Kanpur, India, from 1 May to 12 June 2008. ....	28
Figure 2.6 Data from TIGERZ IOP sites indicated spatially homogeneous, uniformly sized, spectrally absorbing pollution and dust particles. ....	32
Figure 3.1 Aqua MODIS Land Normalized Difference Vegetation Index (NDVI) 250 m product over the Indo-Gangetic Plain averaged between April 30 and May 15, 2008. ....	35
Figure 3.2 MODIS AOD retrievals with $QA \geq 0$ were biased high with respect to TIGERZ IOP area-averaged measurements. MODIS AOD 3 km retrievals improved spatial representativeness during some conditions (e.g., clouds) that prohibited the retrieval of 10 km products. Area-averaged MODIS (MOD04_L2/MYD04_L2) 3 km and 10 km $\tau_{550\text{nm}}$ versus area-averaged sun photometer (Cimel and Microtops) $\tau_{550\text{nm}}$ were compared for each temporary deployment. ....	38
Figure 3.3 MODIS AOD 10 km retrievals with the lowest quality assurance ( $QA \geq 0$ ) had moderate correlation with the Kanpur AERONET site, whereas retrievals with $QA > 0$ were limited in number over the semi-bright land surface. Area-averaged MODIS (MOD04_L2/MYD04_L2) 10 km $\tau_{550\text{nm}}$ versus Kanpur AERONET $\tau_{550\text{nm}}$ compared from 1 May to 9 June 2008, and partitioned for each QA level $\geq 0$ (a), $\geq 1$ (b), $\geq 2$ (c), and 3 (d) for the Terra MODIS, Aqua MODIS, and Aqua Deep Blue MODIS algorithms. ....	40
Figure 4.1 Level 2.0 absorption Ångström exponent ( $\alpha_{\text{abs}}$ ) and sphericity fraction as a function of extinction Ångström exponent ( $\alpha_{\text{ext}}$ ) and fine mode fraction of AOD at	

675 nm ( $\eta_{675\text{nm}}$ ; from the almucantar inversions) from the Kanpur AERONET record (2002-2008) in all seasons (a,c) and April-May-June (b,d).....	48
Figure 4.2 Scanning electron microscope image analyzed using filter samples taken at IIT-Kanpur on 10 May 2008.....	50
Figure 4.3 As absorption Ångström exponent decreased to 1.0, coarse mode particles became less dominant for both the annual cycle and pre-monsoon. Further, single scattering albedo transitioned from spectra representing dust (i.e., typical iron oxide absorption in the blue wavelength region and relatively weak absorption in the near-infrared) to urban/industrial pollution containing black carbon (i.e., stronger absorption in longer wavelengths).....	51
Figure 4.4 Level 2.0 SSA data were averaged for $\alpha_{\text{abs}}$ bins and further partitioned based on $\alpha_{\text{ext}}$ and $\eta_{675\text{nm}}$ using Kanpur AERONET (2002-2008).....	52
Figure 5.1 Distribution of the AERONET sites based on the dominant particle type. Sites were selected based on data volume, geographic location, and primary aerosol source region. ....	56
Figure 5.2 Spectral single scattering albedo averages were grouped by dominant aerosol particle category for $\tau_{440\text{nm}} > 0.4$ using AERONET Version 2, Level 2.0 data. ....	61
Figure 5.3 Similar to Figure 5.2, except the spectral single scattering albedo averages for the Mixed category were grouped by fine mode fraction of AOD ( $\eta_{550\text{nm}}$ ) using the ranges 0.0-0.33 for coarse mode dominated particles (a), 0.33-0.66 for mixed size particles (b), and 0.66-1.0 for fine mode dominated particles (c). ....	67
Figure 5.4 Absorption aerosol optical depth ( $\tau_{\text{abs}}$ ) and absorption Ångström exponent ( $\alpha_{\text{abs}}$ ) averages were grouped by dominant aerosol particle category for $\tau_{440\text{nm}} > 0.4$ using AERONET Version 2, Level 2.0 data.....	68
Figure 5.5 Similar to Figure 5.3, except $\tau_{\text{abs}}$ and $\alpha_{\text{abs}}$ averages for the Mixed category were grouped by fine mode fraction of the AOD ( $\eta_{550\text{nm}}$ ) using ranges of 0.0-0.33 for coarse mode dominated particles (a), 0.33-0.66 for mixed size particles (b), and 0.66-1.0 for fine mode particles (c).....	69
Figure 5.6 Absorption Ångström exponent ( $\alpha_{\text{abs}}$ ) frequency distribution for individual retrievals partitioned by dominant aerosol particle using AERONET Version 2, Level 2.0 data. Approximately 10% of the $\alpha_{\text{abs}}$ retrievals (22% for Urban/Industrial) were below 1.0 or $\lambda^{-1}$ dependence. ....	71
Figure 5.7 Relative number density plots for the absorption Ångström exponent (440-870 nm) and extinction Ångström exponent (440-870 nm) relationship based on dominant aerosol type using AERONET Version 2, Level 2.0 data. ....	77
Figure 5.8 Similar to Figure 5.7, except for the absorption Ångström exponent (440-870 nm) and fine mode fraction of the aerosol optical depth (550 nm) relationship... ..	77
Figure 5.9 Similar to Figure 5.7, except for the single scattering albedo (440 nm) and the extinction Ångström exponent (440-870 nm) relationship.....	78
Figure 5.10 Similar to Figure 5.7, except for the single scattering albedo (440 nm) and fine mode fraction of the aerosol optical depth (550 nm) relationship.....	78
Figure 5.11 Weighted cluster averages were grouped for each aerosol type category and relationship using AERONET Version 2, Level 2.0 data.....	80

## Chapter 1: Introduction

*Reproduced by permission of American Geophysical Union.*

### 1.1 Motivation

Aerosols are particles suspended in the air—such as dust, carbon, sulfate, nitrate, sea salt or mixtures of them—that heat or cool the atmosphere to a significant degree of uncertainty. For example, according to the Intergovernmental Panel on Climate Change in 2007 [IPCC, 2007], the overall aerosol direct effect on radiative forcing ( $-0.5 \pm 0.4$   $\text{W/m}^2$ , a net cooling) has significant uncertainty with estimates ranging from near zero to  $\sim -0.1$ , which affects the net anthropogenic radiative forcing estimate where greenhouse gases (including  $\text{CO}_2$ ,  $\text{CH}_4$ ,  $\text{N}_2\text{O}$ , and halocarbons) dominate heating ( $+2.6 \pm 0.3$   $\text{W/m}^2$ ). Aerosols can also impact the hydrological cycle. Particles in the vicinity of clouds may have “indirect effects” acting as cloud condensation nuclei to change the cloud albedo [ $-0.7$  ( $-1.1$ ,  $+0.4$ )  $\text{W/m}^2$ , net cooling], cloud lifetime, and precipitation efficiency [IPCC, 2007]. Further, deposition of black carbon particles on snow pack and glaciers may possibly lead to a positive radiative forcing response ( $+0.1 \pm 0.1$   $\text{W/m}^2$ ) and accelerated melting [IPCC, 2007]. Aerosols in the lower troposphere degrade air quality and impact human health (e.g., respiratory disease), aesthetics, and transportation (e.g., reduced visibility) [Watson 2002; Menon *et al.*, 2002]. High aerosol loading also reduces the total solar radiation reaching Earth’s surface leading to solar dimming [Pinker *et al.*, 2005]. Depending on meteorological conditions, airborne particles typically have a lifetime in the atmosphere of up to a few hours to one or two weeks and they may travel large distances (up to thousands of kilometers). While aerosols are observed in the troposphere and stratosphere, the highest aerosol concentration is in the boundary layer of

the troposphere, which typically extends from the Earth's surface to about 3 km. High temporal and spatial observations are needed to properly quantify the magnitude of the aerosol properties with respect to concentration, size, type, and absorption to properly understand these aerosol impacts on regional and global scales.

Aerosol size and absorption can vary greatly depending on the origin of the aerosol. Weakly absorbing sulfates and nitrates and weakly to strongly absorbing carbonaceous particles (e.g., organic carbon or black carbon) have radii less than  $\sim 1 \mu\text{m}$  (i.e., the fine mode of the size distribution) resulting from varying fuel types (e.g., automobile exhaust, power plant emissions, or open burning of forest land), combustion phases (e.g., smoldering or flaming), and chemical and microphysical processes (e.g., humidification and aggregation). Sulfates and sea salt are hygroscopic and can grow in high humidity environments (e.g., leading to haze in summer or fog in winter), while aerosol particles may aggregate when transported away from the source (e.g., aged biomass burning smoke). Weakly absorbing sea salt and moderately absorbing iron-ore containing mineral dust have radii greater than  $\sim 1 \mu\text{m}$  (i.e., the coarse mode of the size distribution). Volcanic gas and ash eruptions can lead to a variety of aerosol sizes (e.g., coarse mode ash as well as small and large fine mode sulfates) producing trimodal volume size distributions and these volcanic aerosol particles can be dispersed over large distances (possibly globally) in the upper troposphere or lower stratosphere after extreme events such as Mount Pinatubo [McCormick *et al.*, 1995; Eck *et al.*, 2010].

Routine measurements on a global scale are needed to quantify aerosol properties. These measurements are performed utilizing passive or active remote sensing techniques. The NASA Aerosol Robotic Network (AERONET) was established to measure aerosol

properties in the early 1990s and continues to operate over 450 Sun/sky radiometers worldwide [Holben *et al.*, 1998; <http://aeronet.gsfc.nasa.gov>]. AERONET provides a freely available database of aerosol properties allowing for aerosol characterization, satellite validation, and aerosol transport model verification. The seasonal and multi-year variability of aerosol optical depth (AOD) and other aerosol properties have been characterized at long-term AERONET sites in or near aerosol source regions [Holben *et al.*, 2001; Dubovik *et al.*, 2002; Eck *et al.*, 2010]. Satellite passive remote-sensing measurements, such as the Moderate Resolution Spectroradiometer (MODIS) instrument on Terra and Aqua satellites, have utilized the AERONET data to validate aerosol retrievals over land and ocean surfaces [Levy *et al.*, 2007a]. Aerosol transport models, such as the Goddard Chemistry Aerosol Radiative Transport (GOCART) model, have used AERONET data for verification and evaluation [Chin *et al.*, 2009]. Globally distributed AERONET observations improve satellite retrievals and model predictions to increase our knowledge of aerosols and their impact on climate, the hydrological cycle, and air quality.

## 1.2 Aerosol and Water Vapor Properties from Collimated Solar Measurements

Direct sun and sky radiance measurements are conducted using the fully autonomous robotic Cimel Electronique CE-318 model Sun/sky radiometers (referred to as Cimels hereafter) deployed by the NASA AERONET project (see Figure 1.1). The measurement protocols, calibration techniques, and data processing have been described by Holben *et al.* [1998] and Eck *et al.* [1999, 2005], but important details are provided here. The AERONET Cimels have a full field of view of  $1.2^\circ$  and use two common filter configurations: standard 8-filter (340, 380, 440, 500, 675, 870, 940, 1020 nm) and

extended 9-filter (standard plus 1640 nm). For almucantar scans, the instrument points to the Sun, moves  $\pm 180^\circ$  azimuth from solar origin at a constant elevation angle to perform a total of 76 sky radiance measurements for each sky wavelength (e.g., 440, 675, 870, and 1020 nm) [Holben *et al.*, 1998]. Field instruments are inter-calibrated against AERONET reference Cimels, which are calibrated at Mauna Loa Observatory in Hawaii using Langley analyses [Shaw 1980, 1983; Eck *et al.*, 2005]. Columnar AOD, columnar water vapor (CWV) in centimeters, and almucantar retrievals utilized AERONET Version 2 algorithms and data quality criteria [Smirnov *et al.*, 2000; Dubovik *et al.*, 2000, 2006; Holben *et al.*, 2006]. The estimated accuracy of AERONET field Cimels varies spectrally from  $\pm 0.01$  to  $\pm 0.02$  for measured columnar AOD with higher errors in the ultraviolet channels [Holben *et al.*, 1998; Eck *et al.*, 1999], is within 10% for CWV retrievals [Schmid *et al.*, 2001; Smirnov *et al.*, 2004], and is typically less than 5% for calibrated sky radiances [Holben *et al.*, 1998].



**Figure 1.1 Cimel Sun/sky Radiometers deployed in Kanpur, India. Using a robot controlled by azimuth and zenith motors, the instrument points directly at the Sun given the time, location, and aid of a 4-quadrant detector. Light passes through a collimator tube, sensor head lens, and wavelength-dependent transmission filter on a filter wheel until it reaches a Silicon or InGaAs detector inside the sensor head canister. Photo courtesy of Sheng-Hsiang Wang.**

In addition, the manually-operated Solar Light Microtops II sun photometers (referred to as Microtops hereafter) performed direct sun measurements [Morys *et al.*, 2001]. The Microtops had varying sets of five filters utilizing the nominal wavelengths 440, 675, 870, and 940 with either 340 nm or 500 nm. Microtops data were collected using measurement and data processing protocols established by the Maritime Aerosol Network (MAN) component of AERONET [Smirnov *et al.*, 2009]. An artifact of the Microtops  $\sim 2^\circ$  full field of view is to allow more stray light than the AERONET Cimel; however, during dust events, any reduction in  $\tau_{500\text{nm}}$  is estimated to be less than 0.02

[Kinne *et al.*, 1997]. The estimated accuracy of Microtops instruments is  $\pm 0.02$  for measured columnar AOD at the nominal aerosol wavelengths [Smirnov *et al.*, 2009].

The direct sun voltage ( $V$ ) measured by the radiometer is proportional to the irradiance ( $I$ ). For Cimel reference instruments, the estimated top of the atmosphere irradiance ( $I_0$ ) in terms of voltage ( $V_0$  in mV) is obtained by Langley measurements at the Mauna Loa Observatory in Hawaii. Mauna Loa ( $19.54^\circ$ ,  $155.58^\circ$ , 3397 m) is located in the remote south central North Pacific above most boundary layer aerosols except for the occasional emissions of volcanic aerosols and episodic middle to upper tropospheric Asian dust that affects the measurements during the boreal spring [Holben *et al.*, 2001; Eck *et al.*, 2005]. The Langley plot is used to determine  $V_0$  by using a linear fit of  $\ln V$  versus the optical air mass ( $m$ , between 2 and 5 at visible and near infrared wavelengths) and extrapolated to  $m=0$  to obtain  $V_0$ . The total optical depth [ $\tau(\lambda)_{\text{Total}}$ ] can be obtained using the Beer-Lambert-Bouguer law (Transmission,  $T=I/I_0$ ) and given  $I$  is also proportional to  $V$  (the measured direct sun voltage in mV):

$$V(\lambda) = V_0(\lambda) * d^{-2} * \exp[-\tau(\lambda)_{\text{Total}} * m] \quad (1)$$

where  $d$  is the ratio of the average to the actual Earth-Sun distance and  $m$  is the optical air mass [Holben *et al.*, 1998]. Other atmospheric constituents can scatter and/or absorb light and must be considered when calculating the AOD. The optical depth due to water vapor, Rayleigh (molecular) scattering, and other wavelength-dependent trace gases must be subtracted from the total optical depth to obtain the AOD:

$$\tau(\lambda)_{\text{Aerosol}} = \tau(\lambda)_{\text{Total}} - \tau(\lambda)_{\text{Water}} - \tau(\lambda)_{\text{Rayleigh}} - \tau(\lambda)_{\text{O}_3} - \tau(\lambda)_{\text{NO}_2} - \tau(\lambda)_{\text{CO}_2} - \tau(\lambda)_{\text{CH}_4} \quad (2)$$

AERONET field instruments are inter-calibrated against reference Cimels. The calibration transfer may occur during low aerosol loading conditions ( $<0.2$  at AOD 500 nm) and near solar noon when the solar zenith angle changes most slowly allowing improved instrument time synchronization and reducing the relative AOD error due to air mass dependent instrument characteristics (e.g., filter transmittance). The relative error in AOD has a cosine solar zenith angle dependence ( $\delta V_o/V_o * 1/m$ ), where  $m \sim 1/\cos(\theta_o)$  for solar zenith angle ( $\theta_o$ ) less than  $75^\circ$ ; therefore, the greatest relative error in AOD occurs when the optical air mass is 1. The spectral AERONET AOD data are retrieved from measurements taken when the sun is not obscured by clouds and thus cloud optical depth is not a factor in the computation. If clouds contaminate the measurement, most of these points are removed from the Level 1.5 AOD data set automatically on the basis of temporal variability thresholds on the optical depth [Smirnov *et al.*, 2000]. The Level 2.0 AOD product applies pre- and post-deployment calibrations to the Level 1.5 AOD data and these data are further inspected for anomalies.

The dominant aerosol particle size can be determined using the Ångström exponent ( $\alpha$ ) [Ångström 1964], which is defined by the logarithms of AOD and wavelength [Eck *et al.*, 1999]:

$$\alpha = -d\ln[\tau(\lambda)]/d\ln[\lambda] \quad (3)$$

$\alpha$  is calculated for the inclusive wavelength range from 440 to 870 nm using a linear fit of  $\tau$  versus  $\lambda$  on a logarithmic scale; values closer to two indicate that small particles dominate and values approaching zero indicate larger aerosol particles dominate [Holben

*et al.*, 1991; *Kaufman et al.*, 1992; *Eck et al.*, 1999; *Reid et al.*, 1999].  $\alpha$  is related to the Junge or Power Law size distribution by the expression  $\alpha=3-v$ , where  $v$  is the parameter of the aerosol size distribution which is defined as  $dN/d\ln r=Cr^{-v}$  [*Junge* 1955]. Some deviation in the linear fit may occur for high fine mode AOD events where curvature (i.e.,  $\alpha'$  or the derivative of  $\alpha$ ) becomes more significant [*Eck et al.*, 1999]. While a combination of  $\alpha$  and  $\alpha'$  provides a more complete understanding of the aerosol size distribution,  $\alpha$  is more commonly used by ground-based and satellite-based remote sensing techniques to interpret aerosol particle size [*Eck et al.*, 1999; 2001]. Using the AOD measurements, the spectral deconvolution algorithm (SDA) retrieves the columnar optically equivalent fine mode ( $\tau_f$ ) and coarse mode ( $\tau_c$ ) AOD as well as the fine mode fraction of AOD [ $\eta=\tau_f/(\tau_f+\tau_c)$ ] at 500 nm. The SDA assumes a bimodal aerosol distribution, the coarse mode Ångström exponent ( $\alpha_c$ ) and its derivative ( $\alpha_c'$ ) are near zero, and a second order polynomial fit of spectral AOD in logarithmic coordinates [*O'Neill et al.*, 2001, 2003]. The SDA product quality depends on the input AOD wavelengths (i.e.,  $N \geq 4$  for Level 2.0), the spectral range (i.e., 380-870 nm for Level 2.0), the combination of aerosol loading and optical air mass dependence (i.e.,  $\tau \geq 0.02/m$ ), and the removal of outliers.

Columnar water vapor is determined by AERONET simultaneously with aerosol properties and uses three wavelengths: 675 nm, 870 nm, and 940 nm. The total transmission ( $T$ ) is computed for 675 nm and 870 nm using Rayleigh and aerosol optical depths and extrapolated to obtain the total transmission at the nominal 940 nm wavelength. The extrapolated transmission for 940 nm is subtracted from the measured transmission at 940 nm (i.e.,  $\ln(T_w) = \ln[T_{w940 \text{ nm(measured)}}] - \ln[T_{940 \text{ nm(extrapolated)}}]$ ) providing

the transmission only due to water vapor ( $T_w$ ), which can be expressed by the following equation:

$$-\ln(T_w) = \ln[V_{o\ 940\ \text{nm}} * d^{-2}] - \ln[V_{940\ \text{nm}}] - (m_a * \tau_a + m_R * \tau_R) \quad (4)$$

where  $V_{940\ \text{nm}}$  is the measured voltage (mV) at 940 nm,  $V_{o\ 940\ \text{nm}}$  is the extraterrestrial constant (mV),  $m_a$  and  $m_R$  are the optical air masses for aerosol and Rayleigh contributions, respectively, and  $\tau_a$  and  $\tau_R$  are the optical depths for aerosol and Rayleigh contributions, respectively, while effects by other trace gases are negligible for the 940 nm channel. Further, the columnar water vapor (CWV,  $u$ ) in cm can be determined using the following equation:

$$u = [-\ln(T_w)/a]^{1/b} / m_w \quad (5)$$

where  $a$  and  $b$  are filter-dependent constants, and  $m_w$  is the water vapor optical air mass [Schmid *et al.*, 1996, 2001]. The CWV calculations are typically accurate to less than 10% [Schmid *et al.*, 2001; Smirnov *et al.*, 2004]. In addition, Prasad and Singh [2009] showed high correlation ( $\sim 0.95$ ) between CWV retrieved from AERONET and GPS over Kanpur, India.

### 1.3 Aerosol Properties Using Almuantar Sky Radiance Measurements

In combination with the direct sun measurements, the Cimel performs sky radiance measurements at 76 azimuth angles at  $\pm 180^\circ$  from the solar zenith angle origin; this sky scan is known as an almuantar measurement [Holben *et al.*, 1998]. Aerosol optical and microphysical properties were computed from inversions of almuantar sky radiance measurements simultaneously with spectral AOD at the 440, 675, 870, and 1020

nm nominal wavelengths. Almucantar-retrieved aerosol properties include the aerosol volume size distribution, complex index of refraction, phase functions, and fraction (f) of particle sphericity [i.e.,  $f_{\text{sphericity}} = f_{\text{spherical}} / (f_{\text{spherical}} + f_{\text{spheroidal}})$ ]. The retrieved number size distribution is expressed as a volume size distribution using equation (6):

$$dV(r)/d \ln r = V(r) * dN(r)/d \ln r = 4/3 \pi r^3 * dN(r)/d \ln r \quad (6)$$

where  $r$  is the radius of the aerosol particle ( $\mu\text{m}$ ),  $V(r)$  is the volume of the aerosol particles with radius  $r$  ( $\mu\text{m}^3/\mu\text{m}^2$ ), and  $N(r)$  is the number of particles with radius  $r$  (in  $1/\mu\text{m}^2$ ). The volume size distribution may be integrated to calculate the volume concentration ( $C_v$  in  $\mu\text{m}^3/\mu\text{m}^2$ ), effective radius ( $r_{\text{eff}}$  in  $\mu\text{m}$ ), volume median radius ( $r_v$ ), the standard deviation (width) [Dubovik *et al.*, 2002]. The fine mode and coarse mode separation is  $\sim 1 \mu\text{m}$ ; however, the threshold may vary slightly depending on the inflection point between the fine mode and coarse mode maximums [Eck *et al.*, 2010]. In addition, aerosol fine mode and coarse mode AOD, asymmetry parameter, single scattering albedo, and absorption Ångström exponent are derived from the retrieved quantities [Dubovik and King, 2000; Dubovik *et al.*, 2002, 2006]. The single scattering albedo ( $\omega_0$ ) is defined as the ratio of scattering to the extinction ( $\tau_{\text{ext}} = \tau_{\text{scat}} + \tau_{\text{abs}}$ ) and indicates the probability that a photon will be scattered by an aerosol particle:

$$\omega_0 = \tau_{\text{scat}} / \tau_{\text{ext}} \quad (7)$$

where  $\tau_{\text{scat}}$  is the retrieved scattering aerosol optical depth,  $\tau_{\text{ext}}$  is the measured aerosol optical depth. A single scattering albedo of 1 indicates perfect particle scattering of

incident light, while values near zero indicate perfect particle absorption. By rearranging equation (7), absorption aerosol optical depth ( $\tau_{\text{abs}}$ ) can be expressed as:

$$\tau_{\text{abs}} = \tau_{\text{ext}} * (1 - \omega_0) \quad (8)$$

providing a formulation to obtain the absorption AOD from the retrieved single scattering albedo and measured extinction AOD.

The almucantar retrieval aerosol parameters depend on the measured AOD, angular distribution of sky radiances, and the magnitude of the sky radiances at each wavelength [Dubovik and King 2000]. The AERONET Version 2 almucantar retrieval assumes (1) a plane-parallel atmosphere, (2) particles are homogeneously distributed, (3) randomly oriented spheres or spheroids with a fixed aspect ratio exist in the sample volume, (4) surface reflectance for land is based on bidirectional reflectance distribution function (BRDF) models using on Moody ecosystem type input and water reflectance is based on Cox-Munk calculations using NCEP reanalysis wind speeds, and (5) the retrieved parameters represent optically effective columnar aerosol parameters [Dubovik et al., 2006; Eck et al., 2008]. The AERONET Version 2 almucantar inversion algorithms, data processing, quality controls, and input surface reflectance were discussed further by Holben et al. [2006] and Eck et al. [2008].

#### 1.4 TIGERZ Experiment in the Indo-Gangetic Plain

The TIGERZ experiment (2008-2011) was conducted by the NASA Aerosol Robotic Network (AERONET) project within the Indo-Gangetic Plain (IGP) in northern India located south of the Himalayan foothills, and the intensive operational period (IOP) occurred during the 2008 pre-monsoon (April-June). The TIGERZ IOP foci included (1)

the spatial and temporal characterization of columnar aerosol optical, microphysical, and absorption properties; (2) the identification of aerosol particle type mixtures; and (3) the validation of remotely sensed aerosol properties from satellites. Data collection and analysis involved scientists, engineers, and graduate students from 20 institutions in Europe, India, and North America. Of note, the TIGERZ experiment (i.e., “tigers”) was a larger follow-on effort to the smaller Cloud-Aerosol Lidar and Infrared Pathfinder Satellite Observation (CALIPSO) And Twilight Zone (CATZ) experiment (i.e., “cats”) held in the Baltimore/Washington D.C. region during the summer of 2007 [McPherson *et al.*, 2010].

Anthropogenic activities within the IGP produce pollution from urban, industrial, and rural combustion sources nearly continuously and convection-induced winds drive desert and alluvial dust into the atmosphere over the IGP during the pre-monsoon [Middleton, 1986; Littman, 1991; Chu *et al.*, 2003; Dey *et al.*, 2004; Singh *et al.*, 2004; Prasad *et al.*, 2007a; Remer *et al.*, 2008; Gautam *et al.*, 2009]. Atmospheric brown cloud formation over northern India influences the scattering and absorption of solar radiation and initiates radiative forcing effects such as solar dimming, surface cooling, and surface evaporation [Jacobson *et al.*, 2001; Ramanathan *et al.*, 2005; Ramanathan and Ramana, 2005; Pinker *et al.*, 2005; Dey and Tripathi, 2007; Gautam *et al.*, 2010]. Atmospheric turbidity measurements were initially conducted in the 1960s over India [Mani *et al.*, 1969], and aerosol field campaigns and monitoring networks have continued to be established in order to monitor aerosol loading and other properties. Recent field campaigns included the Indian Ocean Experiment (INDOEX) [Ramanathan *et al.*, 2001; Lelieveld *et al.*, 2001], Arabian Sea Monsoon Experiment (ARMEX-II) [Moorthy and

*Babu*, 2005], Indian Space Research Organization Geosphere Biosphere Programme (ISRO-GBP) [<http://www.isro.org/gbp/aerosol.apx>], and Integrated Campaign for Aerosols, gases, and Radiation Budget (ICARB) [*Beegum et al.*, 2008; *Moorthy et al.*, 2008; *Satheesh et al.*, 2009]. A ground-based network using the Multi-Wavelength Radiometers (MWR) has been deployed in India through ISRO-GBP activities [*Moorthy et al.*, 1989; *Gogoi et al.*, 2009]. Furthermore, Microtops have been operated by ISRO-GBP and others to measure aerosol optical properties in India [*Niranjan et al.*, 2005; *Singh et al.*, 2005; *Mishra et al.*, 2008; *Satheesh et al.*, 2009]. In addition to these programs, the AERONET Kanpur site has collected aerosol data since January 2001 [*Singh et al.*, 2003, 2004; *Tripathi et al.*, 2005a; *Dey et al.*, 2005; *Prasad and Singh*, 2007a, 2007b, 2009].

To improve the understanding of aerosols in the IGP, the NASA AERONET project and several international partners organized a multi-year, ground-based TIGERZ measurement campaign in May 2008. International partners included Canada (AEROCAN), Finland (Finnish Meteorological Institute) and France (PHOTONS) with collaborators in India including the India Meteorological Department (IMD), India Space Research Organization (ISRO), Indian Institute of Technology (Kanpur, Kharagpur, and Delhi), and Indian Institute of Tropical Meteorology (IITM). The first TIGERZ intensive operational period (IOP) occurred around the city of Kanpur from 1 May to 23 June 2008 (Figure 1.2b). Measurement activities during the IOP included the deployment of AERONET Cimel and Microtops instrumentation on selected days within the footprint of NASA Earth-observing satellites including Terra, Aqua, and Cloud-Aerosol Lidar and Infrared Pathfinder Satellite Observations (CALIPSO) as well as spatial variability

studies (SVSs) in and around the city of Kanpur. The CALIPSO satellite was given first priority for along-track instrument deployments due to a narrow 70 m footprint. Table 1.1 provides the instrument inventory deployed to the region and dates when data were collected during the intensive operational period (IOP). Furthermore, semi-permanent AERONET sites (i.e., Bareilly and Pantnagar) were deployed north of Kanpur to the Himalayan foothills (Nainital) to characterize aerosols across the IGP (Figure 1.2a).

**Table 1.1 Instrument inventory and availability during the 2008 TIGERZ IOP.**  
**Table from Giles *et al.* [2011a].**

Location	Coordinates	Instrument	Period
Kanpur (or IIT-Kanpur)	26° 30' 46"N, 80° 13' 53"E	Cimel	1 May – 23 June
Mobile_N_050608	26° 30' 22"N, 80° 26' 21"E	Cimel	6 May
Mobile_C_050608	26° 18' 10"N, 80° 29' 19"E	Cimel	6 May
Mobile_S_050608	26° 07' 30"N, 80° 31' 58"E	Cimel	6 May
Hand_N_050608	26° 19' 31"N, 80° 29' 01"E	Microtops	6 May
Hand_S_050608	26° 17' 08"N, 80° 29' 34"E	Microtops	6 May
Hand_E_050608	26° 18' 38"N, 80° 30' 49"E	Microtops	6 May
Hand_W_050608	26° 18' 09"N, 80° 27' 47"E	Microtops	6 May
Mobile_Kanpur_West(W2)	26° 25' 09"N, 80° 07' 24"E	Cimel	10, 26 and 30 May
Mobile_Kanpur_East	26° 27' 31"N, 80° 26' 22"E	Cimel	10, 26 and 30 May
Hand_Kanpur_North	26° 29' 55"N, 80° 18' 44"E	Microtops	10 and 26 May
Hand_Kanpur_South	26° 24' 39"N, 80° 19' 02"E	Microtops	10 and 26 May
Hand_Kanpur_Panki	26° 28' 44"N, 80° 15' 23"E	Microtops	10 and 26 May
Hand_Kanpur_RR	26° 27' 20"N, 80° 21' 02"E	Microtops	10 and 26 May
Mobile_Kanpur_South	26° 21' 10"N, 80° 18' 03"E	Cimel	30 May
Mobile_Kanpur_SE	26° 22' 43"N, 80° 25' 05"E	Cimel	30 May
Mobile_N_060708	26° 31' 50"N, 80° 30' 21"E	Cimel	7 June
Mobile_C_060708	26° 26' 58"N, 80° 31' 36"E	Cimel	7 June
Mobile_S_060708	26° 06' 21"N, 80° 36' 39"E	Cimel	7 June

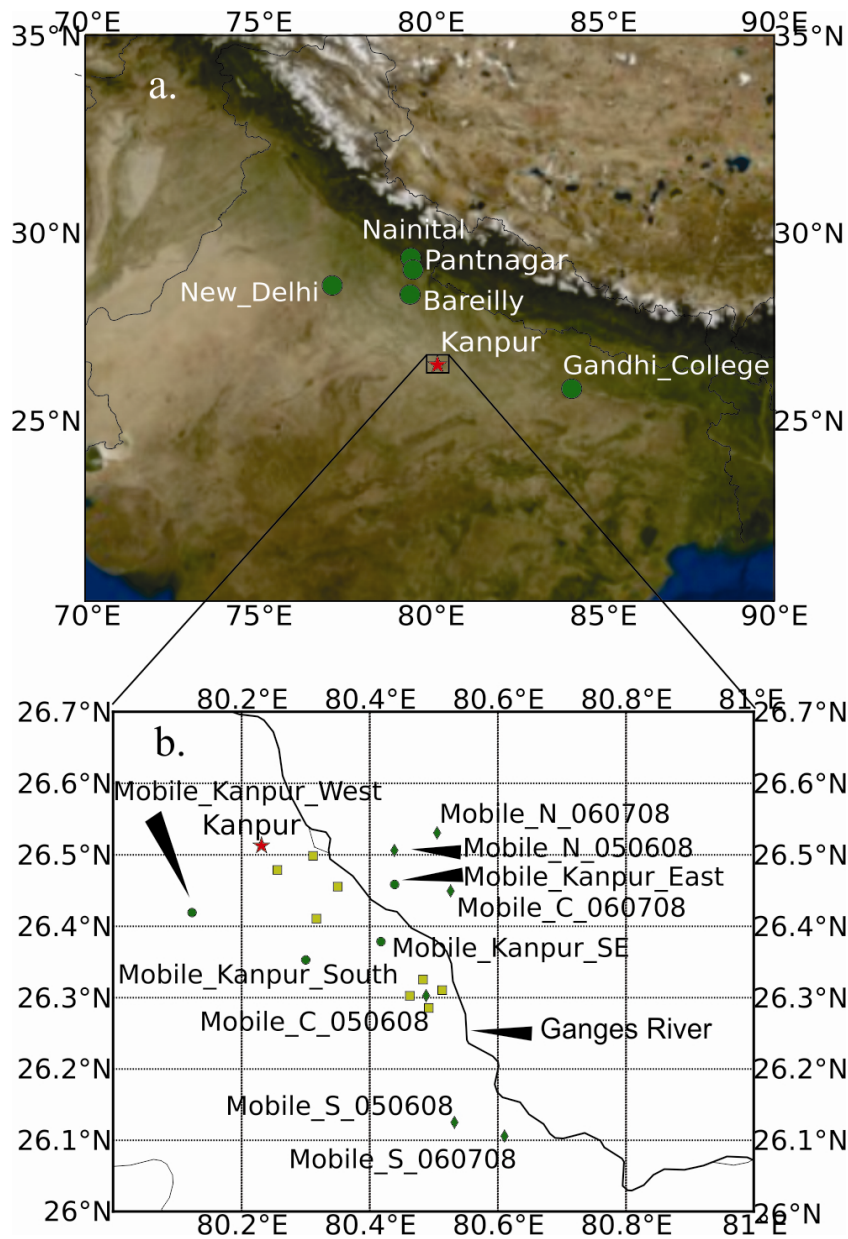


**Figure 1.2 Atmospheric flow originating over the Thar Desert, Arabian Sea, and Bay of Bengal is restricted by the Himalayan Mountains to the north of the Indo-Gangetic Plain (IGP) allowing aerosols to accumulate here. Map (a) shows the regional distribution of Cimel sites within the IGP and map (b) shows the distribution of sites around Kanpur, India (26.51°N, 80.23°E). The red star represents the IIT-Kanpur site and location of the permanent AERONET site. The green symbols represent Cimel sites, where circles indicate sites for Terra and Aqua satellite overpasses and diamonds represent sites for CALIPSO satellite overpasses. Yellow squares indicate Microtops sites. The Ganges River bisects the region. Figure from *Giles et al.* [2011a].**

## 1.5 Scientific Objectives and Outline of Dissertation

The major objectives of my dissertation include:

- Quantifying the spatial and temporal variability of columnar aerosol properties such as aerosol optical depth, volume size distribution, and single scattering albedo over Kanpur during the 2008 TIGERZ experiment.
- Analyzing aerosol retrievals from satellite over the IGP to determine how the mixture of dust and carbonaceous aerosols in combination with the semi-bright land surface affect the quality of the retrievals during the 2008 TIGERZ experiment.
- Evaluating relationships of aerosol size and absorption properties to determine black carbon and dust particle mixtures over Kanpur, India.
- Summarizing aerosol absorption properties (i.e., single scattering albedo and absorption Ångstrom exponent) at AERONET sites worldwide near aerosol source regions dominated by dust, urban/industrial pollution, biomass burning, and mixtures of them.
- Perturbing single scattering albedo to determine the response of the absorption Ångstrom exponent, which is a parameter that may determine the dominant absorbing aerosol type (e.g., dust, black carbon, or organic carbon).
- Evaluating and comparing aerosol absorption and size relationships at AERONET sites to determine the dominant aerosol mixing states and origins.

The Ph.D. dissertation was based on my two first-authored papers in the Journal of Geophysical Research – Atmospheres: (1) *Giles et al.* [2011a], a comprehensive study of aerosol properties and types using ground-based and space-based instrumentation over the Indo-Gangetic Plain during the 2008 TIGERZ experiment and (2) *Giles et al.* [2012], a comprehensive study of aerosol absorption properties at AERONET sites worldwide and classification of aerosol mixing states and origins. Chapter 2 (from *Giles et al.*, 2011a) presents climatology of aerosol properties over Kanpur, India, a comparison between Cimel sun photometer and Microtops instrumentation, and an assessment of the spatial and temporal variability of aerosol properties during TIGERZ. Chapter 3 (from *Giles et al.*, 2011a) evaluates the performance of MODIS operational and research satellite retrieval algorithms using data from several ground-based instruments distributed around Kanpur during TIGERZ. Chapter 4 (from *Giles et al.*, 2011a) presents an analysis of aerosol absorption and size relationships used to identify dominant aerosol types such as dust, black carbon, and mixtures of them using the Kanpur data set. Chapter 5 (from *Giles et al.*, 2012) uses data from 19 AERONET sites to compute aerosol absorption property statistics and compares these findings to previous work, quantifies the sensitivity of aerosol absorption Ångström exponent to changes in the single scattering albedo, and presents a cluster analysis for various aerosol absorption and size relationships to determine possible aerosol mixing states and origins. Finally, Chapter 6 (from *Giles et al.*, 2011a; 2012) provides the major findings of this work and addresses the potential impact of studies such as TIGERZ, additional work using TIGERZ aerosol data, and possible directions to provide more detailed aerosol classifications.

## Chapter 2: Aerosol Properties in Kanpur during TIGERZ

*Reproduced by permission of American Geophysical Union.*

### 2.1 Motivation and Methodology

Aerosol conditions over the IGP during the pre-monsoon are affected by locally generated and regionally transported aerosol particles such as fine mode pollution containing secondary organic carbon (OC) and black carbon (BC) from urban and industrial sources as well as dust mainly from nearby arid agricultural lands and the Thar Desert [Middleton, 1986; Littman, 1991; Chu *et al.*, 2003; Dey *et al.*, 2004; Singh *et al.*, 2004; Prasad *et al.*, 2007; Remer *et al.*, 2008; Gautam *et al.*, 2009, Arola *et al.*, 2011]. These aerosol particles challenge remote sensing algorithms for ground-based sensors due to the combined temporal and spatial variability of dust resembling thin cirrus clouds, and algorithms for space-based sensors due to assumed aerosol absorption models and semi-bright land surface during the pre-monsoon. General circulation models have simulated shifts in the monsoon circulation due in part to high aerosol loading and radiative effects of BC and dust particles over the IGP. The Elevated Heat Pump (EHP) hypothesis proposed by Lau and Kim [2006] and Lau *et al.* [2006] was explored by the 2007-2011 Joint Aerosol-Monsoon Experiment (JAMEX) activities to further understand aerosol-monsoon interactions [Lau *et al.*, 2008]. Within this context, the AERONET project initiated the TIGERZ experiment to measure aerosol properties at sites spanning the IGP in 2008. Although the TIGERZ experiment had several components, one element was to establish up to seven temporary sites near Kanpur, India (26.51°N, 80.23°E) located ~300 km south of the Himalayan foothills. In addition to the long-term monitoring AERONET site at the Indian Institute of Technology (IIT) Kanpur, these

TIGERZ sites provided the framework to quantify the spatial and temporal variability of columnar aerosol optical depth (AOD,  $\tau$ ), volume size distribution, and single scattering albedo (SSA). Long-term AERONET Kanpur data and TIGERZ results were examined to identify BC and dust particle mixtures from aerosol size, shape, and absorption properties. Lastly, the TIGERZ mesoscale deployment data set was utilized for validation of aerosol retrievals from satellite [e.g., Moderate Resolution Imaging Spectroradiometer (MODIS)].

To further understand aerosol remote sensing measurements performed within the IGP, the NASA AERONET project and several international partners organized the TIGERZ multi-year, ground-based measurement campaign. TIGERZ sites were deployed spatially within the mesoscale domain based on definitions by Orlanski [1975]. A mesoscale- $\alpha$  (200-2000 km) distribution of semi-permanent AERONET sites (e.g., Bareilly and Pantnagar) was established north of Kanpur to the Himalayan foothills (Nainital) to characterize aerosols latitudinally across the IGP for the multi-year effort (Figure 1.2a) [Dumka *et al.*, 2012, in preparation]. The TIGERZ IOP occurred in the greater Kanpur region from 1 May to 23 June 2008. Figure 1.2b shows the site distribution and Table 1.1 provides site deployment details. Temporary sites were established within mesoscale- $\gamma$  (2-20 km) and - $\beta$  (20-200 km) domains using AERONET Cimels and Microtops to assess the influence of Kanpur pollution to the IGP aerosol loading as well as provide validation points for Terra, Aqua, and CALIPSO satellite retrievals [Vaughan *et al.*, 2004; Anderson *et al.*, 2005]. Due to the deviation from standard AERONET protocol during TIGERZ (i.e., ~30-second rather than ~15-minute data collection intervals), temporary site Level 1.5 AOD data are manually cloud

screened and quality assured using the detailed field logs. The low optical air mass ( $m < 1.3$ ) during satellite overpass times precluded useful almucantar sky radiance measurements due to a limited range of measured scattering angles [Dubovik *et al.*, 2000]. A temporary deployment of sites with 15-30 km site separation, conducted from 09:45-12:45 UTC ( $1.3 \leq m \leq 6.3$ ) on 30 May 2008, provided the first-of-its-kind spatial variability assessment of sky radiance derived AERONET aerosol properties in India.

## 2.2 Aerosol Variability and Transport over Kanpur, India

The AERONET long-term monitoring site at IIT-Kanpur is positioned  $\sim 17$  km northwest of Kanpur's main industrial region (Figure 1.2). Previous work has shown that distinct seasonal patterns of aerosol properties are controlled by the monsoon ( $\sim$ June-September) and post-monsoon (October-December) over Kanpur [Singh *et al.*, 2004; Jethva *et al.*, 2005; Dey *et al.*, 2005; Eck *et al.*, 2010]. Figure 2.1 shows the AERONET Kanpur climatology (2001-2009) of AOD ( $\tau_{500\text{nm}}$ ,  $\tau_{f500\text{nm}}$ ,  $\tau_{c500\text{nm}}$ ),  $\eta_{500\text{nm}}$ , and CWV with total AOD and CWV variability resembling seasonal fluctuations shown by Singh *et al.* [2004], Jethva *et al.* [2005], and Eck *et al.* [2010]. During the pre-monsoon (April-June),  $\tau_{c500\text{nm}}$  increased by 0.21, while  $\tau_{f500\text{nm}}$  increased by 0.03 and  $\eta_{500\text{nm}}$  decreased by 0.03 indicating dust contributed strongly to the  $\tau_{500\text{nm}}$  increase of 0.24. A climatologically-averaged CWV increase of  $\sim 3$  cm between April and July over Kanpur corresponded to CWV increases observed by MWR, MODIS, and Global Positioning System (GPS) retrievals in northern India indicating the transition to the monsoon [Moorthy *et al.*, 2007; Kumar *et al.*, 2011]. Figure 2.2 depicts 3-day back trajectory analyses starting from Kanpur at 1000 m, derived from the NOAA Air Resources Laboratory (ARL) Hybrid

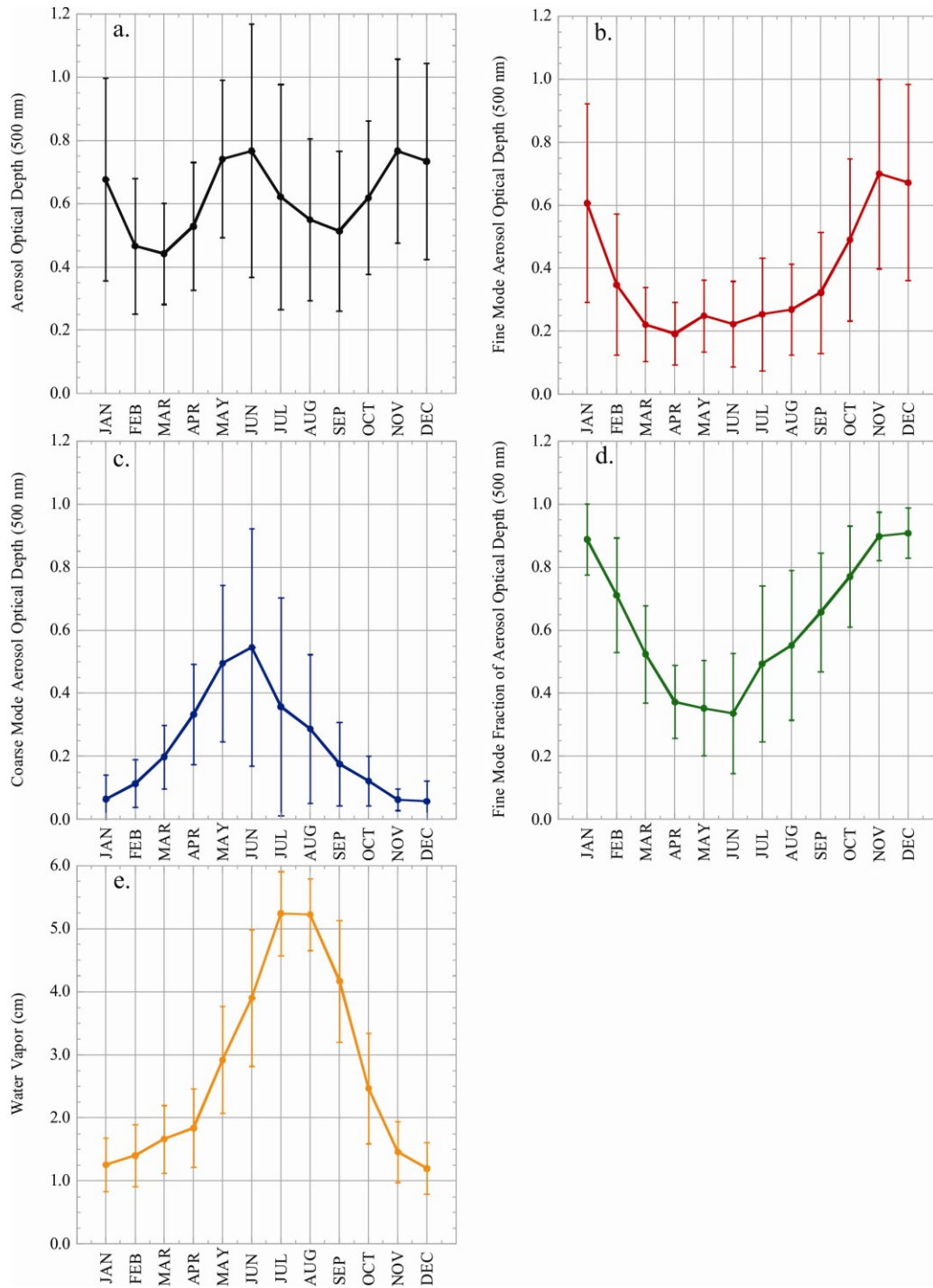


**Figure 2.1** The 2001-2009 Kanpur multi-year monthly averages are plotted for aerosol optical depth and water vapor (a,e) and spectral deconvolution algorithm (SDA) retrievals (b-d) at the Level 2.0 quality level. Maximums in total and coarse mode aerosol optical depth in May and June indicate the presence of transported desert dust and the maximum in water vapor (cm) during July and August indicates the peak of the monsoon. Figure from *Giles et al.* [2011a].

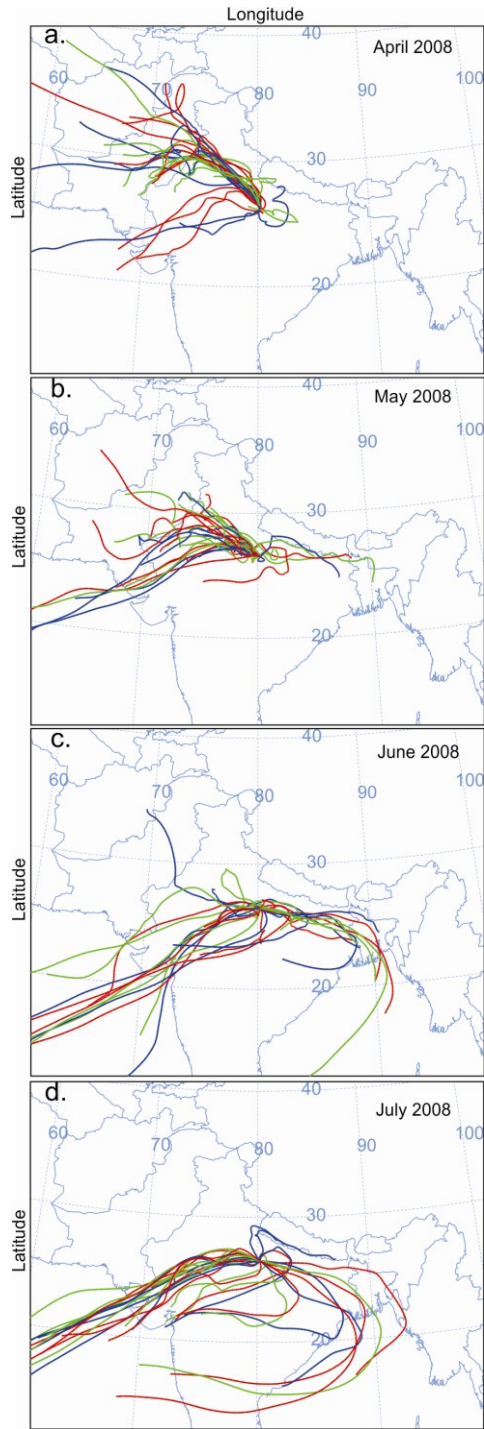


**Figure 2.2** The NOAA HYSPLIT 3-day back trajectory analyses are shown for Kanpur, India ( $26.51^{\circ}\text{N}$ ,  $80.23^{\circ}\text{E}$ ). The trajectories start at 06 UTC and at a height of 1000 m daily from April-July 2008 (a-d). Colored trajectory lines show differentiation among trajectory days. The trajectories are based on the Global Data Assimilation System (GDAS) data available from NOAA Air Resources Laboratory (ARL, <http://ready.arl.noaa.gov/HYSPLIT.php>). Figure from *Giles et al.* [2011a].

Single Particle Lagrangian Integrated Trajectory (HYSPPLIT) model [Draxler and Rolph, 2010; Rolph 2010]. The April 2008 trajectories show potential aerosol transport pathways originating to the west and northwest of Kanpur in Pakistan and northern India, and May 2008 trajectories show a transition to air parcels originating in the Arabian Sea and travelling across the Thar Desert; these trajectories resemble dust transport pathways to Kanpur as shown by Chinnam *et al.* [2006] and Prasad and Singh [2007a]. The June 2008 and July 2008 trajectories show that most air parcels originate over the Arabian Sea and Bay of Bengal transporting moisture inland as the monsoon develops.

The pre-monsoon (April-June) climatologically-averaged  $\tau_{c500nm}$  and  $\tau_{f500nm}$  of  $0.46 \pm 0.11$  and  $0.22 \pm 0.03$ , respectively, represents the dominance of long-range desert dust transport and regionally generated alluvial dust over pollution particles. Emission sources near Kanpur include vehicles powered by a variety of fuels, coal-fired power generation, leather factories, brick kilns (Figure 2.3) [Reddy *et al.*, 2002; Singh *et al.*, 2004; Jethva *et al.*, 2005; Dey *et al.*, 2005; Chinnam *et al.*, 2006; Prasad *et al.*, 2006; Gautam *et al.*, 2009; Eck *et al.*, 2010; Singh 2010], and wood fuel and agricultural waste from biomass fuel burning [Dickerson *et al.*, 2002; Gustafsson *et al.*, 2009; Ram *et al.*, 2010a, 2010b]. The interaction of fine and coarse mode particles during the pre-monsoon over Kanpur provided a unique opportunity to study remotely sensed properties of complex aerosol mixtures from the surface and space.



**Figure 2.3 Fossil fuel aerosol sources, such as the coal-fired Panki power plant (top panel) and a coal-fired mix of agricultural waste and/or wood in a Bull's Trench kiln (bottom panel), emit black carbon particles and precursor gases (e.g. nitrogen oxides and sulfur dioxide) to form nitrates and sulfates contributing to aerosol loading in the atmosphere over Kanpur, India.**

### 2.3 Comparison of Microtops and AERONET

The AERONET reference Cimels obtain calibration at the Mauna Loa Observatory in Hawaii [Shaw 1980, 1983; Eck *et al.*, 2005] and routinely cycle through the NASA Goddard Space Flight Center (GSFC) calibration facility to provide calibration transfer to Cimel and Microtops field instruments during clear and stable atmospheric conditions [Holben *et al.*, 1998; Smirnov *et al.*, 2009]. The accuracy of AERONET reference Cimels for measured columnar AOD is  $\sim 0.004$  in the visible and near-infrared wavelengths and  $\sim 0.01$  in the ultraviolet wavelengths [Eck *et al.*, 1999]. Although none of the AERONET reference Cimels was deployed during TIGERZ, a consistency check among the field Cimels and Microtops was performed by comparing the AOD measured at IIT-Kanpur for a 30-minute period from 05:19 UTC to 05:49 UTC on 25 May 2008 (Figure 2.4). The AERONET Cimel #83 (or C83) was chosen arbitrarily as a “reference” to compare with other Cimels and Microtops. The C83 instrument average  $\tau_{500\text{nm}}$  for the period was  $0.390 \pm 0.029$  and the other Cimel and Microtops averages were within  $\pm 0.01$  and  $\pm 0.02$ , respectively. The  $\tau_{f500\text{nm}}$  and  $\tau_{c500\text{nm}}$  averages of  $0.235 \pm 0.02$  and  $0.150 \pm 0.01$ , respectively, from C83 indicate the presence of fine mode pollution (e.g., primarily OC, sulfates, nitrates, and BC) and dust particles. Given that Microtops and Cimels averaged AOD were similar, the apparent effect of dust particles to scatter more light into the Microtops larger field of view was not evident in this case. Overall, the Cimel and Microtops comparison showed that AOD differences were consistent with the stated field instrument uncertainties.

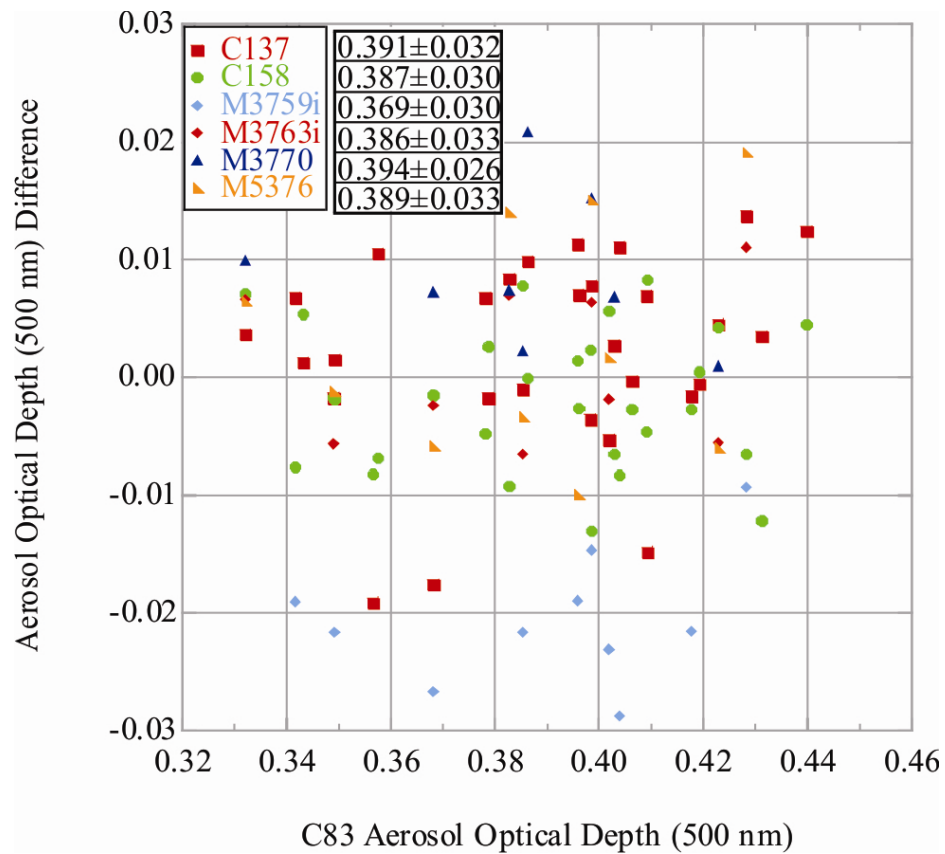


**Figure 2.4 Cimel and Microtops aerosol optical depth at 500 nm ( $\tau_{500\text{nm}}$ ) measurements were compared to an arbitrary Cimel #83 (C83) at IIT-Kanpur between 05:19 UTC and 05:49 UTC on 25 May 2008, and ranged within the stated uncertainty. The “C” indicates a Cimel instrument number and “M” indicates a Microtops number. The “i” at the end of the Microtops number indicates that data were interpolated to 500 nm. The values adjacent to the legend represent the  $\tau_{500\text{nm}}$  average values for each instrument during the comparison period. Figure from *Giles et al. [2011a]*.**

#### 2.4 Spatial and Temporal Variability of AOD

The TIGERZ IOP aerosol temporal variability was evaluated at IIT-Kanpur and spatial variability was determined over an area covering  $\sim 50 \text{ km}^2$  around Kanpur (Figure 1.2). Spatial variability can be analyzed by comparing one site to many nearby sites using time coincident measurements and observing the change in correlation or coefficient of variability as a function of site separation distance [*Hay and Suckling, 1979, Holben et al., 1991*]. Although the TIGERZ IOP data set did not meet temporal

requirements for computation of the coefficient of variability, the correlations of coincident observations at 5- and 15-minute discrete intervals were analyzed for 6 and 30 May 2008; however, matchups were still statistically insignificant. Instead, TIGERZ IOP data are presented temporally as site averages and deviations and spatially as area-averages and area standard deviations derived from all sites during coincident periods.

The IIT-Kanpur AERONET Cimel Level 2.0 daily averaged AOD temporal variability is shown in Figure 2.5. From 1 May to 12 June 2008, averaged  $\tau_{500\text{nm}}$ ,  $\tau_{f500\text{nm}}$ ,  $\tau_{c500\text{nm}}$ , and  $\eta_{500\text{nm}}$  were  $0.65\pm 0.18$ ,  $0.24\pm 0.13$ ,  $0.42\pm 0.15$ , and  $0.36\pm 0.14$ , respectively, indicating high aerosol loading and mainly coarse mode particle contributions to the AOD. On temporary deployment days, IIT-Kanpur daily averages for  $\tau_{500\text{nm}}$  and  $\eta_{500\text{nm}}$  varied from 0.28-0.78 and 0.21-0.37, respectively, due to transported dust. The coefficient of variation (CV) is calculated by dividing the standard deviation by the mean and multiplying by 100 to calculate the relative variability with respect to the mean. For the period, total and coarse mode aerosol loading CV was ~25-55% of the mean, which may represent dust transport and the removal of aerosols due to dry deposition and rainfall.

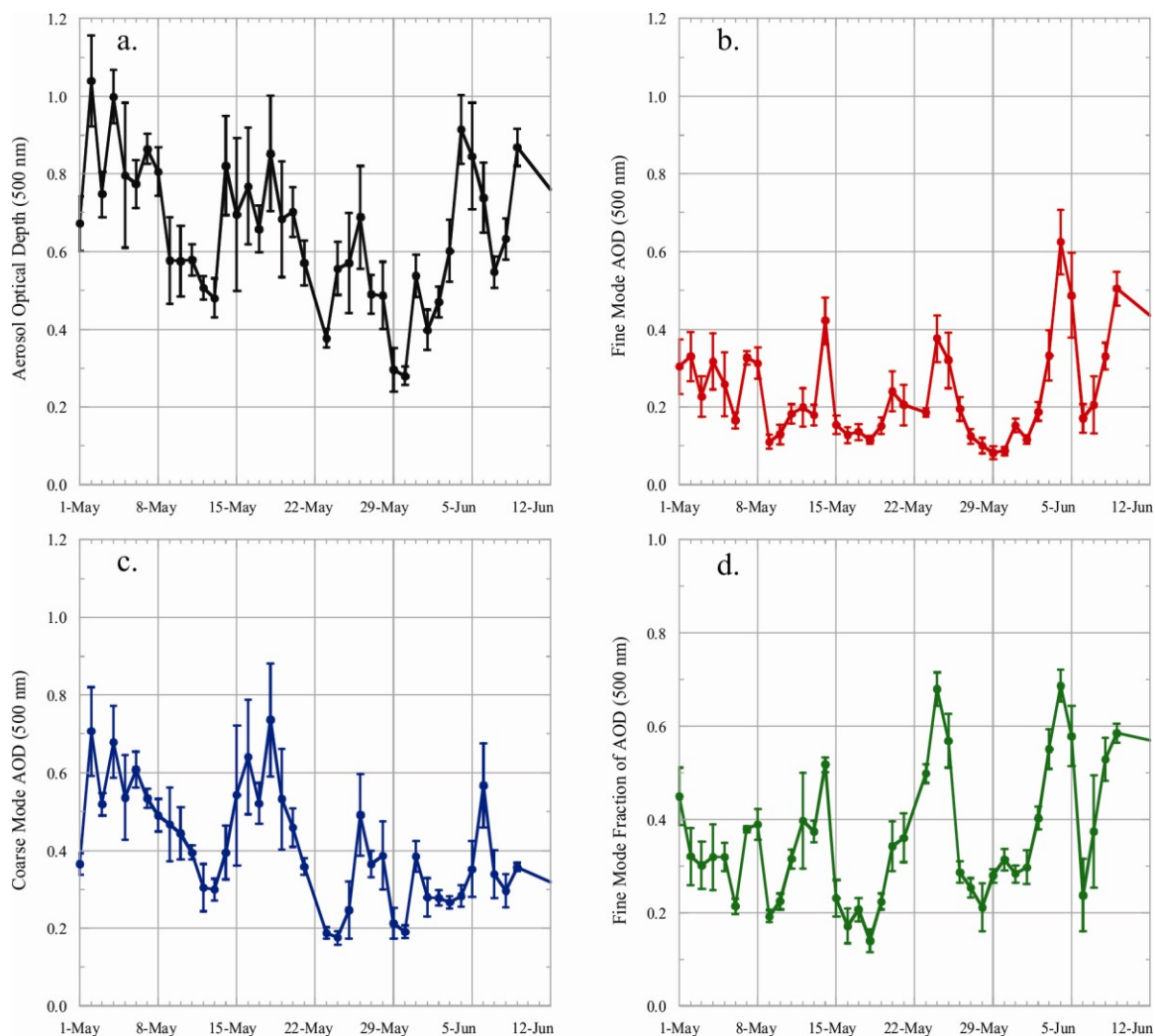


**Figure 2.5** Substantial day-to-day variation of aerosol loading occurred during the TIGERZ IOP possibly due to dust transport, dry deposition, and precipitation. Aerosol optical depth (AOD) daily averages of AERONET Level 2.0 are plotted for IIT-Kanpur, India, from 1 May to 12 June 2008. Temporary sites were deployed on 6 May, 10 May, 26 May, 30 May, and 7 June 2008. Figure from *Giles et al.* [2011a].

Spatial aerosol variability was assessed using area averages for deployment days (Table 2.1). Most area averages for  $\tau_{500\text{nm}}$ ,  $\tau_{f500\text{nm}}$ , and  $\tau_{c500\text{nm}}$  lie within one standard deviation of the multi-year monthly averages (Figure 2.1); however, on 30 May 2008, area-averaged AOD ( $\tau_{500\text{nm}} = 0.30$ ;  $\tau_{f500\text{nm}} = 0.09$ ;  $\tau_{c500\text{nm}} = 0.21$ ) were anomalously low for May and June. For temporary deployments on 10 and 26 May 2008, when Microtops were located within the industrial sector and Cimels in the outer sections of Kanpur,

Microtops  $\tau_{500\text{nm}}$  area averages were 0.03 and 0.09 higher than Cimel area averages, respectively. Coincident period  $\tau_{500\text{nm}}$  area-averaged standard deviations were up to  $\pm 0.04$ , indicating significant spatial variability in the measurements over different deployment configurations, whereas Microtops deviations on 6 May were only  $\pm 0.01$  likely due to their proximity to each other. The Ångström exponent ( $\alpha = 0.20$  to  $0.39$ ) and fine mode fraction of AOD ( $\eta_{500\text{nm}} = 0.21$  to  $0.33$ ) area-averages represent the presence of mainly super-micron radius or coarse mode particles region-wide on deployment days, except on 7 June 2008, when  $\alpha \sim 0.95$  and  $\eta_{500\text{nm}}$  of  $0.55$  were observed indicating a reduction of coarse mode particle AOD. Near-surface winds from the Navy Operational Global Atmospheric Prediction System (NOGAPS) model were analyzed to identify the change in aerosol loading between upwind and downwind sites. Although aerosol sources in Kanpur emit both particles (e.g., OC and BC) and precursor gases (i.e.,  $\text{SO}_2$ ,  $\text{NO}_x$ , etc.) into the atmosphere over the IGP [Tripathi *et al.*, 2005b; Arola *et al.*, 2011], sites downwind of the Kanpur urban center reported an increase in  $\tau_{500\text{nm}}$  only up to  $\sim 0.10$  near these sources. On the 30 May deployment day with only Cimels, the IIT-Kanpur and Mobile\_West sites upwind of Kanpur industrial sector had lower average AOD ( $\tau_{500\text{nm}} = 0.28 \pm 0.02$ ,  $0.29 \pm 0.01$ , respectively) than the Mobile\_Southeast site ( $\tau_{500\text{nm}} = 0.33 \pm 0.02$ ) by as much as  $0.05$ . These upwind/downwind AOD increases were consistent with differences between Microtops within and Cimels outside the city of Kanpur on the 10 and 26 May 2008. Approximately 10-20% of the aerosol loading detected by ground-based sun photometers on temporary deployment days resulted from the Kanpur city emission contributions to the upwind aerosols comprised of a mixture of pollution and dust.

**Table 2.1 Mesoscale deployment day area averages of aerosol properties for coincident measurement periods<sup>a</sup>. Table from *Giles et al.* [2011a].**

Group	$\tau$	$\alpha$	$\tau_f$	$\tau_c$	$\eta$	Time (UTC)
6 May 2008						
All	0.75±0.03	0.22±0.03	0.17±0.02	0.58±0.03	0.23±0.03	07:30-08:37
Cimel	0.77±0.02	0.20±0.03	0.16±0.02	0.61±0.01	0.21±0.02	03:00-11:17
Microtops	0.73±0.01	0.22±0.01	0.17±0.02	0.55±0.03	0.24±0.03	07:30-08:37
10 May 2008						
All	0.69±0.03	0.30±0.06	0.19±0.03	0.51±0.04	0.27±0.04	05:00-06:06
Cimel	0.68±0.04	0.26±0.06	0.16±0.02	0.51±0.04	0.24±0.03	04:51-06:06
Microtops	0.71±0.04	0.32±0.05	0.21±0.03	0.51±0.04	0.29±0.03	05:00-08:36
26 May 2008						
All	0.88±0.04	0.38±0.05	0.27±0.04	0.61±0.03	0.31±0.03	05:00-07:30
Cimel	0.84±0.03	0.36±0.06	0.25±0.03	0.59±0.02	0.30±0.03	05:00-07:30
Microtops	0.93±0.04	0.39±0.05	0.32±0.05	0.64±0.03	0.33±0.03	04:30-08:47
30 May 2008						
Cimel	0.30±0.02	0.38±0.01	0.09±0.01	0.21±0.01	0.30±0.01	10:05-12:30
7 June 2008						
Cimel	0.60±0.04	0.94±0.03	0.33±0.03	0.26±0.02	0.55±0.02	03:38-05:48

<sup>a</sup>Aerosol properties at 500 nm, except  $\alpha$  was calculated between 440 and 870 nm.

## 2.5 Spatial and Temporal Variability of Absorption and Size Properties

Temporary site deployments within mesoscale- $\gamma$  and - $\beta$  (15-30 km site separation) domains provided a unique opportunity to acquire up to eight almucantar inversions on 30 May 2008. All of the products were processed utilizing the AERONET Level 2.0 inversion criteria [*Holben et al.*, 2006], except the input AOD may have been Level 1.5 as discussed in Section 2.1. To help interpret absorption results when  $\tau_{440\text{nm}}$  is  $\leq 0.40$ , a development version of the inversion code provided uncertainty estimates for each SSA retrieval. Area-averaged aerosol properties for the size distribution, single scattering albedo, and parameterizations describing the size distribution were calculated for the region covered by the temporary deployment on 30 May (09:40-12:27 UTC). The volume size distribution shows coarse mode dominated aerosol loading for all sites (Figure 2.6a). Calculated from volume concentration ( $C_v$ ), effective radius ( $r_{\text{eff}}$ ), volume

mean radius ( $r_v$ ), and standard deviation ( $\sigma$ ) derived size distribution quantities in Table 2.2, the coefficient of variation was less than 10% of the area-averages indicating mainly uniformly sized particles over the region. Spectral SSA area-averages in Figure 2.6b were  $0.87 \pm 0.01$ ,  $0.91 \pm 0.01$ ,  $0.92 \pm 0.01$ , and  $0.93 \pm 0.01$  for 440, 675, 870, and 1020 nm nominal wavelengths indicating spatially homogeneous absorption by aerosol particles. While average  $\tau_{440\text{nm}}$  was  $\sim 0.33$ , the average uncertainties for SSA (Figure 2.6b) were approximately  $\pm 0.04$  over the 440 nm to 1020 nm range, consistent with increased uncertainty during low aerosol loading ( $\tau_{440\text{nm}} \leq 0.4$ ). The SSA uncertainty has not been quantified for the AERONET Version 2 almucantar retrievals; however, it has been estimated as  $\pm 0.03$  for  $\tau_{440\text{nm}} > 0.4$  for Version 1 retrievals [Dubovik *et al.*, 2002]. Although temporal SSA averages vary within the calculated uncertainty of  $\pm 0.04$ , Figure 2.6b suggests a higher probability of more absorbing aerosols downwind of Kanpur at the Mobile\_SE site (where higher AOD was also found) with higher SSA values at sites north and east of the city. Black carbon particles emitted from the Panki power plant and other sources possibly increased aerosol absorption downwind of Kanpur [Tripathi *et al.*, 2005b]. Stronger spectral absorption at 440 nm represented the absorption by iron oxides in dust, whereas increasing absorption at longer wavelengths possibly represented a greater contribution of BC to the optical mixture.

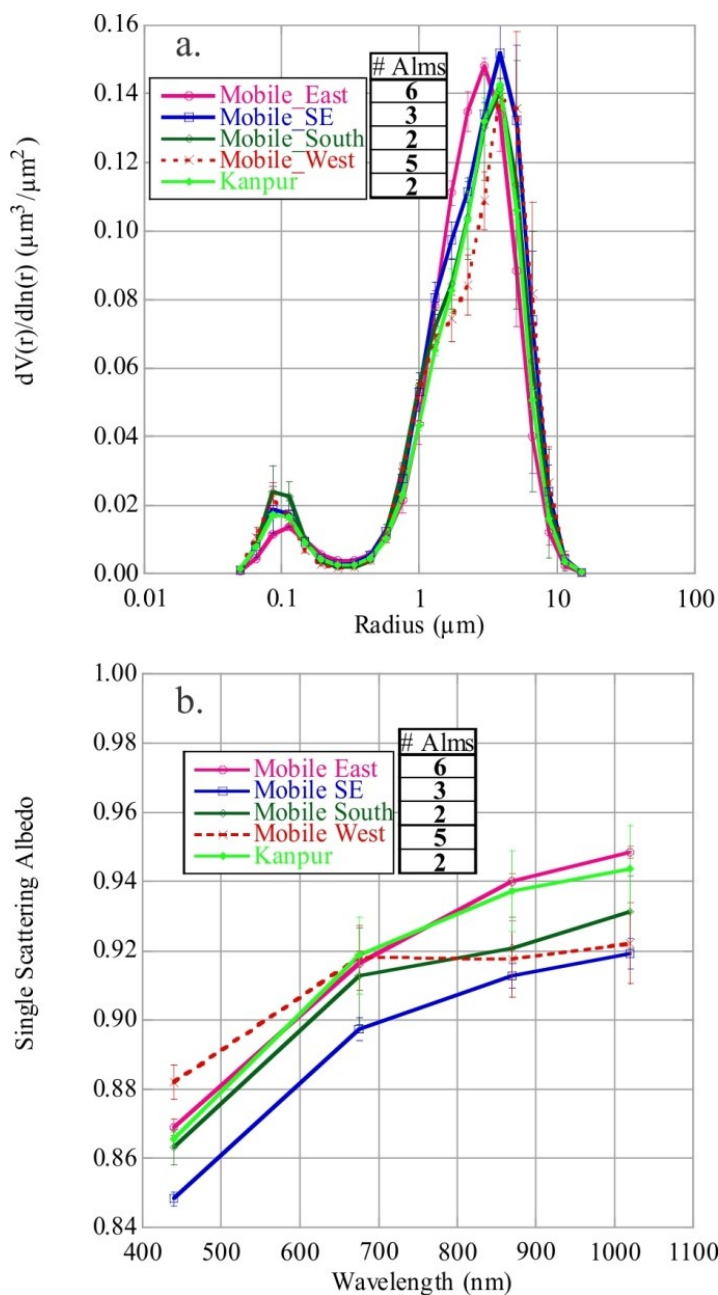


**Figure 2.6 Data from TIGERZ IOP sites indicated spatially homogeneous, uniformly sized, spectrally absorbing pollution and dust particles. Temporally averaged almucantar retrieval plots for aerosol volume size distribution (a) and spectral single scattering albedo (SSA) (b) for the Mobile\_East site (pink), Mobile\_Southeast (blue), Mobile\_South (green), Mobile\_West (red), and Kanpur (light green) sites are shown for the temporary site deployment on 30 May 2008. The vertical bars indicate the standard deviation in each plot. The average  $\tau_{440\text{nm}}$  was 0.33 with solar zenith angle greater than 50 degrees. Figure from Giles *et al.* [2011a].**

**Table 2.2 Area-averaged aerosol volume size distribution quantities for fine mode (*f*) and coarse mode (*c*) aerosols on 30 May 2008<sup>a</sup>. Table from *Giles et al.* [2011a].**

Site	$r_{\text{eff}} (\mu\text{m})$		$C_v (\mu\text{m}^3/\mu\text{m}^2)$		$r_v$		$\sigma$		N
	<i>f</i>	<i>c</i>	<i>f</i>	<i>c</i>	<i>f</i>	<i>c</i>	<i>f</i>	<i>c</i>	
Mobile_Kanpur_East	0.12	2.11	0.016	0.227	0.14	2.52	0.52	0.59	6
Mobile_Kanpur_SE	0.11	2.20	0.019	0.246	0.12	2.73	0.50	0.64	3
Mobile_Kanpur_South	0.10	2.17	0.021	0.235	0.11	2.67	0.43	0.64	2
Mobile_Kanpur_West	0.09	2.23	0.018	0.223	0.11	2.84	0.46	0.67	5
Kanpur	0.11	2.21	0.018	0.212	0.12	2.71	0.50	0.62	2
Area Average	0.11	2.18	0.018	0.229	0.12	2.69	0.48	0.63	
	$\pm 0.01$	$\pm 0.05$	$\pm 0.001$	$\pm 0.013$	$\pm 0.01$	$\pm 0.12$	$\pm 0.04$	$\pm 0.03$	

<sup>a</sup> Corresponds to Figure 2.6a.

## Chapter 3: Evaluation of MODIS over Kanpur during TIGERZ

*Reproduced by permission of American Geophysical Union.*

### 3.1 Motivation

Passive satellite remote sensing techniques utilize the reflectance of solar radiation that has passed through the atmosphere from the Sun and returned to space. The spectral magnitude of the radiances varies depending on the aerosol properties in addition to properties of the Earth's surface. Other factors such as instrument field of view, viewing angles, and orbit also play a role in the radiances. Lookup tables are necessary in satellite remote sensing retrievals to establish a priori set of expected conditions to produce a result consistent with ground-based measurements. Over bright (deserts) and semi-bright surfaces, aerosols can be difficult to detect due to the strong contribution by the Earth's surface. While algorithms have been developed for the bright surfaces where the blue spectrum can be utilized due to lower signal, the semi-bright surface still remains an issue especially in regions with high aerosol loading dominated by dust. The Normalized Difference Vegetation Index (NDVI) is calculated using the radiance of near infrared (0.75-1.5  $\mu\text{m}$ ) and visible (0.6-0.7  $\mu\text{m}$ ) bands [(NIR-VIS)/(NIR+VIS)] from satellites, such as Advanced Very High Resolution Radiometer (AVHRR) and MODIS, to determine areas of green vegetation with positive values near 0 indicating sparse green vegetation and values near 1 indicating dense green leaf vegetation [Kriegler *et al.*, 1969; Tucker 1979]. For example, during the spring months (March-April-May), the Indo-Gangetic Plain (IGP) has sparsely vegetated agricultural land (Figure 3.1), while more dense green vegetation usually exists in the IGP between the monsoon and winter seasons. Satellite retrieval algorithms may not have enough

sensitivity or confidence level to detect aerosol properties in the presence of dust when present over semi-bright surfaces, skewing the statistics that otherwise show good algorithm performance over the region.

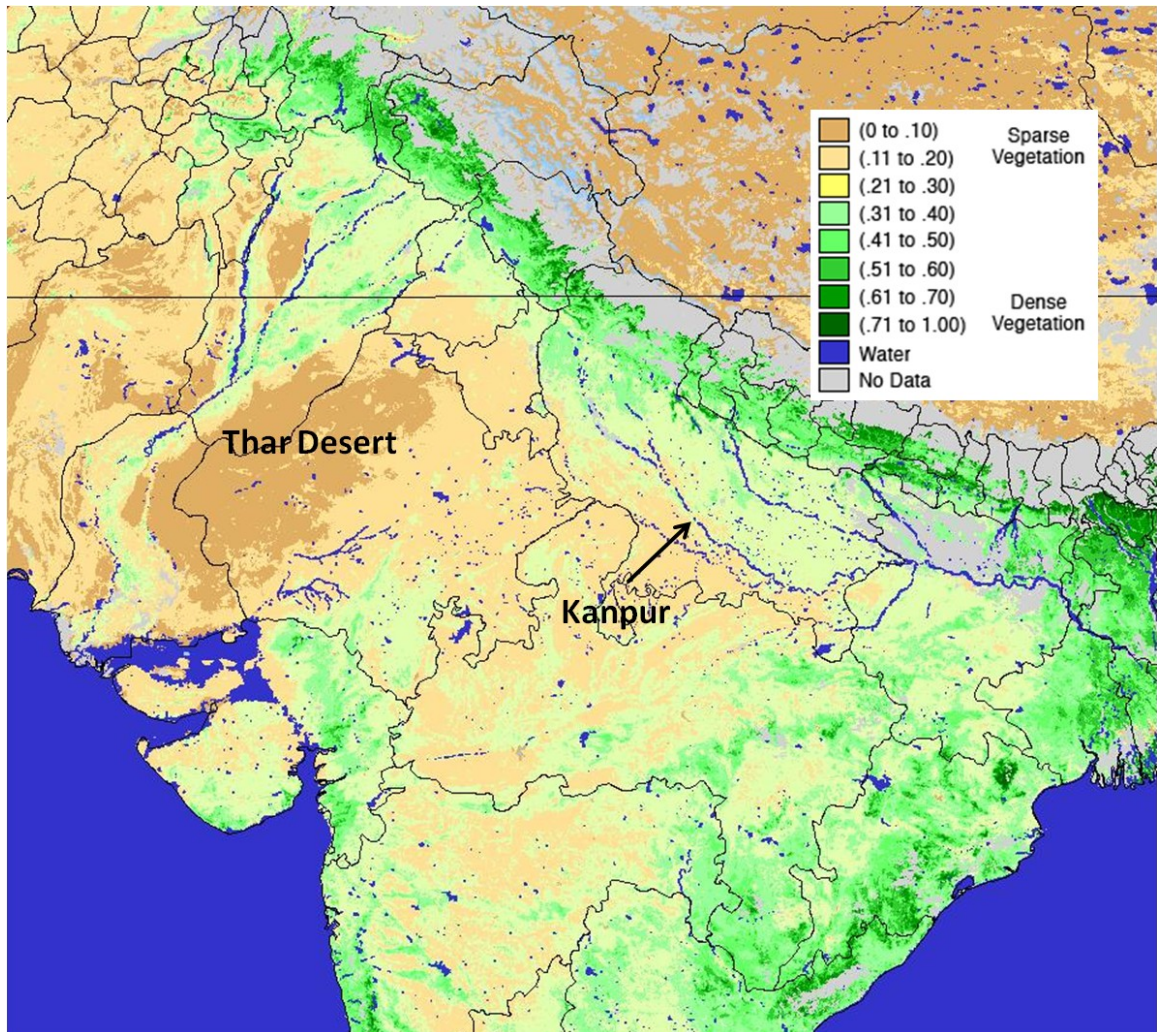


**Figure 3.1 Aqua MODIS Land Normalized Difference Vegetation Index (NDVI) 250 m product over the Indo-Gangetic Plain averaged between April 30 and May 15, 2008. Light brown and brown regions indicate areas of sparse vegetation (NDVI<0.3), while green regions indicate areas of more dense vegetation. The region around Kanpur mainly has NDVI values in the 0.11 to 0.20 range. Source: USDA/NASA/UMD Global Agricultural Monitoring (GLAM) Project.**

### 3.2 Analysis Technique

Terra and Aqua MODIS satellite data were evaluated using the TIGERZ IOP data set. Collection 5 (C005) and 5.1 (C051) processing utilizes the MODIS dark target and Deep Blue algorithms [Kaufman *et al.*, 1997; Remer *et al.*, 2005; Hsu *et al.*, 2006; Levy *et al.*, 2007b]. Retrievals of MODIS (MOD04\_L2/MYD04\_L2)  $\tau_{550\text{nm}}$  were compared to ground-based measurements of AOD interpolated to 550 nm using the linear fit of the logarithms of AOD and wavelength. The subset statistics generated from 10 km MODIS AOD granules were computed following the procedure presented by Ichoku *et al.* [2002] for a 50x50 km (5x5 pixels) box, whereas 3 km granules used a 48x48 km (16x16 pixels) box around the Kanpur AERONET site. The MODIS/AERONET matchups were performed when MODIS had at least five pixels for the overpass and AERONET had at least two observations within  $\pm 30$  minutes. Modifying the procedure to use actual geographic pixel dimensions for the bounding box or decreasing the average time from overpass for ground-based measurements had a negligible effect on statistics when compared to the method suggested by Ichoku *et al.* [2002]. Each 10 km MODIS product provided quality assurance (QA) flags to indicate the confidence level of each pixel ranging from 0 (poor) to 3 (very good) and were generated based on the presence of clouds, fitting errors, limits on AOD, and semi-bright land surface in addition to other quality checks [Remer *et al.*, 2009], although these QA flags were not available for the 3 km MODIS product.

### 3.3 Comparison of MODIS and AERONET

The Terra and Aqua MODIS comparisons for the five TIGERZ deployment days are shown in Figure 3.2 for MODIS aerosol product QA flags  $\geq 0$ . Depending on the

deployment day, sun photometer data represent Cimel and Microtops or Cimel area averages (Table 2.1). As indicated by *Remer et al.* [2008], MODIS retrievals with  $QA < 3$  are generally used for qualitative rather than quantitative purposes; however, due to the lack of  $QA = 3$  retrievals for 10 km and the 3 km products,  $0 \leq QA < 3$  flags were analyzed here. In Figure 3.2, the overpass matchups for these five days show higher MODIS  $\tau_{550nm}$  values over most of the range when compared to sun photometers consistent with *Jethva et al.* [2006]. This finding is not consistent with other studies showing MODIS AOD biases as a function of ground-based sun photometer AOD, where MODIS AOD is overestimated at low AOD and underestimated at high AOD [*Remer et al.*, 2008]; however, the small sample size here limits the robustness of the trend analysis. In this case, very high MODIS  $\tau_{550nm}$  values are likely the result of non-spherical particle scattering by dust aerosols over the semi-bright surface reducing the contrast between the atmosphere and surface [*Jethva et al.*, 2006]. In comparison to the MODIS 10 km retrievals, the MODIS 3 km retrievals show similar or better agreement with the ground-based instruments (Figure 3.2). In addition, three matchups were made on 6 May 2008 (Terra and Aqua) and 7 June 2008 (Terra). For the Terra overpass on 7 June 2008, clouds were visible in the northern portion of the 50x50 km domain when 10 km MODIS retrievals were not available; however, the immediate vicinity of Kanpur did not have clouds and allowed the retrieval of 3 km MODIS AOD pixels. Consistent with results from *Johnson et al.* [2009] and *Ginoux et al.* [2010], on 30 May 2008, the Aqua C051 Deep Blue retrieval shows improvement over the Aqua C005 Deep Blue retrieval with a reduction in  $\tau_{550nm}$  by  $\sim 0.18$  due to an improved characterization of the land surface.

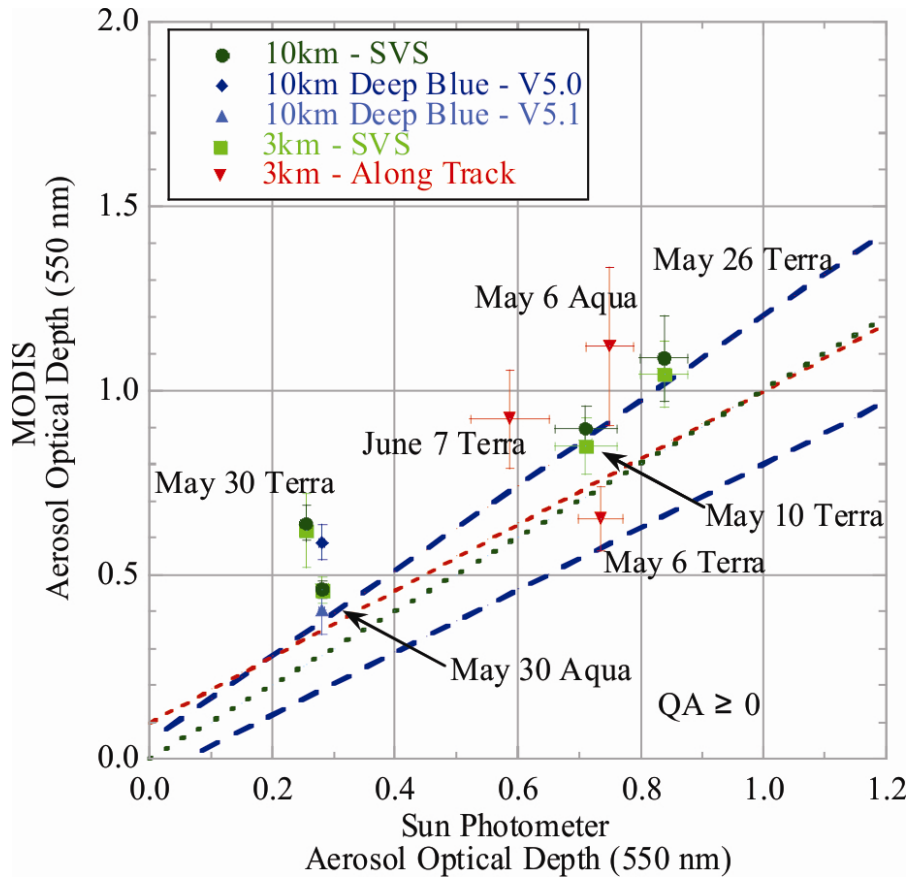


**Figure 3.2 MODIS AOD retrievals with  $QA \geq 0$  were biased high with respect to TIGERZ IOP area-averaged measurements. MODIS AOD 3 km retrievals improved spatial representativeness during some conditions (e.g., clouds) that prohibited the retrieval of 10 km products. Area-averaged MODIS (MOD04\_L2/MYD04\_L2) 3 km and 10 km  $\tau_{550nm}$  versus area-averaged sun photometer (Cimel and Microtops)  $\tau_{550nm}$  were compared for each temporary deployment. The vertical and horizontal error bars indicate standard deviations for MODIS and sun photometer area averages, respectively. The blue dashed lines indicate the calculated MODIS uncertainty compared to sun photometer AOD. The green dotted line is the one-to-one line. The red dashed line shows the trend in reported MODIS retrievals, for all AERONET sites globally, based on a several validation studies as reported by *Levy et al.* [2007b]. Figure from *Giles et al.* [2011a].**

The MODIS 10 km  $\tau_{550nm}$  was evaluated using the AERONET long-term monitoring Cimel at IIT-Kanpur during the TIGERZ IOP (1 May 2008 to 23 June 2008). Figure 3.3a shows moderate correlation between MODIS and AERONET with  $R^2$  values (and root mean square error in parentheses) of 0.52 (0.12), 0.69 (0.11), and 0.68 (0.17)

for Terra-MODIS, Aqua-MODIS, and Aqua-Deep Blue MODIS, respectively. These correlations with respect to other validation exercises at Kanpur were slightly lower than those reported by *Tripathi et al.* [2005a] ( $R^2 = 0.72$ ) for dust events using MODIS Collection 4 (C004) Level 2 data set in 2004, higher than those reported by *Prasad and Singh* [2007b] ( $R^2 = 0.29$ ) using C004 Level 3 MODIS AOD during the pre-monsoon season (April-June), and lower than those reported by *Jethva et al.* [2007b] ( $R^2 = 0.83$ ) for MODIS C005 from 2002 to 2005. Furthermore, the MODIS and AERONET correlations are similar to those reported by *Dey and Di Girolamo* [2010] ( $R^2 = 0.69$ ) for Multiangle Imaging Spectroradiometer (MISR) over Kanpur from 2001 to 2008, higher than those reported by *Kar et al.* [2010] ( $R^2 = 0.25$ ) for CALIPSO over Kanpur from 2006 to 2009, and similar to those reported by *Hyer et al.* [2011] ( $R^2 = 0.71$ ) for MODIS C005 Level 2 data compared to all AERONET sites on the Indian sub-continent from 2005 to 2008. The Terra and Aqua-MODIS retrievals had better agreement with AERONET within the stated MODIS uncertainty [*Remer et al.*, 2008] than Aqua-Deep Blue retrievals for  $QA \geq 0$ . In Figure 3.3a, the linear regression through each standard MODIS retrieval suggests an overestimation at low  $\tau_{550nm}$  and underestimation at high  $\tau_{550nm}$  with the inflection point near 0.45; this result is a well-known bias in the MODIS retrieval and depends on particle size distribution, shape, and absorption [*Ichoku et al.*, 2005; *Levy et al.*, 2005; *Remer et al.*, 2005]. The linear regression for the Aqua Deep Blue retrieval gives a slope near 1.0 and high offset of  $\sim 0.29$  due to issues with the assumed bidirectional reflectance distribution function (BRDF) model over the Kanpur region.

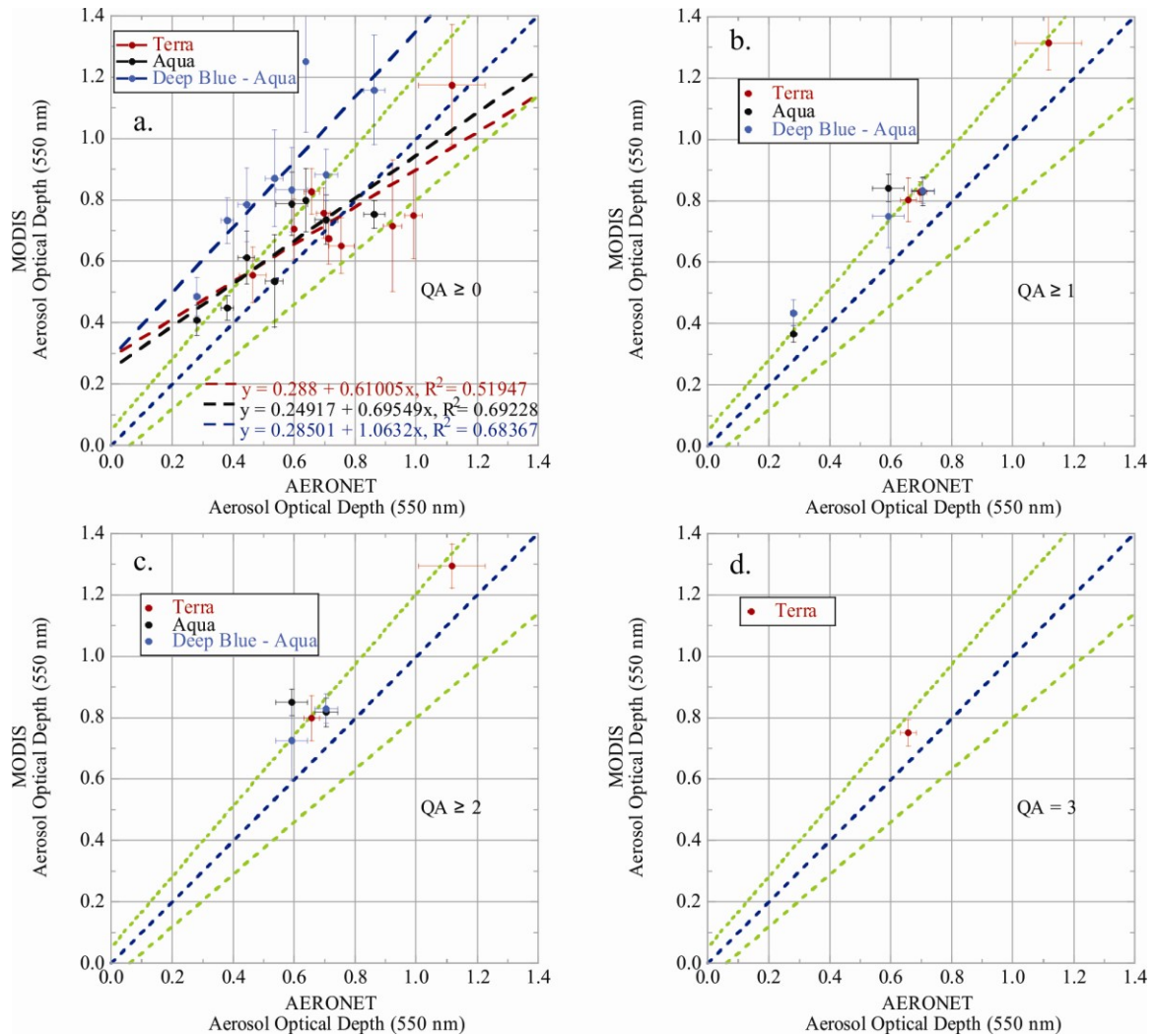


**Figure 3.3 MODIS AOD 10 km retrievals with the lowest quality assurance (QA≥0) had moderate correlation with the Kanpur AERONET site, whereas retrievals with QA>0 were limited in number over the semi-bright land surface. Area-averaged MODIS (MOD04\_L2/MYD04\_L2) 10 km  $\tau_{550\text{nm}}$  versus Kanpur AERONET  $\tau_{550\text{nm}}$  compared from 1 May to 9 June 2008, and partitioned for each QA level ≥0 (a), ≥1 (b), ≥2 (c), and 3 (d) for the Terra MODIS, Aqua MODIS, and Aqua Deep Blue MODIS algorithms. The vertical and horizontal error bars indicate the standard deviation for the MODIS area-average and AERONET temporal average, respectively. Figure from *Giles et al.* [2011a].**

Quality assurance flags 1, 2, and 3, representing increased confidence in the retrieved pixel, were evaluated and used to remove significant portions of the MODIS data. In Figure 3.3b-d, higher quality retrievals show all MODIS products were biased high when compared to AERONET. For these overpasses, significant cloud cover was

not identified by either on-site observers or by manual inspection of MODIS Rapid Response true color images generated for the Kanpur AERONET site. On 18 May 2008, dust over the semi-bright surface reduced the aerosol to surface contrast and resulted in no Terra/MODIS aerosol retrievals on this cloud-free day, while Level 2.0 AERONET measurements were available during the overpass time. The MISR instrument had one cloud-free scene on 18 May 2008, where MISR retrieved a  $\tau_{558\text{nm}}$  of 0.70 [*R. Kahn personal communication*, 2010] and the corresponding AERONET Kanpur interpolated  $\tau_{558\text{nm}}$  was 0.72 for  $\pm 30$  minutes of the Terra overpass at 05:15 UTC. However, *Dey and Di Giorlamo* [2010] showed that MISR AOD typically underestimated Kanpur AERONET observations when analyzing all seasons similar to results from *Kahn et al.* [2005] and *Prasad and Singh* [2007b].

Further investigation of the ground-based data revealed that some data were removed by the AERONET cloud-screening algorithm during cloud-free periods when aerosols were primarily dust. Dust occasionally exhibits a similar spectral AOD signature to spectral cloud optical depth by having almost no spectral dependence and high triplet variability causing the AERONET cloud-screening algorithm to misclassify dust as cloud [*Smirnov et al.*, (2000)]. During over-cloud-screened days, Level 1.0 AOD data were inspected for anomalies, verified with observer sky condition logs, and incorporated into the MODIS overpass comparison to provide additional valid points. Potential MODIS days were based on retrievals made for  $QA \geq 0$  during mainly cloud-free and low aerosol loading conditions. Re-inspected AERONET data provided 29 additional validation points within  $\pm 30$  minutes of MODIS overpass for MODIS/AERONET matchups between 1 May 2008 and 23 June 2008. Reconstituted

AERONET points (within  $\pm 30$  minutes of satellite overpass) increased observations available for four previously identified MODIS/AERONET matchups (i.e., one for Terra and three for Aqua) and added two or more AERONET validation points to enable six additional potential MODIS/AERONET matchups (i.e., four for Terra and two for Aqua). As a result, these additional AERONET validation points increased the potential MODIS/AERONET matchups by 24% from 25 to 31 (Table 3.1). During the period, 55 MODIS retrieval days were possible over Kanpur; however, less than 50% of the overpass days (18 days for Terra and 20 days for Aqua) were retrieved by MODIS due to clouds, elevated dust, or surface reflectance issues. In summary, both AERONET and MODIS algorithms occasionally misclassified dust as clouds, and additionally, semi-bright surface effects sometimes resulted in screening by the MODIS algorithm over the IGP during the pre-monsoon.

**Table 3.1 Potential and actual MODIS, AERONET Level 2.0 (L2), and Level 2.0 + Level 1.0 screened (L2+L1) matchups from 1 May to 23 June 2008. Table from Giles *et al.* [2011a].**

Matchups	Potential MODIS	Potential AERONET L2	Potential AERONET L2+L1	Actual
Satellite	Days	Days	Days	Days
Terra	18	9	13	9
Aqua	20	16	18	8

The evaluation of MODIS aerosol products over the IGP has shown the need for additional algorithm or parameterization improvements. MODIS retrievals for C005 and C051 overestimated and under-sampled aerosol properties when compared to TIGERZ IOP measurements at Kanpur; this is consistent with MODIS C004 retrieval biases identified by *Jethva et al.* [2007a] over the IGP during the pre-monsoon. However,

*Jethva et al.* [2007b, 2010] have adjusted both the absorbing aerosol model assumed by the MODIS C005 algorithm and the surface reflectance to produce more accurate retrievals. Although spatially distributed MODIS aerosol retrievals are commonly compared to ground-based sun photometer point measurements, the TIGERZ IOP has provided a unique data set on the same spatial scale to provide a more robust validation of satellite retrievals.

## Chapter 4: Dominant Absorbing Aerosol Types over Kanpur

*Reproduced by permission of American Geophysical Union.*

### 4.1 Motivation

Single scattering albedo (SSA) retrievals from AERONET have been compared to surface-based and airborne in situ measurements in atmospheric environments affected by biomass burning emissions, dust, or mixtures of them. *Leahy et al.* [2007], *Johnson et al.* [2009], *Müller et al.* [2010], and *Toledano et al.* [2011] show that spectral SSA differences between AERONET and in situ retrievals were well within uncertainty estimates. However, ground-based in situ measurements may exhibit large diurnal variability in SSA due to anthropogenic processes and boundary layer meteorology [Garland et al., 2008]. The spectral SSA [ $\omega_o(\lambda)$ ] and extinction AOD [ $\tau_{\text{ext}}(\lambda)$ ] relate to the absorption AOD [ $\tau_{\text{abs}}(\lambda)$ ] as given in equation (8). Analogous to the extinction Ångström exponent ( $\alpha_{\text{ext}}$ ) in equation (3), the absorption Ångström exponent ( $\alpha_{\text{abs}}$ ) is derived using equation (9).

$$\alpha_{\text{abs}} = -\text{dln}[\tau_{\text{abs}}(\lambda)]/\text{dln}(\lambda) \quad (9)$$

$\alpha_{\text{abs}}$  is calculated for the inclusive wavelength range from 440 to 870 nm. The linear fit of  $\tau_{\text{abs}}$  versus  $\lambda$  on a logarithmic scale cannot differentiate among particle types alone. Comparing  $\alpha_{\text{abs}}$  to an aerosol size proxy (e.g.,  $\alpha_{\text{ext}}$  or  $\eta_{675\text{nm}}$ , the fine mode fraction of AOD at 675 nm from the almucantar retrieval) relates particle absorption spectral dependence to particle size and potentially characterizes the dominant absorbing particle type or optical mixture. Assuming a spectrally constant refractive index, *Bergstrom et al.* [2002] suggested that small BC particles ( $r < 0.01 \mu\text{m}$ ) will have a  $\lambda^{-1}$  dependence or  $\alpha_{\text{abs}}$  of 1.0, whereas larger, optically effective BC particles ( $r > 0.01 \mu\text{m}$ ) will have  $\alpha_{\text{abs}}$  of 1.3.

Deviations from these  $\alpha_{\text{abs}}$  values occur when spectral changes in the imaginary part of the refractive index vary due to the composition of the aerosol particle [Kirchstetter *et al.*, 2004]. From Nuclepore filter measurements collected 50 km east-southeast of Beijing, China, Chaudhry *et al.* [2007] demonstrated that coarse mode particles with diameters ranging between 2.5  $\mu\text{m}$  and 10  $\mu\text{m}$  had a subtle increase in absorption from 350 nm to 600 nm. Bergstrom *et al.* [2007] showed that aerosol particles from different regions have distinct  $\alpha_{\text{abs}}$  values (e.g.,  $\alpha_{\text{abs}} = \sim 2.3$  for Saharan dust and Asian dust/pollution mixtures,  $\alpha_{\text{abs}} = \sim 1.5$  for South Africa biomass burning, and  $\sim 1.1$  for urban/industrial.). Lewis *et al.* [2008] also showed that  $\alpha_{\text{abs}}$  for biomass burning particles varies by fuel type, combustion phase, and organic to black carbon ratio. Russell *et al.* [2010a] used AERONET Version 1 almucantar retrieval data from Dubovik *et al.* [2002] to show dust separated from other discrete aerosol types using the  $\alpha_{\text{abs}}$  versus  $\alpha_{\text{ext}}$  (hereafter defined as “ $\alpha_{\text{abs}}/\alpha_{\text{ext}}$ ”) relationship to classify data clusters (e.g.,  $\alpha_{\text{abs}} = \sim 1.2$  to  $\sim 3.0$  for dust,  $\alpha_{\text{abs}} = \sim 1.2$  to  $\sim 1.5$  for biomass burning, and  $\alpha_{\text{abs}} = \sim 0.75$  to  $\sim 1.3$  for urban/industrial), although particles with absorption dominated by BC content (i.e., urban and biomass burning aerosols) were less defined and required more information [Giles *et al.*, 2010].

#### 4.2 Aerosol Absorption and Size Relationships

Both the  $\alpha_{\text{abs}}/\alpha_{\text{ext}}$  and  $\alpha_{\text{abs}}$  versus  $\eta_{675\text{nm}}$  (hereafter defined as “ $\alpha_{\text{abs}}/\eta_{675\text{nm}}$ ”) relationships were examined with AERONET Version 2, Level 2.0 AOD and almucantar retrievals for Kanpur. For all months from 2002 to 2008, the  $\alpha_{\text{abs}}/\alpha_{\text{ext}}$  and  $\alpha_{\text{abs}}/\eta_{675\text{nm}}$  relationships (Figure 4.1a and Figure 4.1c) show a non-linear dependence over the aerosol size ranges, whereas the sphericity fraction, generally valid for only  $\alpha_{\text{ext}} < 1.0$  according to Dubovik *et al.* [2006], has a strong transition from non-spherical to spherical

particles around  $\alpha_{\text{ext}}$  of  $\sim 1.3$  or  $\eta_{675\text{nm}}$  of  $\sim 0.66$ . The “Mostly Dust” category [i.e.,  $\alpha_{\text{ext}} \leq 0.5$  ( $\eta_{675\text{nm}} \leq 0.33$ ) and sphericity fraction  $< 0.2$ ] with  $\alpha_{\text{abs}} > 2.0$  and the “Mostly BC” category [i.e.,  $\alpha_{\text{ext}} > 0.8$  ( $\eta_{675\text{nm}} > 0.66$ ) and sphericity fraction  $\geq 0.2$ ] with  $1.0 < \alpha_{\text{abs}} \leq 2.0$  are consistent with results reported by *Bergstrom et al.* [2007] and *Russell et al.* [2010a].

The “Mostly Dust” category identifies aerosol mixtures where iron oxide in dust is the dominant absorber and the “Mostly BC” category represents a mixture of biomass burning and urban/industrial emissions with BC as the dominant absorber, although other absorbers such as brown carbon and soot carbon may exist [*Gustafsson et al.*, 2009]. The  $\alpha_{\text{ext}} > 0.8$  ( $\eta_{675\text{nm}} > 0.66$ ) and  $\alpha_{\text{abs}} > 2.0$  may indicate a greater organic carbon concentration [*Arola et al.*, 2011]. The  $\alpha_{\text{abs}}/\alpha_{\text{ext}}$  and  $\alpha_{\text{abs}}/\eta_{675\text{nm}}$  relationships during the pre-monsoon (Figure 4.1b and Figure 4.1d) revealed the dominance of large particles with  $\alpha_{\text{abs}}$  ranging mainly from 1.25 to 3.0. Centered on the maximum density at  $\alpha_{\text{ext}} \sim 0.5$  ( $\eta_{675\text{nm}} \sim 0.33$ ) with  $\alpha_{\text{abs}} \sim 1.5$ , the “Mixed BC and Dust” category likely represents an optical mixture of fine mode BC and coarse mode dust as the dominant absorbers. Notably, these classifications are complicated by the fact that 6% of the Kanpur Level 2.0 data set (2002-2008) had  $\alpha_{\text{abs}} < 1.0$ , where  $\alpha_{\text{abs}} \sim 1.0$  is often identified as indicative of exclusively BC absorption. *Bergstrom et al.* [2007] showed that  $\alpha_{\text{abs}} < 1.0$  occurred frequently in Particle Soot Absorption Photometer (PSAP) data and suggested that the imaginary refractive index may decrease with wavelength due to absorption AOD spectral dependence or the low  $\alpha_{\text{abs}}$  values are related to measurement uncertainties. For AERONET data,  $\alpha_{\text{abs}} < 1.0$  may be related to higher SSA retrieval uncertainty for low aerosol loading cases [*Dubovik et al.*, 2000; *Giles et al.*, 2010], non-linearity of absorption optical depth [*Eck et al.*, 2010], the quality of the almucantar measurement

sequence, and the spectral range chosen for the calculation [*Lack and Cappia* 2010].

Some  $\alpha_{\text{abs}} < 1.0$  cases at Kanpur revealed potential measurement inconsistencies between sun and sky collimators (e.g., spider webs or dust) or possible diffuse cloud contamination (e.g., uniform optically thin cirrus). *Kirchstetter et al.* [2004] reported  $\alpha_{\text{abs}}$  values below 1.0 for similar wavelength regions using in situ measurements, therefore some AERONET retrievals with  $\alpha_{\text{abs}} < 1.0$  may be the result of actual spectral variation.

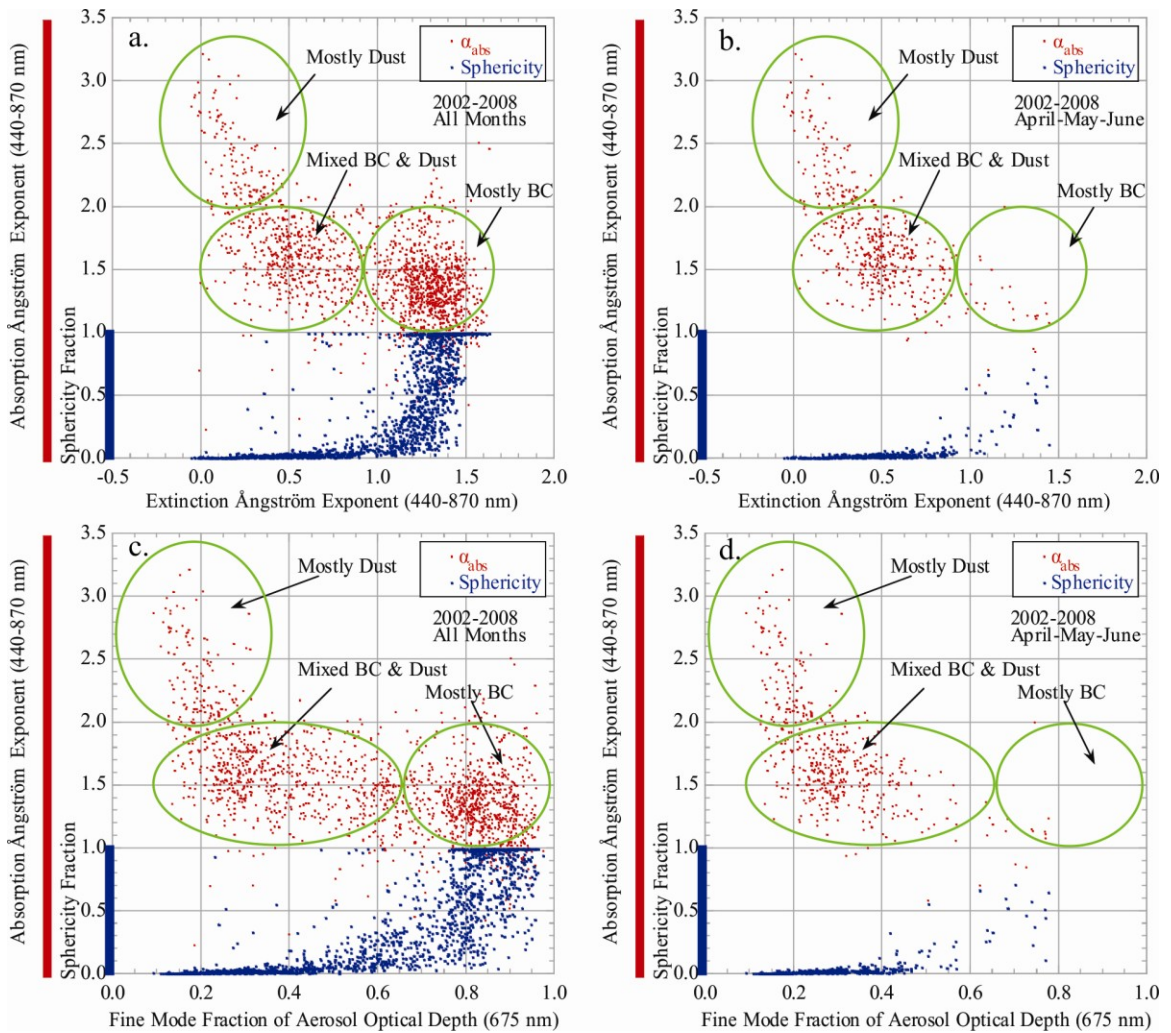


**Figure 4.1** Level 2.0 absorption Ångström exponent ( $\alpha_{\text{abs}}$ ) and sphericity fraction as a function of extinction Ångström exponent ( $\alpha_{\text{ext}}$ ) and fine mode fraction of AOD at 675 nm ( $\eta_{675\text{nm}}$ ; from the almucantar inversions) from the Kanpur AERONET record (2002-2008) in all seasons (a,c) and April-May-June (b,d).  $\alpha_{\text{abs}}$  is plotted from 0.0 to 3.5 (in red) and sphericity fraction is plotted from 0.0 to 1.0 (in blue). The green ellipses represent probable aerosol mixture categories.  $\alpha_{\text{abs}}$  of 1.0 indicates  $\lambda^{-1}$  dependence and a sphericity fraction of 1.0 indicates a 100% spherical particle. Figure from *Giles et al. [2011a]*.

### 4.3 Absorption Wavelength Dependence Effects on Aerosol Properties

Remotely sensed aerosol retrievals cannot determine whether BC coats dust; however, the likelihood for this interaction increases over the IGP during the pre-monsoon and results from *Arimoto et al. [2006]* and *Guo et al. [2010]* in China and *Dey*

*et al.* [2008] and Figure 4.2 in India suggest this interaction is likely. The volume size distribution and SSA retrievals were binned based on  $\alpha_{\text{abs}}$  (Figure 4.3). As  $\alpha_{\text{abs}}$  decreases to 1.0, coarse mode particles became less dominant for both the annual cycle and pre-monsoon (Figure 4.3a and Figure 4.3c). In Figure 4.3b and Figure 4.3d, SSA transitioned from spectra representing dust (i.e., typical iron oxide absorption in the blue wavelength region and relatively weak absorption in the near-infrared) to urban/industrial pollution containing BC (i.e., stronger absorption in longer wavelengths); the interpretation of these SSA spectra are consistent with results reported by *Dubovik et al.* [2002], *Singh et al.* [2004], *Eck et al.* [2003a, 2003b, 2005, 2008, 2009], *Prasad and Singh* [2007a], and *Derimian et al.* [2008]. Single scattering albedo binned by  $\alpha_{\text{abs}}$  was further partitioned based on the  $\alpha_{\text{ext}}$  intervals of 0.0-0.8 and 0.8-2.0 and  $\eta_{675\text{nm}}$  intervals of 0.0-0.33, 0.33-0.66, and 0.66-1.0 (Figure 4.4). Strong absorption is noted at 440 nm relative to longer wavelengths due to large dust particles, but increasing absorption at longer wavelengths indicates a greater absorption contribution by fine mode BC. For nearly 75% of cases, mainly large particles ( $\alpha_{\text{ext}} \sim 0.0-0.8$ ) were classified as “Mixed BC and Dust” whereas the other 25% of cases were classified as “Mostly Dust” (see Figure 4.1a approximate ellipses). For nearly 75% of cases, mainly small particles ( $\alpha_{\text{ext}} \sim 0.8-2.0$ ) were classified as “Mostly BC” (for  $\alpha_{\text{abs}} \leq 1.5$ ), whereas the other 25% of the cases were classified as “Mixed BC and Dust”. Using Figure 4.4, the “Mixed BC and Dust” classification represents  $\sim 40\%$  of the Kanpur data set. Further,  $\sim 33\%$  of retrievals were classified as “Mostly Dust” and 67% as “Mixed BC and Dust” for coarse mode particles ( $\eta_{675\text{nm}} \leq 0.33$ ), whereas, by definition, all of the retrievals were classified as “Mostly BC and Dust” for mixed size particles ( $0.33 < \eta_{675\text{nm}} \leq 0.66$ ) and “Mostly BC” for fine mode

particles ( $\eta_{675\text{nm}} > 0.66$ ). The optical mixture of dust transported over or mixed with pollution dominates during the pre-monsoon, and the small particle dominated optical mixtures are consistent with pollution occurring during winter [Singh *et al.*, 2004].

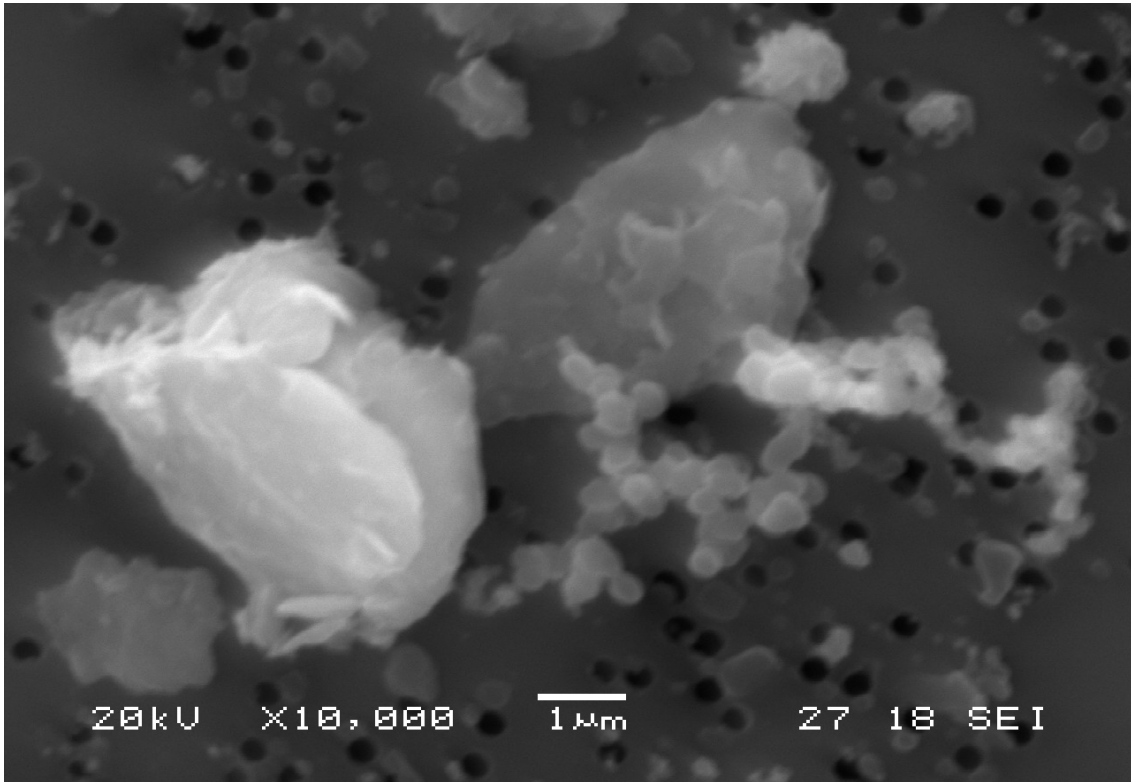


**Figure 4.2** Scanning electron microscope image analyzed using filter samples taken at IIT-Kanpur on 10 May 2008. The image shows large dust particles with  $\sim 2 \mu\text{m}$  radii and an open black carbon particle cluster (as shown by *Martins et al.* [1998]) with individual particle radii likely between  $\sim 0.1 \mu\text{m}$  and  $0.2 \mu\text{m}$ . These black carbon particles have similar radii to the aerosol volume size distribution fine mode peak in Figure 4.3 (a,c) for  $\alpha_{\text{abs}}$  less than 2.0. Image courtesy of Vanderlei Martins and Adriana Lima (UMBC).

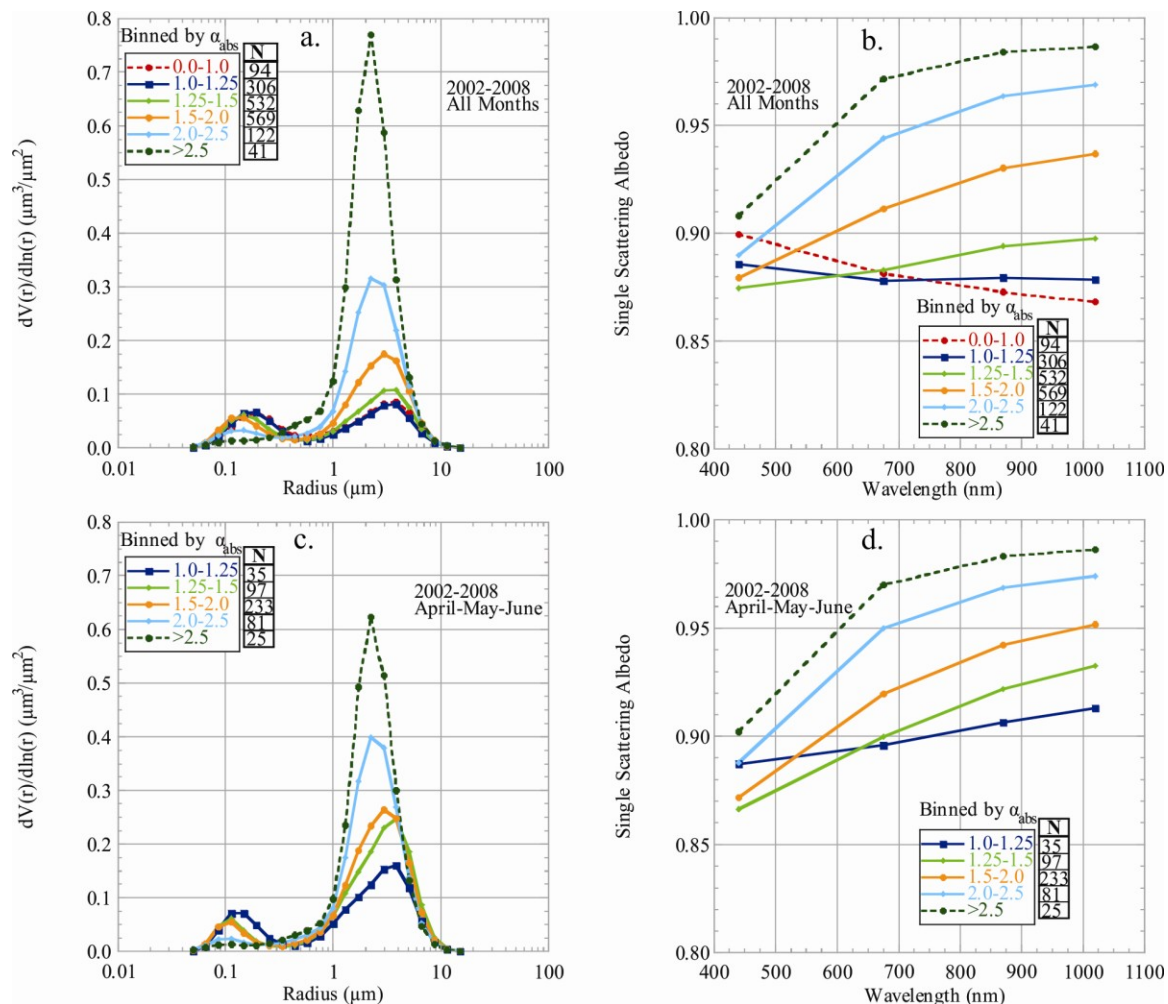


**Figure 4.3** As absorption Ångström exponent decreased to 1.0, coarse mode particles became less dominant for both the annual cycle and pre-monsoon. Further, single scattering albedo transitioned from spectra representing dust (i.e., typical iron oxide absorption in the blue wavelength region and relatively weak absorption in the near-infrared) to urban/industrial pollution containing black carbon (i.e., stronger absorption in longer wavelengths). Level 2.0 almucantar retrievals from the Kanpur AERONET (2002-2008) all years (a, b) and April-May-June (c, d) for aerosol volume size distribution (a,c) and SSA (b,d) averaged by  $\alpha_{abs}$  bins. Averages with  $N < 25$  were removed from the plots. Figure from *Giles et al. [2011a]*.

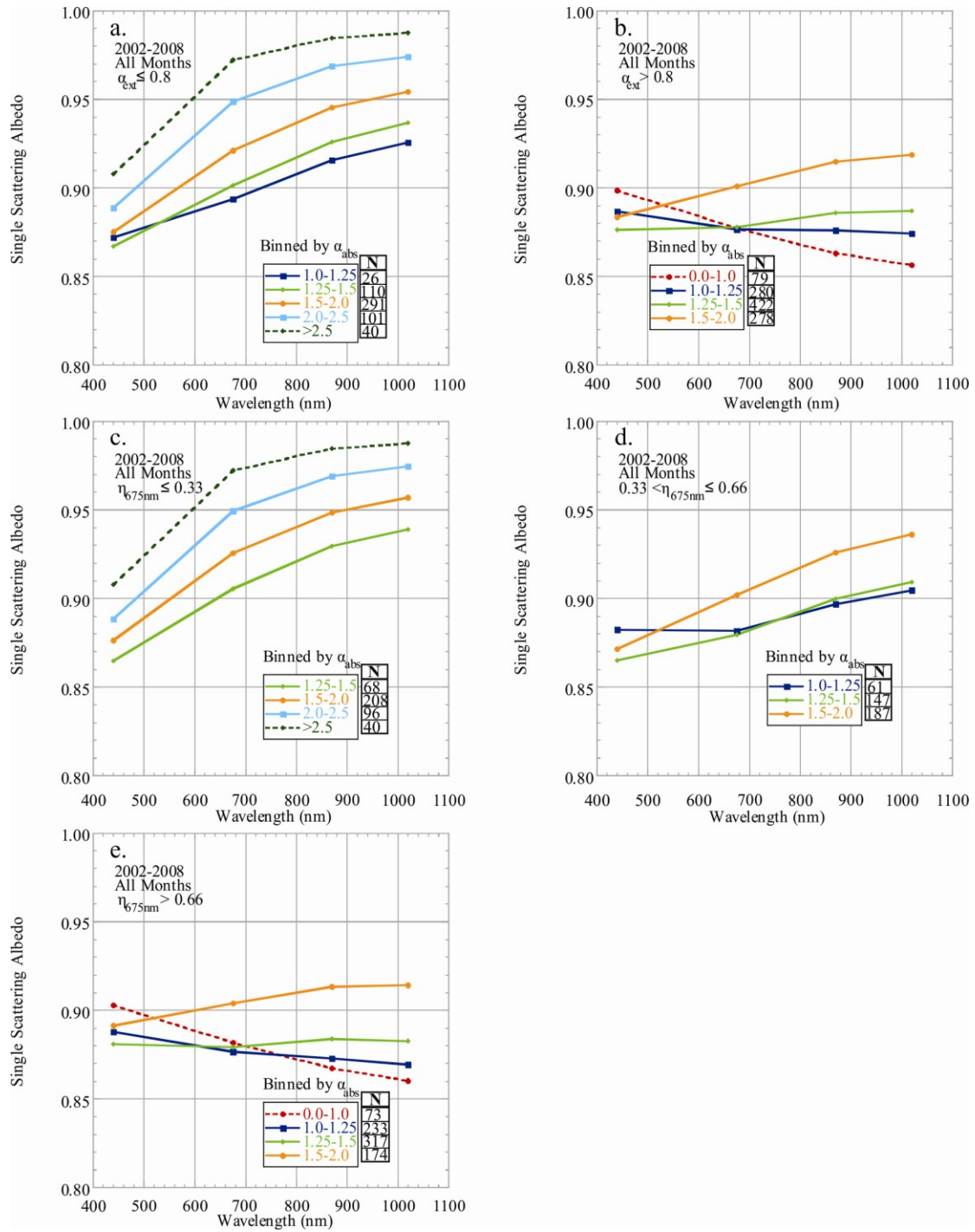


**Figure 4.4** Level 2.0 SSA data were averaged for  $\alpha_{abs}$  bins and further partitioned based on  $\alpha_{ext}$  and  $\eta_{675nm}$  using Kanpur AERONET (2002-2008). (a) represents the case for large particle dominated conditions (i.e.,  $\alpha_{ext} \leq 0.8$ ) and (b) represents the case for small particle dominated conditions (i.e.,  $\alpha_{ext} > 0.8$ ). (c) represents mainly coarse mode particles ( $\eta_{675nm} \leq 0.33$ ), (d) represents mixed size particles ( $0.33 < \eta_{675nm} \leq 0.66$ ), and (e) represents mainly fine mode particles ( $\eta_{675nm} > 0.66$ ). Averages with  $N < 25$  were removed from the plots. Figure from Giles *et al.* [2011a].

## Chapter 5: Classifications of Aerosol Dominant Mixing States and Origins

*Reproduced by permission of American Geophysical Union.*

### 5.1 Motivation

Particles suspended in the atmosphere are difficult to characterize both temporally and spatially due to their short lifetime and geographically diverse sources. Aerosol mixtures—whether dominated by dust, sulfate, carbon, sea salt, or mixtures of these particles—pose a challenge to satellite and sub-orbital remote sensing techniques when identifying aerosol type [Jeong and Li 2005; Levy *et al.*, 2007a; Kalapureddy *et al.*, 2009; Lee *et al.*, 2010; Kahn *et al.*, 2010; Russell *et al.*, 2010a]. Remote sensing techniques can quantify the aerosol particle size using spectral aerosol optical properties, but inferring aerosol type requires knowledge of the source regions usually obtained through use of ancillary data sets (e.g., back trajectory models, satellite product, and electron microscopy) to determine emission sources, transport mechanisms, composition, and morphology. The discrimination of aerosol types increases accuracy of the assessment of the aerosol radiative impact and therefore is important to climate modeling [Diner *et al.*, 1999; Satheesh and Moorthy 2005]. Variations in spectral aerosol absorption magnitudes can enable partitioning among aerosols from various source regions, fuel types, or combustion phases. Aerosol absorption together with size can potentially determine dominant aerosol types from remote sensing and in situ measurements.

Various methods have been proposed using aerosol optical and microphysical properties to distinguish aerosol types. The magnitude of the aerosol optical depth (AOD,  $\tau_{\text{ext}}$ ) and the spectral dependence of AOD with respect to wavelength (i.e.,

Ångström exponent,  $\alpha_{\text{ext}}$ ) is commonly used in aerosol remote sensing to infer dominant aerosol types given knowledge of the source region or typical aerosol transport mechanisms [e.g., *Kalapureddy et al.*, 2009, *Boselli et al.*, 2012]. Other techniques using the derivative of the Ångström exponent or spectral difference of Ångström exponent wavelength pairs along with aerosol loading and particle effective radius may provide further information on particle type with respect to size and growth of particles [*Gobbi et al.*, 2007; *Basart et al.*, 2009]. Although size varies among particle types, the spectral absorption also varies. Studies [*Omar et al.*, 2005; *Levy et al.*, 2007a; *Mielonen et al.*, 2009; *Lee et al.*, 2010; *Russell et al.*, 2010a] have suggested relationships utilizing the aerosol absorption and size properties to determine the dominant aerosol type from Aerosol Robotic Network (AERONET) retrievals [*Holben et al.*, 1998; *Dubovik et al.*, 2000, 2002, 2006]. Information content from these relationships varies from generic identification of major aerosol particle types (e.g., dust, mixed, urban/industrial pollution, and biomass burning smoke) to specific degrees of absorbing aerosols. Recently, *Russell et al.* [2010a] have proposed using the absorption Ångström exponent (AAE,  $\alpha_{\text{abs}}$ ), the spectral absorption aerosol optical depth dependence on wavelength, to further define aerosol type from AERONET retrievals. For comparison to the Cloud-Aerosol Lidar with Orthogonal Polarization (CALIOP) instrument, *Mielonen et al.* [2009] utilized the AERONET single scattering albedo ( $\omega_0$ ) difference between 440 and 1020 nm (as suggested by *Bergstrom et al.* [2002] and implemented by *Derimian et al.* [2008]) and  $\alpha_{\text{ext}}$  to estimate aerosol type. Further, *Lee et al.* [2010] modified this relationship to use only  $\omega_0$  from 440 nm and the fine mode fraction ( $\eta$ ) of the AOD at 550 nm to determine the particle size partitioning. Other techniques using spectral lidar ratios and multiple

aerosol optical and microphysical properties retrieved from AERONET have been implemented to determine aerosol type categories for various applications [Catrall *et al.*, 2005; Omar *et al.*, 2005; Qin and Mitchell 2009; Burton *et al.*, 2012].

## 5.2 Methodology

Nineteen AERONET sites were selected for the analysis based on the availability of an extensive data record (i.e., greater than five data equivalent years of AOD measurements from 1999 to 2010) and the geographic distribution among aerosol source regions (Figure 5.1). The sites were designated as one of four commonly used aerosol classifications: Dust, Mixed, Urban/Industrial (U/I), and Biomass Burning (BB). The classifications were established based on the source regions and known seasonal changes in aerosol type over these regions (see references in Table 5.1). Further, these selected sites should be subject to high aerosol loading (i.e.,  $\tau_{440\text{nm}} > 0.4$ ) to meet the Version 2, Level 2.0 almucantar retrieval sensitivity requirement for absorption parameters (e.g.,  $\omega_o$ ,  $\tau_{\text{abs}}$ ) [Dubovik *et al.*, 2000; Holben *et al.*, 2006]. Sea salt (as well as biogenic) aerosols as a dominant particle type category were not considered in this study since  $\tau_{500\text{nm}}$  is typically less than 0.1 for pure maritime environments [Smirnov *et al.*, 2002]; however, for maritime locations affected by aerosol plumes (e.g., Saharan dust transport over Cape Verde islands),  $\tau_{440\text{nm}} > 0.4$  can be satisfied [Smirnov *et al.*, 2009]. Hence, the  $\tau_{440\text{nm}} > 0.4$  criterion biases the data set only to high aerosol loading periods to ensure enough radiometric sensitivity to compute absorption reliably [Dubovik *et al.*, 2002]. Although Dust, U/I, and BB categories may represent the dominant aerosol type, episodic aerosol incursions outside of their classification category likely have occurred at any site during the analysis period (e.g., dust over Shirahama or Lake\_Argyle, biomass burning smoke

over NASA Goddard Space Flight Center (GSFC)) [Sano *et al.*, 2003; Qin and Mitchell 2009; Eck *et al.*, 2003b; O'Neill *et al.*, 2005]. The Mixed aerosol category encompasses sites primarily affected by different mixtures of aerosol types (e.g., dust and pollution or dust and biomass burning smoke mixtures) on a seasonal basis, increasing the probability of at least an optical mixture state [Derimian *et al.*, 2006; Eck *et al.*, 2010]. Although no explicit seasonal partitioning is performed, the  $\tau_{440\text{nm}} > 0.4$  criterion captures mainly seasonal increases in aerosol loading at some sites (e.g., GSFC and Mongu) [Holben *et al.*, 2001].

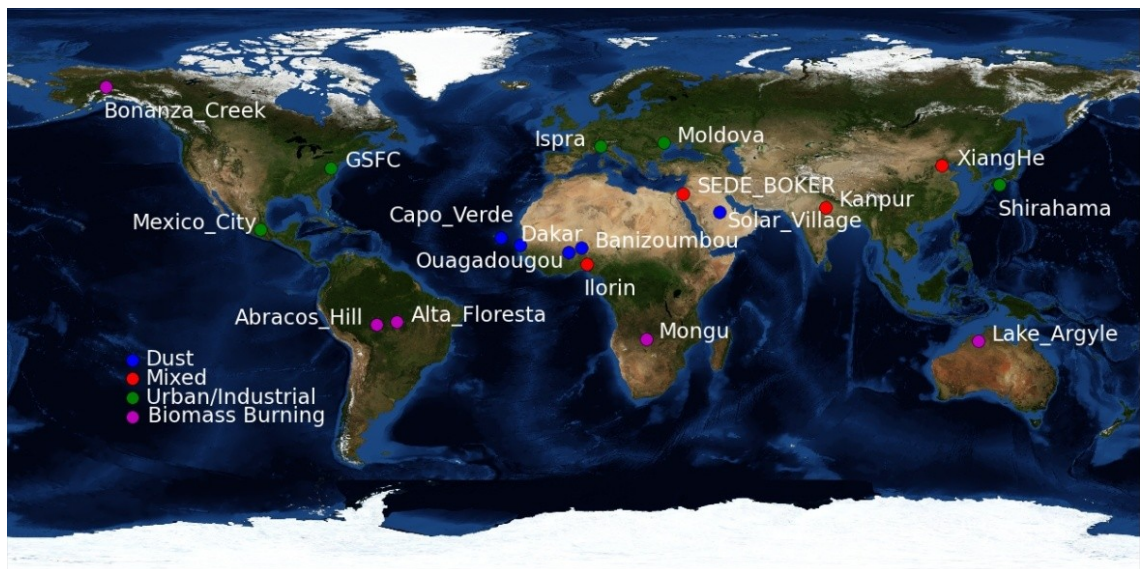


**Figure 5.1** Distribution of the AERONET sites based on the dominant particle type. Sites were selected based on data volume, geographic location, and primary aerosol source region. Other dominant particle types (e.g., sea salt and biogenic aerosols) were not considered due to low aerosol loading conditions ( $\tau_{440\text{nm}} \leq 0.4$ ), which was a limiting threshold for AERONET Version 2, Level 2.0 aerosol absorption retrievals [Dubovik *et al.*, 2002; Holben *et al.*, 2006]. Figure from Giles *et al.* [2012].

**Table 5.1 Previous studies identifying regional aerosol sources affecting AERONET sites. Table from Giles et al. [2012].**

Aerosol Type Source Regions	Affected AERONET Sites	Selected References
Most Regions with Various Types	Most Sites	<i>Holben et al. [2001]</i>
Dust - African	Banizoumbou, Capo Verde, Dakar,	<i>Tanre et al. [2001]; Reid et al. [2003]</i>
Dust - Asian	Ouagadougou, XiangHe, Shirahama	<i>Eck et al. [2005]</i>
Smoke -Amazonia	Abracos Hill, Alta Floresta	<i>Eck et al. [2003b]; Schafer et al. [2008]</i>
Smoke - Australian	Lake_Argyle	<i>Mitchell et al. [2006]</i>
Smoke - Boreal	Bonanza Creek	<i>Eck et al. [2009]</i>
Smoke - African	Mongu	<i>Eck et al. [2003a, 2003b]</i>
Pollution - Europe	Ispra	<i>Melin and Zibordi [2005]</i>
Mixed - Asia	XiangHe, SEDE_BOKER	<i>Derimian et al. [2006]; Eck et al. [2010]; Yang et al. [2009]</i>
Mixed - India	Kanpur	<i>Dey et al. [2004]; Singh et al. [2004]; Prasad et al. [2007]; Giles et al. [2011a]</i>
Mixed - Africa	Ilorin	<i>Eck et al. [2010]</i>

The Aerosol Robotic Network is a ground-based network of standardized Cimel Sun and sky scanning radiometers measuring AOD at multiple wavelengths from 340 to 1640 nm and retrieving other columnar optically effective aerosol properties (e.g., volume size distribution, complex index of refraction, and single scattering albedo) from sky radiance measurements at four wavelengths: 440, 675, 870, and 1020 nm [Holben et al., 1998]. The AOD estimated uncertainty varies spectrally from  $\pm 0.01$  to  $\pm 0.02$  with the highest error in the ultraviolet wavelengths [Holben et al., 1998; Eck et al., 1999] and calibrated sky radiance measurements typically have an uncertainty less than 5% [Holben

*et al.*, 1998]. Further descriptions of the instrumentation, calibration, methodology, data processing, and data quality are described elsewhere [Holben *et al.*, 1998, 2006; Eck *et al.*, 1999, 2005; Smirnov *et al.*, 2000]. For all sky radiance wavelengths (i.e., 440, 675, 870, and 1020 nm), the  $\omega_0$  uncertainty is expected to be  $\pm 0.03$  based on Version 1 almucantar retrieval computations when  $\tau_{440\text{nm}} > 0.4$  [Holben *et al.*, 1998; Eck *et al.*, 1999; Dubovik *et al.*, 2000, 2002]. When compared to AERONET  $\omega_0$  retrievals, in situ measurements of  $\omega_0$  were within AERONET uncertainty estimates [Leahy *et al.*, 2007; Johnson *et al.*, 2009; Müller *et al.*, 2010; Toledano *et al.*, 2011].

In-depth discussions of the almucantar retrieval products are given by Dubovik and King [2000] and Dubovik *et al.* [2000, 2002, 2006] and quality criteria are discussed by Holben *et al.* [2006]. Dubovik *et al.* [2002] provided averaged almucantar retrieval aerosol optical and microphysical properties based on aerosol types and source region using AERONET pre-Version 1 data (i.e., data collected and analyzed prior to the release of quality assured Version 1 retrieval data set in 2003). These results have been used throughout the literature to define aerosol type based on the aerosol absorption characteristics [Russell *et al.*, 2010a and references therein]. Notably, the Version 2 retrievals (i.e., released in 2006) utilized new input data sets (e.g., NCEP reanalysis, MODIS ecosystem type-based BRDF functions, and geographically and temporally varying black sky albedo), more dynamic calculations of the surface reflectance than the Version 1 assumption of a green Earth surface reflectance, robust quality checks of the measured sky radiance inputs, and improved criteria for acceptable sky residual fits [Holben *et al.*, 2006; Leahy *et al.*, 2007; Sinyuk *et al.*, 2007; Eck *et al.*, 2008 and references therein]. For example, in the United Arab Emirates and Arabian Gulf, Version

2 improvements provided more consistent  $\omega_o$  magnitudes and spectra for coarse-mode dust aerosol over two vastly different surfaces (i.e., small island versus bright desert) with  $\omega_o$  differences of less than 0.01 compared to 0.03 for the Version 1 spheroid inversion model and with increased absorption at 440 nm, which typically occurs in iron-rich desert dust, rather than spectrally neutral  $\omega_o$  from Version 1 retrievals [Eck *et al.*, 2008].

Additional instrument checks were implemented to assess absorption properties from the Version 2 almucantar retrievals. To improve the quality of the sky radiance measurements used for almucantar retrievals, instrument collimator consistency checks were performed to remove potential artifacts (e.g., induced by spider webs in the tube or contamination on the sensor head window due to moisture or excessive dust) in the radiance measurements. The sky radiance measurements at  $\pm 6^\circ$  azimuth from solar zenith—using the solar aureole and sky gains for instruments with only Silicon detectors—were required to have a percent difference of less than 10% spectrally from 440 to 1020 nm. For Silicon and InGaAs detector instruments (where each detector measures in a different collimator tube), the temperature corrected Silicon and InGaAs  $\tau_{1020\text{ nm}}$  difference ( $\Delta\tau$ ) must be less than  $\Delta\tau_{\text{limit}}$  of  $0.06/m$  (where  $m$  is the optical air mass), which results in a  $\Delta\tau_{\text{limit}}$  of 0.03 when  $m$  equals 2 and 0.06 for the overhead sun ( $m=1$ ). Collimator consistency checks provide an improved method to further quality assure the Level 2.0 almucantar retrieval data set.

### 5.3 Climatology of Aerosol Absorption Properties

Dust particles aggregated with varying combinations of clay, quartz, and hematite exhibit strong absorption in the blue wavelength region (e.g., 440 nm) with lower absorption in the visible and near infrared wavelengths (i.e.,  $\omega_o$  increasing with

wavelength) [Sokolik and Toon 1999]. For fine mode particles ( $r < 1.0 \mu\text{m}$  in the volume size distribution), hygroscopic aerosol particles (e.g., sulfates) have near neutral  $\omega_o$  spectral dependence and high scattering efficiency [Dubovik et al., 2002]. Black carbon (BC) particles have the strongest absorption in the near-infrared ( $\omega_o$  decreasing with  $\lambda$  when the sole absorber), while aerosols composed of brown carbon (BrC) or organic carbon (OC) exhibit stronger absorption in ultraviolet and visible bands ( $\omega_o$  increasing with  $\lambda$  when the sole absorber) [Eck et al., 2009]. Varying concentrations of BC with dust, BrC, and/or OC particles can produce ambiguous  $\omega_o$  wavelength dependence (i.e., increasing, decreasing, or constant with  $\lambda$ ) due to the spectral absorption characteristics of the aerosol mixture; however, the net effect is stronger absorption across the retrieved spectrum (e.g., 440 to 1020 nm) [Dubovik et al., 2002; Giles et al., 2011a].

The AERONET Version 2, Level 2.0 absorption properties at each site are presented in Figure 5.2 and Table 5.2 to provide an update to Dubovik et al. [2002] and Russell et al. [2010a]. The spectral  $\omega_o$  behavior is similar to Dubovik et al. [2002] for most regions. For Solar Village (Dust), Capo Verde (Dust), GSFC (U/I), Mexico City (U/I), and Mongu (BB), the  $\omega_o$  differences between Dubovik et al. [2002] and Table 5.2 (i.e.,  $\omega_o^{\text{Dubovik 2002}} - \omega_o^{\text{Table 5.2}}$ ) showed an overall average decrease of 0.01 for these sites with the largest decrease of 0.02 spectrally for GSFC and Capo Verde and smallest decrease ranging from 0 to 0.01 for Mongu. Notably, the  $\omega_o$  standard deviations are significantly greater by 0.01 to 0.03 in the present study than Dubovik et al. [2002] for all five sites. Table 5.2 differs from Dubovik et al. [2002] due to utilizing different analysis criteria (e.g.,  $\tau_{440\text{nm}} > 0.4$  in Table 5.2 vs.  $\tau_{1020\text{nm}} \geq 0.3$  and  $\alpha_{\text{ext}} \leq 0.6$  for desert dust in Dubovik et al. [2002]), implementing improved surface characterization and inversion

quality checks in Version 2 (as discussed in Section 5.2), and utilizing a larger data set (e.g., the number of  $\omega_0$  retrievals at GSFC is four times larger than *Dubovik et al.* [2002]).

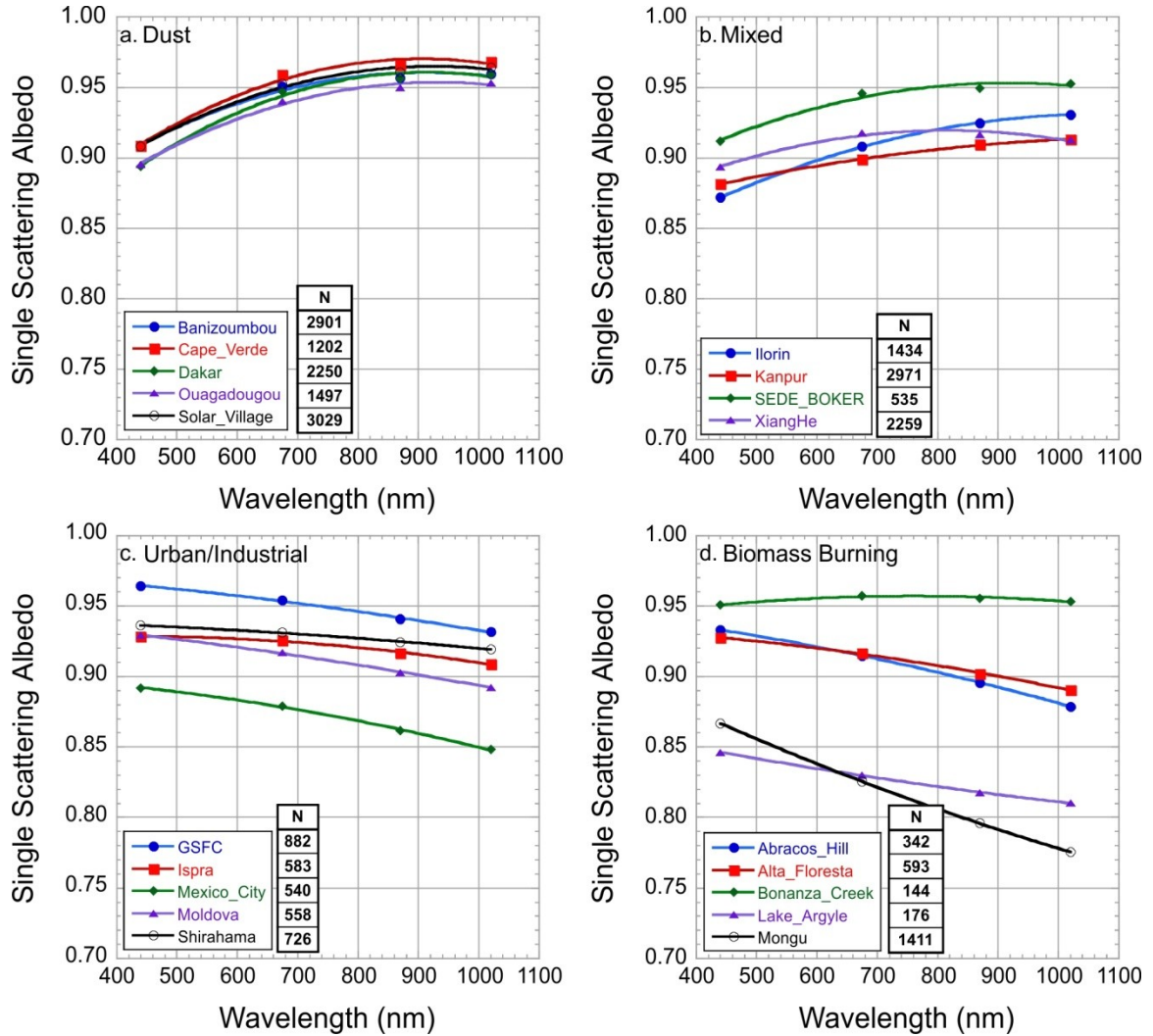


**Figure 5.2 Spectral single scattering albedo averages were grouped by dominant aerosol particle category for  $\tau_{440\text{nm}} > 0.4$  using AERONET Version 2, Level 2.0 data. The plots utilize second order polynomial fit. Figure from *Giles et al.* [2012].**

For  $\omega_{0440\text{nm}}$  as a function of  $\tau_{440\text{nm}}$ , the  $R^2$  values—calculated based on a second order fit—ranged from 0.0 to 0.16 for each site, indicating weak correlation and only up to 16% of  $\omega_{0440\text{nm}}$  variation was explained by  $\tau_{440\text{nm}}$ . Table 5.2 shows that the Dust category has the least variability among sites likely due to the similar mineralogy, while the BB category has the largest variability likely due to various fuel types and fuel

combustion phases resulting from different relative BC emissions [Eck *et al.*, 2003b].

The Mixed category ( $0.33 < \eta_{550\text{nm}} \leq 0.66$ )  $\omega_o$  average shows strong spectral absorption and dust-like  $\omega_o$  spectra with stronger absorption at 440 nm due to significant dust contribution to the optical mixture. Sokolik and Toon [1998] showed that varying hematite amounts in dust can lead to increased absorption spectrally from the blue to near-infrared wavelength region. Using  $\alpha_{\text{ext}} < 0.2$  to designate “pure dust” as suggested by Kim *et al.* [2011], the overall “pure dust” average of  $\omega_o$  for all Dust category sites is 0.91, 0.97, 0.97, 0.97 for the 440, 675, 870, and 1020 nm wavelengths, respectively. These “pure dust”  $\omega_o$  values are lower by up to 0.02, spectrally, than those reported by Dubovik *et al.* [2002] for Dust sites and are lower by up to 0.01 for  $\omega_o$  at 550 nm (logarithmically interpolated between 440 nm and 675 nm) compared to similar sites analyzed by Kim *et al.* [2011]. Table 5.2 shows the Dust site  $\omega_o$  averages are lower than “pure dust,” indicating possible incursions by other aerosols (e.g., biomass burning smoke). An analysis of  $\omega_o$  averages using month designations from Catrall *et al.* [2005] for six corresponding sites (i.e., GSFC, Mexico City, Alta Floresta, Mongu, Capo Verde, and Solar Village) reveals negligible changes with respect to  $\omega_o$  values in Table 5.2, except for Capo Verde, which has slightly higher  $\omega_o$  averages (i.e.,  $\sim 0.005$ ) and lower  $\omega_o$  standard deviations (i.e.,  $-0.01$ ). For Capo Verde, the differences between  $\omega_o$  averages for “pure dust” and  $\omega_o$  averages computed from May to October (as suggested by Catrall *et al.* [2005]) are negligible, indicating mainly dust occurs during this period and possibly episodic biomass burning smoke events affect the site during other months [Tanre *et al.*, 2003; Toledano *et al.*, 2011]. Eck *et al.* [2010] and Giles *et al.* [2011a] also showed increasing absorption with wavelength for decreasing  $\alpha_{\text{abs}}$ , indicating an optical mixture

and possibly aggregation of dust and carbonaceous particles at Kanpur, India.  $\eta$  is interpolated to 550 nm using the linear fit of the logarithms of  $\tau_f$ ,  $\tau$  (i.e.,  $\tau_f + \tau_c$ ) and the 440, 675, and 870 nm wavelengths similar to *Lee et al.* [2010]. In Figure 5.3a, the Mixed category for the coarse mode particles ( $\eta_{550\text{nm}}$ : 0.0-0.33) resembles dust  $\omega_o$  spectra as shown in Figure 5.2a. In Figure 5.3c, for fine mode particles ( $\eta_{550\text{nm}}$ : 0.66-1.0), the  $\omega_o$  magnitudes and variability are similar to U/I or BB particle types categories but with less  $\omega_o$  spectral dependence possibly due to varying amounts of BC, BrC, and OC [*Derimian et al.*, 2006; *Eck et al.*, 2009, 2010]. The average  $\omega_o$  for  $\alpha_{\text{abs}}$  binned between 1.5 and 2.0 shown by *Giles et al.* [2011a] at Kanpur closely resembles the absorption magnitude and spectral shape of mixed aerosol types for the Mixed category ( $0.33 < \eta_{550\text{nm}} \leq 0.66$ ) in Table 5.2 as well as Figure 5.2b and Figure 5.3b suggesting various mixtures of aerosol particles contributing to the absorption.

**Table 5.2 Average aerosol absorption and size properties by aerosol type category from AERONET Version 2 almucantar retrievals. <sup>a</sup>. Table from *Giles et al.* [2012].**

Site	Date Range	$\omega_o$ 440/675/870/1020 nm	$\alpha_{\text{abs}440-870\text{nm}}$	$\alpha_{\text{ext}440-870\text{nm}}$	$\eta_{550\text{nm}}$	N
<i>Dust</i>						
Banizoumbou	1999-2010	0.91/0.95/0.96/0.96 0.04/0.04/0.04/0.04	1.7±0.6	0.3±0.2	0.28±0.20	2901
Capo_Verde	1999-2010	0.91/0.96/0.97/0.97 0.03/0.03/0.03/0.03	2.0±0.6	0.2±0.2	0.24±0.16	1202
Dakar	2000-2010	0.89/0.95/0.96/0.96 0.03/0.04/0.04/0.03	1.9±0.6	0.3±0.2	0.28±0.23	2250
Ouagadougou	1999-2007	0.90/0.94/0.95/0.95 0.04/0.04/0.04/0.03	1.6±0.5	0.3±0.2	0.30±0.21	1497
Solar_Village	1999-2010	0.91/0.95/0.96/0.96 0.02/0.02/0.02/0.02	1.8±0.6	0.3±0.3	0.28±0.25	3029
<i>Mixed (for <math>0.33 &lt; \eta_{550\text{nm}} \leq 0.66</math>)</i>						
Ilorin	1999-2009	0.86/0.90/0.92/0.92 0.05/0.05/0.04/0.04	1.6±0.4	0.7±0.2	0.47±0.23	798
Kanpur	2001-2010	0.87/0.90/0.92/0.93 0.03/0.03/0.03/0.03	1.4±0.4	0.7±0.2	0.48±0.22	963
SEDE_BOKER	1999-2010	0.91/0.93/0.93/0.94 0.02/0.02/0.03/0.03	1.2±0.5	0.7±0.2	0.48±0.20	170
XiangHe	2001, 2004-2010	0.88/0.92/0.93/0.93 0.03/0.03/0.03/0.03	1.8±0.4	0.8±0.2	0.53±0.22	446

<sup>a</sup> Aerosol optical depth (AOD) at 440 nm is greater than 0.4 for Version 2, Level 2.0 almucantar retrievals. The spectral single scattering albedo ( $\omega_o$ ) averages are listed first followed by their standard deviations. The absorption and extinction Ångström exponents ( $\alpha_{\text{abs}}$  and  $\alpha_{\text{ext}}$ ) and are computed using the 440-675-870 nm wavelength interval. The fine mode fraction of the AOD ( $\eta_{550\text{nm}}$ ) is interpolated to 550 nm.

**Table 5.2 (continued)**

Site	Date Range	$\omega_o$ 440/675/870/1020 nm	$\alpha_{\text{abs440-870nm}}$	$\alpha_{\text{ext440-870nm}}$	$\eta_{550\text{nm}}$	N
<i>Urban/Industrial</i>						
GSFC	1999–2010	0.96/0.95/0.94/0.93 0.02/0.02/0.03/0.03	1.1±0.2	1.8±0.2	0.94±0.20	882
Ispira	1999-2010	0.93/0.93/0.92/0.91 0.03/0.04/0.04/0.04	1.4±0.4	1.6±0.2	0.92±0.24	583
Mexico_City	1999-2010	0.89/0.88/0.86/0.85 0.04/0.04/0.05/0.06	1.3±0.3	1.6±0.2	0.87±0.18	540
Moldova	1999-2010	0.93/0.92/0.90/0.89 0.03/0.04/0.05/0.05	1.2±0.3	1.6±0.3	0.87±0.28	558
Shirahama	2000-2010	0.94/0.93/0.92/0.92 0.03/0.03/0.04/0.05	1.1±0.5	1.3±0.3	0.81±0.35	726
<i>Biomass Burning</i>						
Abracos_Hill	1999-2005	0.93/0.91/0.90/0.88 0.02/0.03/0.04/0.05	1.3±0.4	2.0±0.1	0.95±0.14	342
Alta_Floresta	1999-2010	0.93/0.92/0.90/0.89 0.02/0.03/0.04/0.05	1.5±0.4	1.9±0.2	0.92±0.18	593
Bonanaza Creek	1999-2005, 2008- 2010	0.95/0.96/0.96/0.95 0.03/0.03/0.04/0.04	1.8±0.5	1.5±0.2	0.96±0.22	144
Lake_Argyle	2002-2006, 2009-2010	0.85/0.83/0.82/0.81 0.04/0.05/0.06/0.07	1.4±0.3	1.5±0.4	0.79±0.36	176
Mongu	1999-2007, 2009	0.87/0.83/0.80/0.77 0.03/0.04/0.04/0.05	1.2±0.2	1.9±0.1	0.92±0.10	1411

The  $\omega_o$  and  $\tau_{\text{ext}}$  are used to derive the  $\tau_{\text{abs}}$  from AERONET data.  $\tau_{\text{abs}}$  and  $\alpha_{\text{abs}}$  were averaged for each site based on dominant particle type category in Figure 5.4 and Table 5.2. For the five sites (i.e., GSFC, Mexico City, Mongu, Capo Verde, and Solar Village), a comparison of average  $\alpha_{\text{abs}}$  values in Table 5.2 with *Russell et al.* [2010a] for the 440-870 nm range shows the largest difference in  $\alpha_{\text{abs}}$  (i.e.,  $\alpha_{\text{abs Russell 2010a}} - \alpha_{\text{abs Table 5.2}}$ ) at GSFC (-0.25) and Capo Verde (+1.2). For the other three sites, the  $\alpha_{\text{abs}}$  averages in Figure 5.4 are comparable to those reported by *Russell et al.* [2010a] and *Giles et al.* [2011a]. In Figure 5.5, the Mixed category was further stratified by the  $\eta_{550\text{nm}}$  as in Figure 5.3. The coarse particle range ( $\eta_{550\text{nm}}$ : 0.0-0.33) shows similar  $\alpha_{\text{abs}}$  (1.7-2.3) as the Dust category (which is expected for dust dominated cases) and the fine particle range ( $\eta_{550\text{nm}}$ : 0.66-1.0) shows an  $\alpha_{\text{abs}}$  (0.8-1.5) similar to BB and U/I categories. The mixed size particle range ( $\eta_{550\text{nm}}$ : 0.33-0.66) is nearly identical to the Mixed category  $\alpha_{\text{abs}}$  (1.2-1.7) in Figure 5.4b and similar to values reported by *Eck et al.* [2010]. As shown by *Bergstrom et al.* [2007] and *Russell et al.* [2010a], the  $\alpha_{\text{abs}}$  may vary significantly when considering the aerosol particle size between fine and coarse modes; however, when considering U/I and BB aerosols within the fine particle range, significant overlap results in  $\alpha_{\text{abs}}$ . The sensitivity of  $\alpha_{\text{abs}}$  with respect to input parameters will be investigated in the next section.

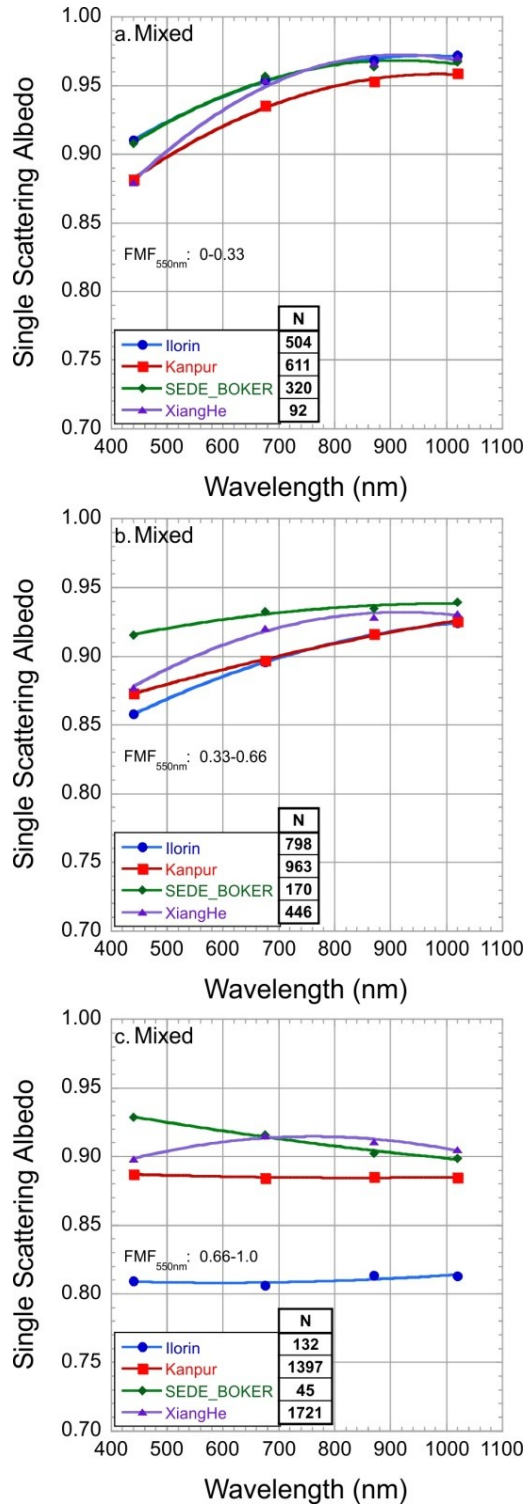


**Figure 5.3** Similar to Figure 5.2, except the spectral single scattering albedo averages for the Mixed category were grouped by fine mode fraction of AOD ( $\eta_{550\text{nm}}$ ) using the ranges 0.0-0.33 for coarse mode dominated particles (a), 0.33-0.66 for mixed size particles (b), and 0.66-1.0 for fine mode dominated particles (c). Figure from *Giles et al.* [2012].

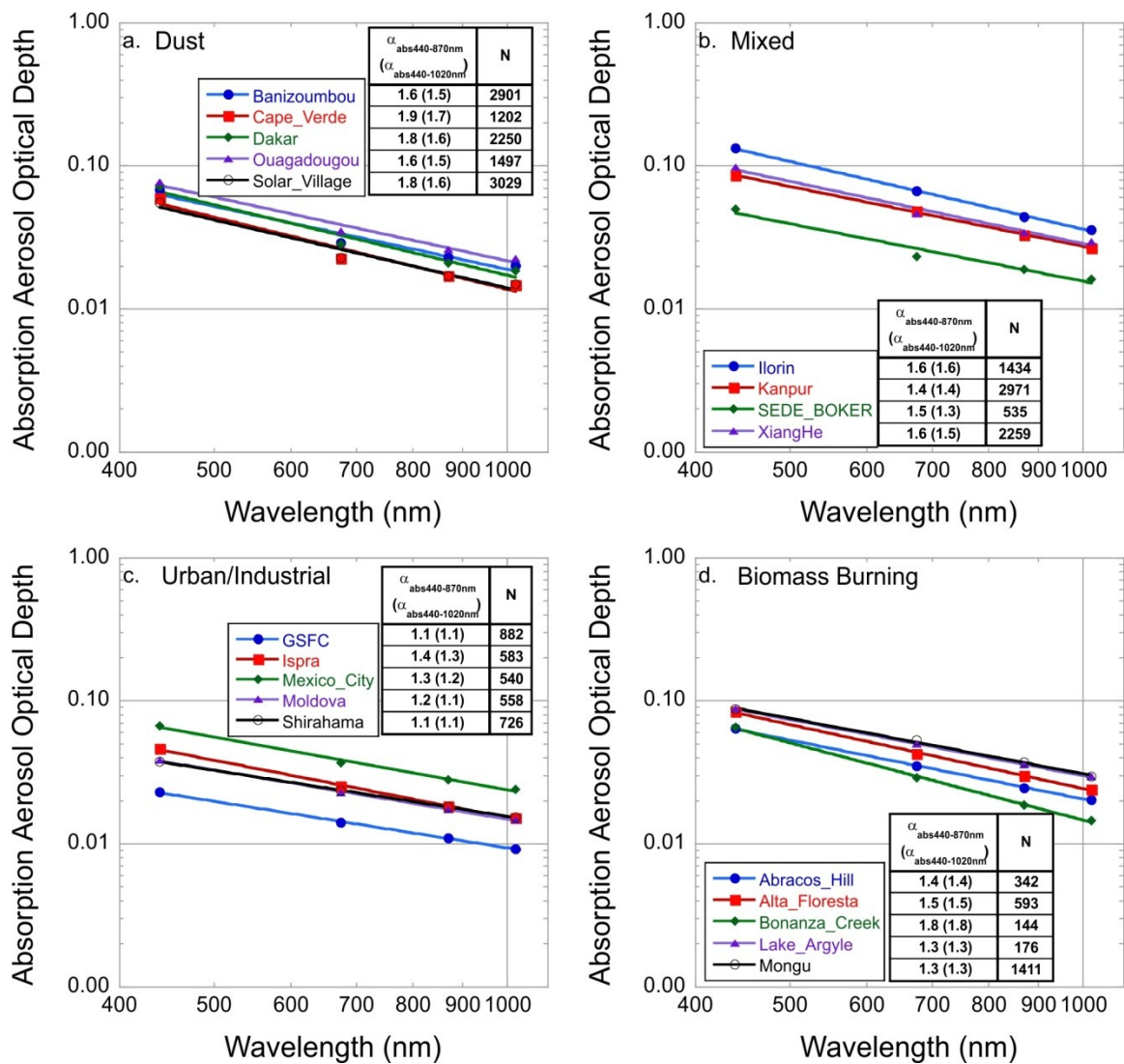


**Figure 5.4** Absorption aerosol optical depth ( $\tau_{\text{abs}}$ ) and absorption Ångström exponent ( $\alpha_{\text{abs}}$ ) averages were grouped by dominant aerosol particle category for  $\tau_{440\text{nm}} > 0.4$  using AERONET Version 2, Level 2.0 data. The plots use the power law fit and slopes of these lines are the  $\alpha_{\text{abs}}$  (440-870 nm or 440-1020 nm) listed adjacent to the legend in each plot. Figure from *Giles et al.* [2012].

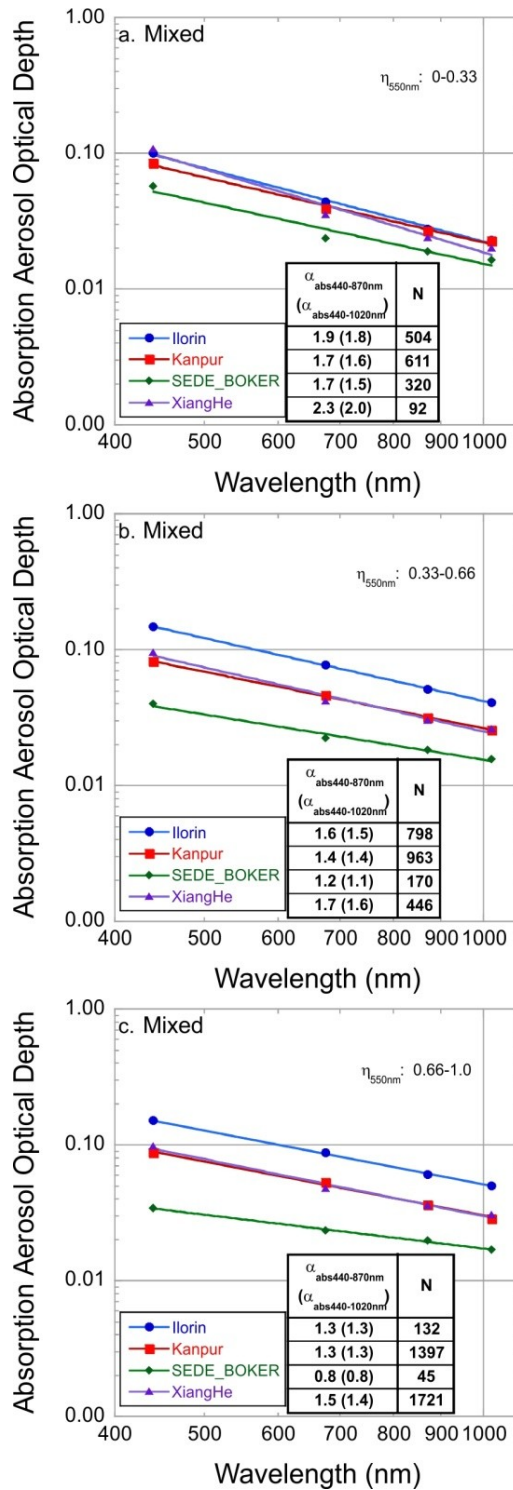


**Figure 5.5** Similar to Figure 5.3, except  $\tau_{abs}$  and  $\alpha_{abs}$  averages for the Mixed category were grouped by fine mode fraction of the AOD ( $\eta_{550nm}$ ) using ranges of 0.0-0.33 for coarse mode dominated particles (a), 0.33-0.66 for mixed size particles (b), and 0.66-1.0 for fine mode particles (c). Figure from *Giles et al.* [2012].

#### 5.4 Sensitivity of Absorption Ångstrom Exponent to Single Scattering Albedo

The retrieved values of  $\alpha_{\text{abs}}$  have a normal distribution (Figure 5.6) when calculating  $\alpha_{\text{abs}}$  using three wavelengths (440-675-870 nm) for each dominant aerosol type. *Russell et al.* [2010a] showed that the average  $\alpha_{\text{abs}}$  values generally decreased with increasing spectral range possibly due in part to the crude surface reflectance assumption made in early AERONET analysis (as discussed in Section 5.2), while *Gyawali et al.* [2012] showed an increasing  $\alpha_{\text{abs}}$  values with increasing spectral range for clean and polluted days during winter in Reno, Nevada. However, increasing or decreasing trends of  $\alpha_{\text{abs}}$  depend on the wavelength interval [*Lack and Cappra* 2010]. Using 19 AERONET sites partitioned by aerosol type,  $\alpha_{\text{abs}}$  values computed from 440-675-870 nm wavelength range have large variability with standard deviations ranging from  $\pm 0.3$  to  $\pm 0.6$  ( $1.76 \pm 0.58$  for Dust;  $1.53 \pm 0.44$  for Mixed;  $1.21 \pm 0.37$  for U/I;  $1.35 \pm 0.35$  for BB). Individual  $\alpha_{\text{abs}}$  retrieval calculations [ $\alpha_{\text{abs}}$  (Dust):  $\sim 0-4$ ;  $\alpha_{\text{abs}}$  (Mixed):  $\sim 0-3.5$ ;  $\alpha_{\text{abs}}$  (U/I):  $\sim 0-2$ ;  $\alpha_{\text{abs}}$  (BB):  $\sim 0-2.5$ ] are within the range of all dominant particle types; therefore,  $\alpha_{\text{abs}}$  should not be used alone to determine aerosol types without the use of other information (e.g., aerosol size). Further, Figure 5.6 shows a significant number of  $\alpha_{\text{abs}}$  below 1.0, which is the black carbon limit for very small particles [*Bergstrom et al.*, 2002]. However, *Lack and Cappra* [2010] suggested  $\alpha_{\text{abs}}$  (from 380-750 nm) values for larger optically effective BC particles may exist between  $\sim -0.2$  and 1.6 depending on the BC coating material. Nonetheless, the U/I category has over 22% of the  $\alpha_{\text{abs}}$  retrievals below 1.0, while the other categories have  $\sim 10\%$  of the  $\alpha_{\text{abs}}$  data below 1.0 also possibly due to the uncertainty of the retrieved  $\omega_0$ .

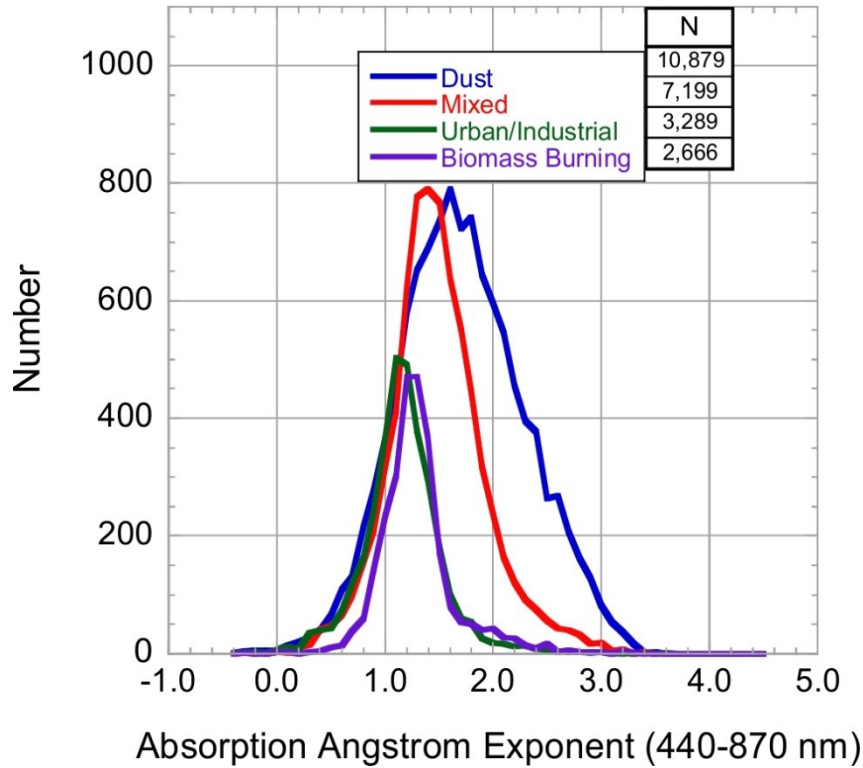


**Figure 5.6 Absorption Ångström exponent ( $\alpha_{\text{abs}}$ ) frequency distribution for individual retrievals partitioned by dominant aerosol particle using AERONET Version 2, Level 2.0 data. Approximately 10% of the  $\alpha_{\text{abs}}$  retrievals (22% for Urban/Industrial) were below 1.0 or  $\lambda^{-1}$  dependence. Figure from *Giles et al.* [2012].**

A sensitivity study of  $\alpha_{\text{abs}}$  was performed to test the response of  $\alpha_{\text{abs}}$  in equation (3) by varying  $\omega_0$  for each wavelength (i.e., 440, 675, and 870 nm) and holding  $\tau_{\text{ext}}$  constant in equation (2). While the spectral  $\omega_0$  depends on the accuracy of the spectral AOD measurements, the source of error is already included in the estimated  $\omega_0$  uncertainties. Therefore, a sensitivity study can be performed by fixing AOD and varying  $\omega_0$ , since: (1) the uncertainties in AOD are much smaller in magnitude than the values of AOD used in this study (i.e.,  $\tau_{440\text{nm}} > 0.4$ ) and (2) the uncertainties in  $\omega_0$ —estimated to be  $\pm 0.03$ —account for different sources of error including AOD [*Dubovik et al.*, 2000, 2002]. In this study,  $\omega_0$  was varied by  $\pm 0.01$ ,  $\pm 0.02$ ,  $\pm 0.03$ , and  $\pm 0.04$  to show the variability of  $\alpha_{\text{abs}}$  with various degrees of  $\omega_0$  uncertainty. Different spectral  $\omega_0$  inputs

schemes were implemented to determine the  $\alpha_{\text{abs}}$  response by varying  $\omega_0$  equally across all wavelengths, by perturbing  $\omega_0$  at only one end point in the 440-675-870 nm wavelength set (i.e., 440 nm or 870 nm), and by perturbing  $\omega_0$  at 440 nm or 870 nm in the 440-870 nm wavelength pair (i.e., excluding 675 nm). Positive  $\omega_0$  perturbation may approach values of 1.0 (i.e., absolute scattering) and can produce large positive or negative  $\alpha_{\text{abs}}$  due to very low  $\tau_{\text{abs}}$ . To prevent such cases, the  $\omega_0$  magnitude was limited to less than 0.995 for positive  $\omega_0$  perturbations for all wavelengths resulting in a reduced data subset.

Table 5.3 shows the sensitivity of  $\alpha_{\text{abs}}$  to perturbations in  $\omega_0$ . The perturbation of  $\pm 0.03 \omega_0$  (i.e., the current AERONET estimated uncertainty) changed  $\alpha_{\text{abs}}$  by at least  $\sim \pm 0.6$  for Dust,  $\sim \pm 0.2$  for Mixed, and  $\sim \pm 0.1$  for U/I and BB. The perturbations of  $\omega_0$  by  $\pm 0.02$  showed  $\sim 0.1$  smaller corresponding change in  $\alpha_{\text{abs}}$  with respect to  $\pm 0.03 \omega_0$  perturbations for Dust and less than 0.05-0.10 for the other categories. Perturbations of  $\omega_0$  by  $\pm 0.04$  showed large deviations from the unperturbed data set, indicating much greater uncertainty for  $\alpha_{\text{abs}}$  with increasing  $\omega_0$  uncertainty. The simulated overestimation of spectral  $\omega_0$  for U/I and BB (i.e.,  $\delta\omega_0 = -0.03$ ) showed a higher  $\delta\alpha_{\text{abs}}$  suggesting a possibility that the unperturbed  $\alpha_{\text{abs}}$  is underestimated and may possibly, at least partly, explain  $\alpha_{\text{abs}}$  below 1.0 in these categories. However, *Lack and Cappa* [2010] determined that the large  $\alpha_{\text{abs}}$  variation ( $-0.2$  and  $1.3$  for the 380-750 nm wavelength range) for BC particles with coatings are possible and  $\alpha_{\text{abs}}$  values less than 1.0 may occur with larger BC particles (e.g.,  $r_{\text{core}} > 0.1 \mu\text{m}$  and  $r_{\text{shell}} > 0.25 \mu\text{m}$ ). *Gyawali et al.* [2012] showed laboratory measurements of kerosene soot particles have  $\alpha_{\text{abs}}$  values of  $\sim 0.8$  for the

**Table 5.3 Sensitivity of the absorption Ångström exponent ( $\alpha_{\text{abs}}$ ) to perturbations of single scattering albedo ( $\omega_0$ ) for each dominant aerosol particle type. Table from *Giles et al. [2012]*.**

Type	$\lambda$ (nm)	$\alpha_{\text{abs}}$ <sup>a</sup>		$\delta\alpha_{\text{abs}}$ <sup>b</sup>			N
		$\delta\omega_0=0.0$	$\delta\omega_0$	All $\tau(\lambda)$	$\tau_{440\text{nm}}$	$\tau_{870\text{nm}}$	
Dust	440-675-870	1.76±0.58	-0.01	-0.27			10879
		1.67±0.52	+0.01 <sup>c</sup>	+0.40			9807
		1.76±0.58	-0.02	-0.45			10879
		1.49±0.42	+0.02 <sup>c</sup>	+0.67			7290
		1.76±0.58	-0.03 <sup>d</sup>	-0.57	+0.47	-0.90	10879
		1.33±0.38	+0.03 <sup>cd</sup>	+0.79	-0.54	+1.16	4898
		1.76±0.58	-0.04	-0.67			10879
		1.23±0.36	+0.04 <sup>c</sup>	+0.85			3342
Mixed	440-675-870	1.53±0.44	-0.01	-0.09			7199
		1.52±0.42	+0.01 <sup>c</sup>	+0.13			7051
		1.53±0.44	-0.02	-0.16			7199
		1.47±0.38	+0.02 <sup>c</sup>	+0.23			6623
		1.53±0.44	-0.03 <sup>d</sup>	-0.21	+0.40	-0.53	7199
		1.43±0.35	+0.03 <sup>cd</sup>	+0.30	-0.51	+0.71	6060
		1.53±0.44	-0.04	-0.25			7199
		1.40±0.33	+0.04 <sup>c</sup>	+0.35			5479
Urban/ Industrial	440-675-870	1.21±0.37	-0.01	+0.05			3289
		1.20±0.36	+0.01 <sup>c</sup>	-0.10			3174
		1.21±0.37	-0.02	+0.09			3289
		1.19±0.35	+0.02 <sup>c</sup>	-0.21			2874
		1.21±0.37	-0.03 <sup>d</sup>	+0.12	+0.74	-0.52	3289
		1.18±0.34	+0.03 <sup>cd</sup>	-0.31	-1.02	+0.58	2428
		1.21±0.37	-0.04	+0.14			3289
		1.18±0.34	+0.04 <sup>c</sup>	-0.40			2027
Biomass Burning	440-675-870	1.35±0.35	-0.01	+0.03			2666
		1.34±0.34	+0.01 <sup>c</sup>	-0.04			2639
		1.35±0.35	-0.02	+0.06			2666
		1.33±0.32	+0.02 <sup>c</sup>	-0.10			2598
		1.35±0.35	-0.03 <sup>d</sup>	+0.08	+0.45	-0.31	2666
		1.32±0.31	+0.03 <sup>cd</sup>	-0.19	-0.62	+0.35	2512
		1.35±0.35	-0.04	+0.11			2666
		1.31±0.29	+0.04 <sup>c</sup>	-0.29			2421

<sup>a</sup> indicates the unperturbed  $\alpha_{\text{abs}}$  average is recalculated based on available  $\omega_0$ .

<sup>b</sup> indicates wavelength(s) used in perturbation of  $\omega_0$ .

<sup>c</sup> indicates positive perturbation of  $\omega_0$  must be less than 0.995 for any wavelength.

<sup>d</sup> indicates these criteria are the current uncertainty estimates based on *Dubovik et al. [2000]*.

355-1020 nm range and in situ measurement values of  $\alpha_{\text{abs}}$  measured during the Reno, Nevada, winter period varied for clean days ( $\text{PM}_{2.5} < 40 \mu\text{g}/\text{m}^3$ ) between  $\sim 1.0$  and  $1.4$  and for polluted days ( $\text{PM}_{2.5} \geq 40 \mu\text{g}/\text{m}^3$ ) between  $0.9$  and  $1.2$  for the  $405\text{-}870$  nm wavelength range. Although these model simulations and laboratory and in situ measurements suggest  $\alpha_{\text{abs}}$  values may occur below  $1.0$ , AERONET remotely sensed values of  $\alpha_{\text{abs}}$  have not yet been compared to coincident column-effective in situ measurements (e.g., measured by aircraft) but this analysis will be addressed in future work. In the present analysis, the simulated underestimation of spectral  $\omega_0$  (i.e.,  $\delta\omega_0 = +0.03$ ) for Dust and Mixed indicates possible underestimation of the unperturbed  $\alpha_{\text{abs}}$ , which could also result in  $\alpha_{\text{abs}}$  below  $1.0$ . Table 5.3 also shows that the  $\alpha_{\text{abs}}$  values for the Dust and Mixed categories change in the same direction as the  $\omega_0$  perturbation possibly due to weak spectral dependence of  $\tau_{\text{ext}}$ , while  $\alpha_{\text{abs}}$  values for the U/I and BB categories have the opposite response possibly due to stronger spectral dependence of  $\tau_{\text{ext}}$ . Two additional tests were conducted by perturbing  $\omega_0$  using the wavelength pair ( $440\text{-}870$  nm) and only varying the end points of the  $440\text{-}675\text{-}870$  nm set and the differences between unperturbed  $\alpha_{\text{abs}}$  averages were minimal (not shown). However, perturbing one  $\omega_0$  end point for either the  $440\text{-}870$  nm wavelength pair (not shown) or the  $440\text{-}675\text{-}870$  nm set (Table 5.3) produced very large deviations in  $\alpha_{\text{abs}}$  by up to  $\sim 1.2$  for Dust,  $\sim 0.7$  for Mixed,  $\sim 1.0$  for U/I, and  $\sim 0.6$  for BB. The perturbation of end points simulates atypical behavior of the instrument while deployed in the field (e.g., anomalous filter degradation) showing potential issues in using real-time data products unless further screening is implemented, such as the instrument collimator consistency checks (stated in Section 5.2), which may be utilized to help remove  $\omega_0$  artifacts (i.e., collimator or sensor head window

obstructions) and improve the reliability of  $\alpha_{\text{abs}}$  retrievals. These sensitivity tests quantified the effect of the reduction of  $\omega_0$  uncertainty on improving estimates of  $\alpha_{\text{abs}}$ .

### 5.5 Cluster Analysis of Absorption and Size Properties

Knowledge of aerosol particle spectral absorption provides insight to determine aerosol particle dominance of dust, carbonaceous matter, or hygroscopic aerosols (e.g., sulfates, nitrates, or sea salt). While the co-albedo (or  $1-\omega_0$ ) indicates the magnitude of absorption and  $\alpha_{\text{abs}}$  provides some indication of the dominance of carbonaceous particles (e.g., BC, BrC, and OC) or iron oxides in dust, these parameters alone cannot fully describe the aerosol particle type. Recent studies have suggested applying an aerosol particle size parameter (e.g.,  $\alpha_{\text{ext}}$  or  $\eta$ ) to separate larger dust particles from other aerosol types and mixtures [Lee *et al.*, 2010; Russell *et al.*, 2010a; Giles *et al.*, 2010, 2011a, 2011b]. Expanding upon concepts presented in Chapter 4, several years of AERONET retrievals of  $\omega_{0440\text{nm}}$ ,  $\alpha_{\text{abs}440-870\text{nm}}$ ,  $\alpha_{\text{ext}440-870\text{nm}}$ , and  $\eta_{550\text{nm}}$  (with wavelength subscripts removed hereafter) were analyzed for each dominant aerosol type category using a density based clustering utilizing the Voronoi tessellation [Voronoi 1908; Ishimoto *et al.*, 2010] to determine the relative concentration of points (density =  $1/\text{polygon area}$ ) for each absorption and size relationship. In these density plots (e.g., Figures 5.7-5.10), the high density represents the primary mode for the dominant aerosol particle type category. Various clustering techniques were attempted previously to categorize dominant aerosol particle type at AERONET sites [Catrall *et al.*, 2005; Omar *et al.*, 2005; Levy *et al.*, 2007a; Qin and Mitchell 2009; Russell *et al.*, 2010a, 2010b; Boselli *et al.*, 2012]. For each absorption and size relationship and aerosol type category in this study (Figure 5.11), dominant aerosol particle clusters were computed using averages weighted by

density magnitudes normalized to a 64-level scale (corresponding to a 64-bit color scale). Although weighting reduces the bias introduced by outliers affecting the normal average, additional thresholds were applied to the aerosol size parameters. To further define weighted cluster averages, the  $\alpha_{\text{ext}}$  cluster averages utilized a 0.8 threshold, where  $>0.8$  indicates mainly small sub-micron radius particles and  $\leq 0.8$  is mainly large super-micron radius particles (where  $\alpha_{\text{ext}440-870\text{nm}}=0.8$  is approximately equivalent to  $\eta_{500\text{nm}}=0.5$  as shown for example by *Eck et al.* [2005, 2010]). In addition, the  $\eta$  cluster averages were defined using thresholds of 0.0 to  $\leq 0.33$  (for coarse mode dominated particles), 0.33 to  $\leq 0.66$  (for mixed size), and  $>0.66$  (for fine mode dominated particles). For the BB category (Figure 5.11c and Figure 5.11d), cluster separation was imposed to calculate two additional clusters using a  $\omega_{0440\text{nm}}$  threshold of 0.90 based on the density cluster analyses shown in Figure 5.9 and Figure 5.10.

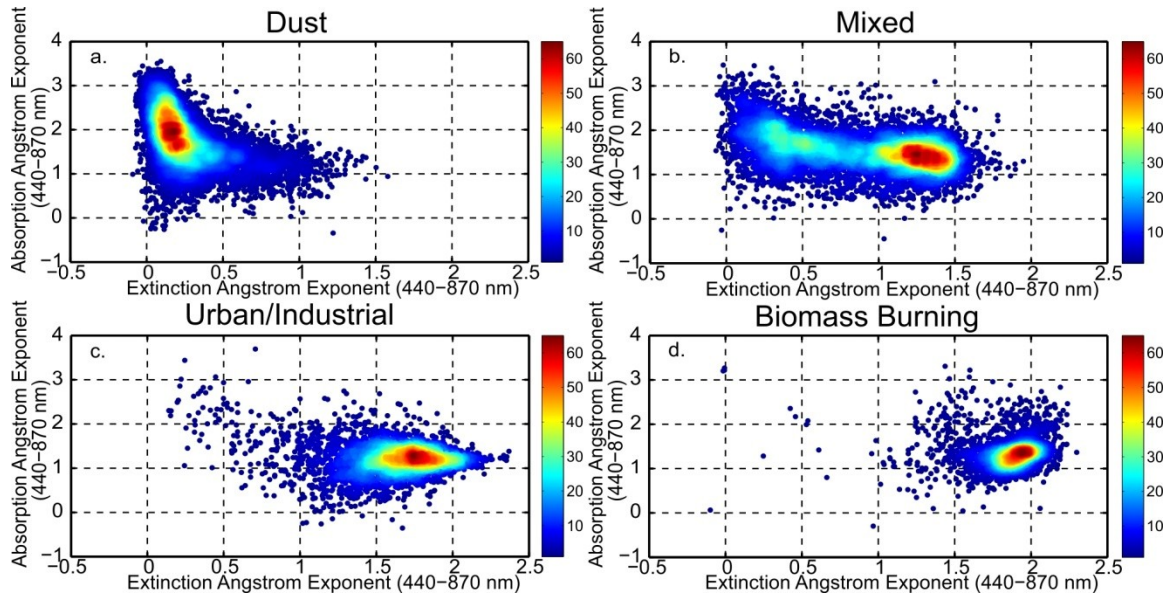


**Figure 5.7** Relative number density plots for the absorption Ångström exponent (440-870 nm) and extinction Ångström exponent (440-870 nm) relationship based on dominant aerosol type using AERONET Version 2, Level 2.0 data. Based on the Voronoi tessellation, the color scale represents the relative density of points in each aerosol type partitioned data set, where orange to red colors (levels ~45-64) indicate the highest number density. Figure from *Giles et al.* [2012].

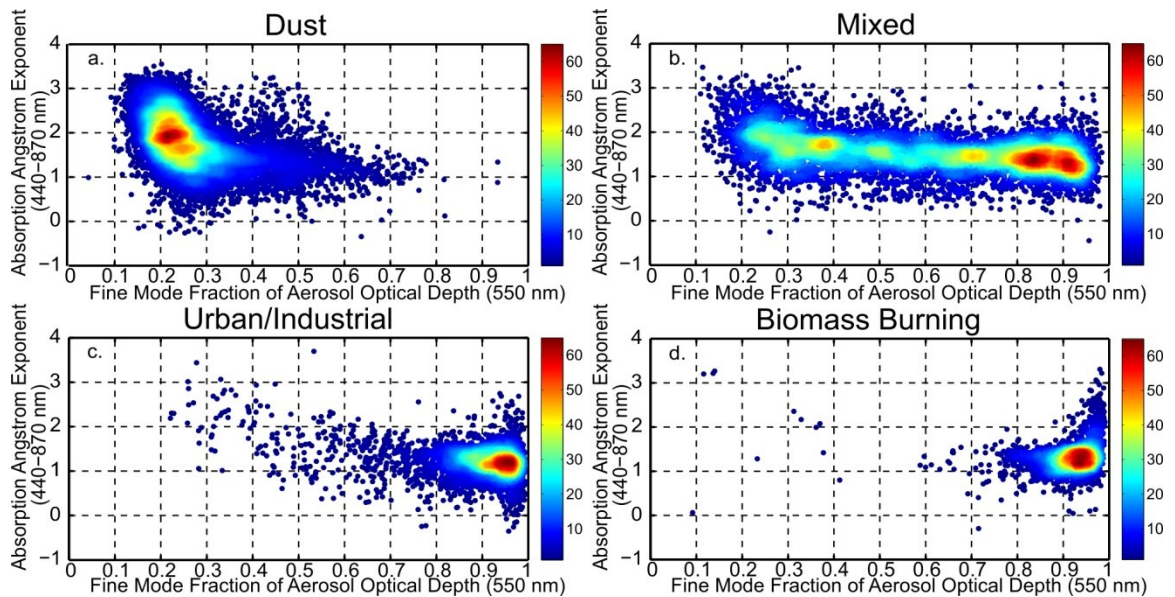


**Figure 5.8** Similar to Figure 5.7, except for the absorption Ångström exponent (440-870 nm) and fine mode fraction of the aerosol optical depth (550 nm) relationship. Figure from *Giles et al.* [2012].

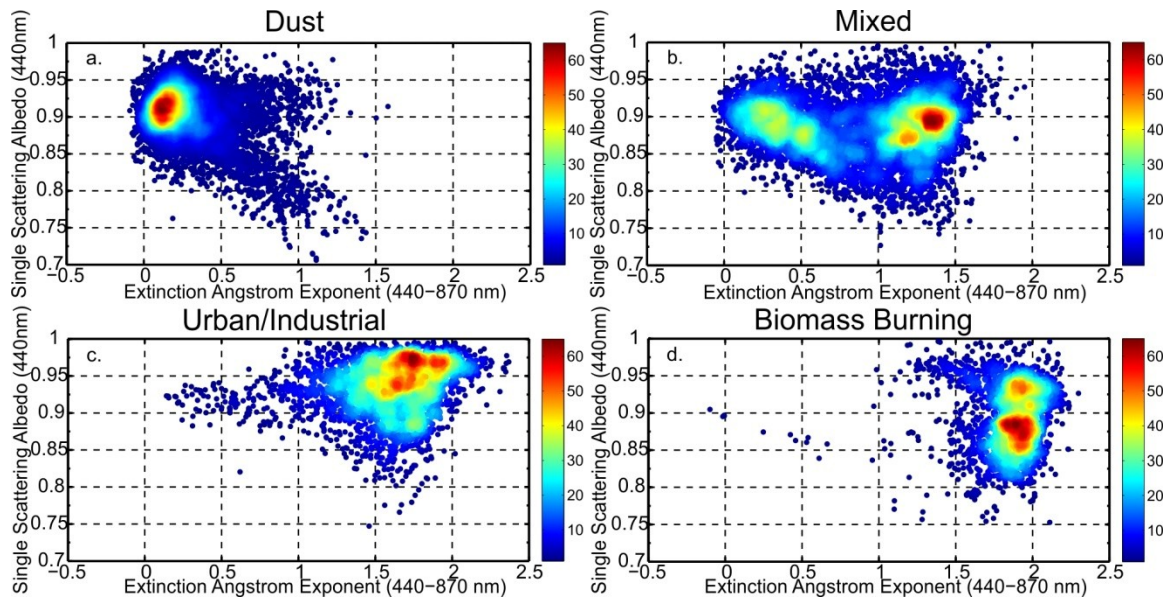


**Figure 5.9** Similar to Figure 5.7, except for the single scattering albedo (440 nm) and the extinction Ångström exponent (440-870 nm) relationship. Figure from *Giles et al.* [2012].

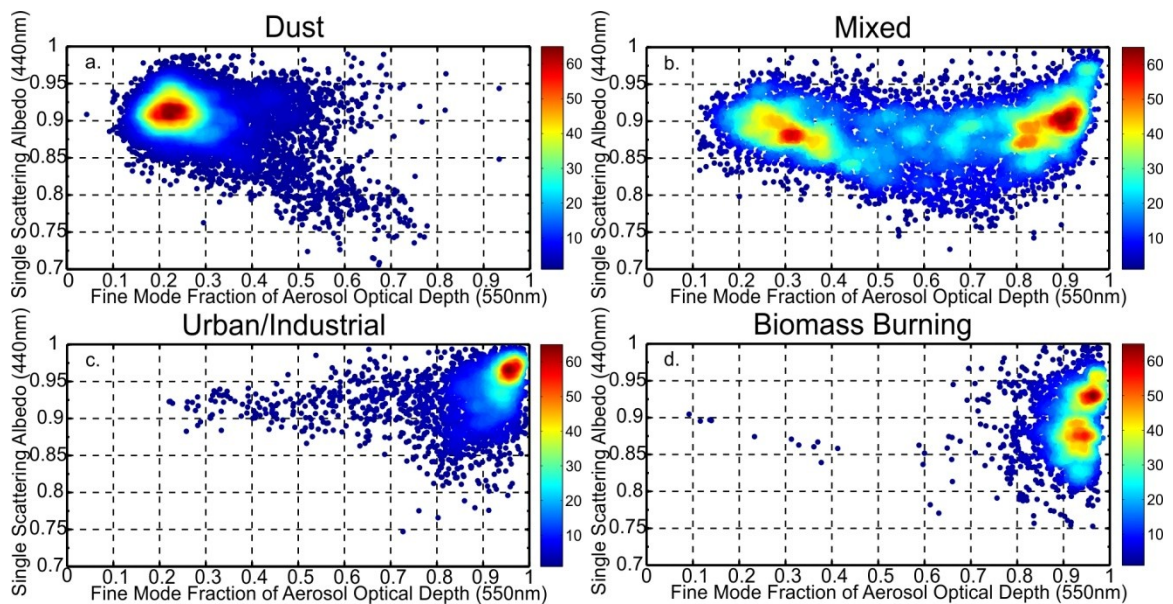


**Figure 5.10** Similar to Figure 5.7, except for the single scattering albedo (440 nm) and fine mode fraction of the aerosol optical depth (550 nm) relationship. Figure from *Giles et al.* [2012].

The relationships of aerosol absorption (i.e.,  $\omega_o$  and  $\alpha_{abs}$ ) and size (i.e.,  $\alpha_{ext}$  and  $\eta$ ) are analyzed with respect to the dominant aerosol type category. For Figures 5.7-5.10, the primary density clusters are clear (denoted by orange and red regions representing relative value levels of  $\sim 45$  to  $64$ ). For example, the Dust category shows a cluster in the region with  $\alpha_{ext}$  of  $\sim 0.2$ - $0.3$  and  $\eta$  of  $\sim 0.2$ - $0.3$ , indicative of domination by coarse mode particles. To provide a better assessment of the clusters, the weighted cluster average and its standard deviation were calculated for each parameter shown in Figure 5.11. In Figure 5.11a and Figure 5.11b, the primary Dust clusters show variation of the  $\alpha_{abs}$  mainly between  $1.5$  and  $2.3$ , which are slightly lower values than reported by *Russell et al.* [2010a]. In Figure 5.11c and Figure 5.11d,  $\omega_o$  also varies significantly in the primary Dust cluster from  $0.89$ - $0.93$ , possibly due to variation in mineral composition of dust [Sokolik and Toon 1999]. For  $\alpha_{ext}$  (Figure 5.11a and Figure 5.11c), the Mixed aerosol type category has two primary density clusters (1) “Mixed-Large Particle” cluster for mainly super-micron particles (centered at  $\alpha_{ext} \sim 0.4$ ) and (2) “Mixed-Small Particle” for mainly submicron particles (centered at  $\alpha_{ext} \sim 1.25$ ). In comparison to the Dust cluster, the Mixed-Large Particle cluster tends to have a slightly smaller contribution to larger particles in the  $0.3$ - $0.6$   $\alpha_{ext}$  range, while  $\eta$  relationships (Figure 5.11b and Figure 5.11d) show the Mixed-Large Particle cluster for coarse particles is nearly identical to the Dust cluster. The Mixed category for mixed sizes ( $0.33 < \eta_{550nm} \leq 0.66$ ) does not show high cluster density due to varying sizes and contributions of the aerosol particles containing dust with strongly varying absorption by pollution or biomass burning smoke [Eck et al., 2010].

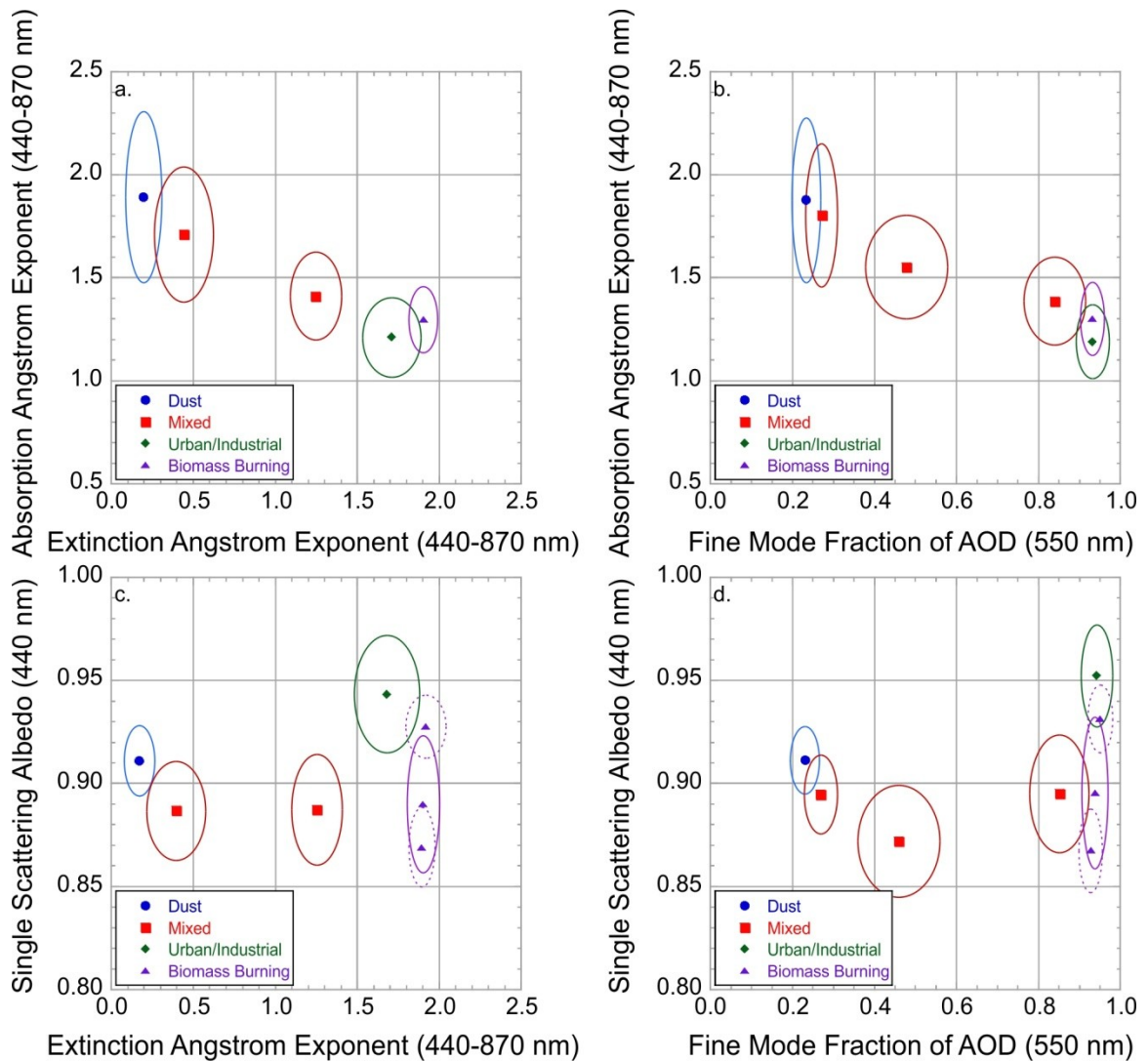


**Figure 5.11** Weighted cluster averages were grouped for each aerosol type category and relationship using AERONET Version 2, Level 2.0 data. The Mixed category averages were calculated using a 0.8 extinction Ångström exponent threshold between mainly small and mainly large particles. For the fine mode fraction of AOD, the Mixed category averages were calculated based on the 0.0-0.33, 0.33-0.66, and 0.66-1.0 ranges. For single scattering albedo plots, the Biomass Burning category was further partitioned by calculating averages using a single scattering albedo threshold of 0.90 to produce two sub-clusters (dashed ellipses) observed in Figure 5.9 and Figure 5.10. Figure from *Giles et al.* [2012].

In Figure 5.11, the Mixed-Small Particle clusters ( $\alpha_{\text{ext}} \sim 1.0$  to  $1.5$ ; also  $\eta \sim 0.8$ - $0.95$ ) show significant variability likely due to variation in carbonaceous particle contribution (primarily BC but also OC) with  $\alpha_{\text{abs}}$  between  $\sim 1.3$  and  $1.7$ , similar to  $\alpha_{\text{abs}}$  values observed at Kanpur for fine mode dominated cases [Giles *et al.*, 2011a]. As indicated by Russell *et al.* [2010a] and shown in Figure 5.6, the U/I and BB category types for the  $\alpha_{\text{abs}}$  and  $\alpha_{\text{ext}}$  relationship tend to overlap each other. For primary density clusters in these two categories, the  $\alpha_{\text{abs}}$  vary from  $\sim 1.1$  to  $1.8$ . Until the  $\omega_0$  uncertainty is known and constrained further (given the sensitivity results of Section 5.4), the usefulness of  $\alpha_{\text{abs}}$  to determine various carbonaceous aerosol particles is doubtful except in separating cases dominated by BC from cases dominated by BrC or OC. A “region” of higher  $\alpha_{\text{abs}}$  values from the density cluster analysis for BB (Figure 5.7d and Figure 5.8d) likely indicates aged smoke from primarily smoldering combustion containing higher concentrations of BrC or OC and relatively low BC [Eck *et al.*, 2009; Moosmüller *et al.*, 2009, 2011], especially above an  $\alpha_{\text{abs}}$  of  $1.6$  for fine mode particles [Lack and Cappa 2010] and also supported by Figure 5.9d and Figure 5.10d with  $\omega_0$  above  $0.90$ . For example, according to Eck *et al.* [2009] and Arola *et al.* [2011], significant absorbing OC concentrations and high OC/BC ratios likely occurred at the Bonanza Creek site where Table 5.2 shows the spectral  $\omega_0$  average is  $\sim 0.95$  and averages of  $\alpha_{\text{abs}}$ ,  $\alpha_{\text{ext}}$ , and  $\eta_{550\text{nm}}$  are  $1.8$ ,  $1.5$ , and  $0.96$ , respectively. The  $\omega_0$  relationships (Figure 5.11c and Figure 5.11d) show more cluster separation than  $\alpha_{\text{abs}}$  relationships (Figure 5.11a and Figure 5.11b). In Figure 5.11d, the primary U/I cluster is centered above  $0.95$ , while the main BB cluster is centered on  $\sim 0.89$  with two BB sub-clusters centered on  $\sim 0.93$  and  $\sim 0.87$   $\omega_0$  (calculated by using  $\omega_0$  threshold of  $0.90$ ); however, the BB clusters overlap with the Mixed-Small Particle

cluster. The  $\omega_{0440\text{nm}}$  and  $\alpha_{\text{ext}440-870\text{ nm}}$  relationship (Figure 5.11c) shows distinct high density clusters in all categories (i.e., between Dust and Mixed-Large Particle, and among Mixed-Small Particle-U/I-BB, and between U/I-BB clusters), while minimal overlap occurs with the U/I and the less absorbing ( $\omega_o > 0.90$ ) BB sub-cluster. Similar aerosol type partitioning was obtained by *Russell et al.* [2010b] using Mahalanobis clustering of  $\omega_{0440\text{nm}}$  and  $\alpha_{\text{ext}440-870\text{ nm}}$  using four AERONET sites (i.e., Beijing, GSFC, Mongu, and Solar Village). In contrast to the density based Voronoi clustering, the Mahalanobis method determines correlations between variables to determine clustering and it is also scale invariant. Nonetheless, the analysis has shown that the  $\omega_{0440\text{nm}}$  and  $\alpha_{\text{ext}440-870\text{ nm}}$  relationship demonstrates that the dominant particle type may be ascertained simply from commonly measured or retrieved aerosol absorption and size parameters.

## Chapter 6: Summary, Conclusions, and Future Work

*Reproduced by permission of American Geophysical Union.*

### 6.1 Summary and Conclusions

The international 2008 TIGERZ experiment intensive operational period was conducted in the Indo-Gangetic Plain around Kanpur, India, during the pre-monsoon (April-June). Mesoscale-distributed ground-based sun photometers quantified temporal and spatial variability of aerosol properties to determine Kanpur urban emission contributions to upwind IGP aerosol loading and validate aerosol retrievals from satellites. Using the long-term Kanpur data set, the climatological aerosol variability during the pre-monsoon was discussed and aerosol absorption and size relationships were evaluated to determine dominant aerosol absorbing types or mixtures. Also in this study, the absorption properties (i.e., single scattering albedo and absorption Ångström exponent) were averaged for 19 AERONET sites to show correspondence to representative aerosol source regions. Sensitivity tests on absorption Ångström exponent were performed by varying the single scattering albedo within plausible constraints based on uncertainty estimates. Lastly, the absorption and size relationships were evaluated and compared to each other based on the dominant aerosol type categorizations.

This study yielded the following conclusions:

- (1) TIGERZ intensive operational period sun photometers quantified AOD increases up to  $\sim 0.10$  within and downwind of the city due to local Kanpur emissions including black carbon. Approximately 10-20% of the aerosol loading detected by ground-based sun photometers on temporary deployment days resulted from the Kanpur city

- emission contributions to the upwind aerosols comprised of a mixture of pollution and dust.
- (2) For a mesoscale case study day with 15-30 km site separation, spatial variability was less than 10% of the area-averages for parameterizations describing the size distribution indicating mainly uniformly sized particles over Kanpur. Spectral single scattering albedo area-averages (0.87-0.93) had stronger absorption at 440 nm due to iron oxides in dust and indicated spatially homogeneous absorption by black carbon and dust particles.
- (3) Aerosol absorption (absorption Ångström exponent) and size (extinction Ångström exponent and fine mode fraction of AOD) relationships showed a non-linear dependence of absorption Ångström exponent over the aerosol size ranges and allowed for the determination of dominant absorbing aerosol types. These relationships along with averaged single scattering albedo spectra were used to categorize black carbon and dust as dominant absorbers and identify a third category where both black carbon and dust dominate absorption. As absorption Ångström exponent decreased to 1.0, coarse mode particles became less dominant for both the annual cycle and pre-monsoon. Further, single scattering albedo transitioned from spectra representing dust (i.e., typical iron oxide absorption in the blue wavelength region and relatively weak absorption in the near-infrared) to urban/industrial pollution containing black carbon (i.e., stronger absorption in longer wavelengths).
- (4) MODIS AOD 3 km and 10 km retrievals with the lowest quality assurance ( $QA \geq 0$ ) flags were biased high with respect to TIGERZ IOP measurements. MODIS AOD 3 km retrievals improved spatial representativeness during some conditions (e.g.,

- clouds) that prohibited the retrieval of 10 km products. MODIS AOD 10 km retrievals with  $QA \geq 0$  had moderate correlation ( $R^2 = 0.52-0.69$ ) with the Kanpur AERONET site, whereas retrievals with  $QA > 0$  were limited in number over the semi-bright land surface. AERONET and MODIS algorithms occasionally misclassified dust as clouds over the IGP during the pre-monsoon.
- (5) A summary of aerosol absorption parameters from the AERONET Version 2, Level 2.0 almucantar retrievals was presented to expand upon previous work using pre-Version 1 retrievals. A comparison of five sites common to *Dubovik et al.* [2002] showed a 0.01 average spectral (from 440 to 1020 nm) decrease in single scattering albedo ( $\omega_0$ ) with the largest decreases spectrally of 0.02 at Capo Verde and GSFC AERONET sites. The average absorption Ångström exponent ( $\alpha_{\text{abs}440-870 \text{ nm}}$ ) computed from Version 2 retrievals was 1.2 lower for Capo Verde and 0.25 higher for GSFC than reported by *Russell et al.* [2010a] computed from pre-Version 1 retrievals. Aerosol mixtures exhibited stronger spectral absorption (i.e., lower  $\omega_0$ ) and increased dominance of absorbing carbonaceous particles (i.e., lower  $\alpha_{\text{abs}440-870 \text{ nm}}$ ) than for dust alone, possibly due to an optical mixture state (e.g., dust and smoke or dust and pollution) or the aggregation of dust and carbonaceous particles.
- (6) The  $\alpha_{\text{abs}440-870 \text{ nm}}$  calculated from AERONET data ranged from  $\sim 0$  to 3.5 among dominant aerosol type categories. Frequency distributions of  $\alpha_{\text{abs}440-870 \text{ nm}}$  exhibited significant overlap among aerosol types, while the Urban/Industrial and Biomass Burning distributions were nearly identical for  $\alpha_{\text{abs}440-870 \text{ nm}}$  values above 1.0. Further, frequency distributions showed approximately 10% of the  $\alpha_{\text{abs}}$  retrievals had values

below 1.0 for most aerosol categories but as high as 22% for the Urban/Industrial category.

- (7) A sensitivity study perturbing the  $\omega_o$  by the current AERONET uncertainty ( $\pm 0.03$ ) showed  $\alpha_{\text{abs}}$  changes by at least  $\sim \pm 0.6$  ( $\pm 20\%$ ) for Dust,  $\sim \pm 0.2$  ( $\pm 7\%$ ) for Mixed, and  $\sim \pm 0.1$  ( $\pm 5\%$ ) for Urban/Industrial and Biomass Burning. The sensitivity study quantified the improvement in estimates of  $\alpha_{\text{abs}}$  resulting from reducing the  $\omega_o$  uncertainty. Variations within the uncertainty of  $\omega_o$  retrievals may explain some of the observed  $\alpha_{\text{abs}}$  values below 1.0 in AERONET data although in situ measurements suggest that some of these  $\alpha_{\text{abs}}$  values may be real depending on the aerosol particle composition and size.
- (8) Absorption and size relationships were examined using density cluster analysis for each dominant aerosol particle type. The  $\omega_{o440\text{nm}}$  vs.  $\alpha_{\text{ext}440-870\text{nm}}$  relationship showed at least five distinct aerosol type clusters [Dust, Mixed-Large Particle, Mixed-Small Particle, Urban/Industrial, and Biomass Burning (with two sub-clusters)], while the  $\alpha_{\text{abs}440-870\text{nm}}$  vs.  $\alpha_{\text{ext}440-870\text{nm}}$  relationship had fewer distinct clusters due to less definition for mainly small aerosol particles ( $\alpha_{\text{ext}440-870\text{nm}} > 1.5$ ).

## 6.2 Future Work

Although the work described in this study advances the current knowledge of aerosols over India, additional effort is needed to understand the long-term impact of Indo-Gangetic Plain aerosols and their effects on air quality, hydrological cycle, and climate. For example, *Lau et al.* [2006] hypothesized from observations and model simulations that the direct radiative heating effects of elevated aerosols act to drive the thermally induced atmospheric circulation over northern India during the pre-monsoon leading to an earlier monsoon progression and subsequent rainfall enhancement over the

Himalayan foothills; a hypothesis known as the Elevated Heat Pump (EHP). *Lau et al.* [2010] used the Goddard Chemistry Aerosol Radiation Transport (GOCART) model monthly aerosol fields as input for numerical experiments using a finite volume general circulation model (fvGCM) when evaluating EHP and its potential effects (e.g., snow melt and changes in surface energy balance). However, *Bollasina and Nigam* [2009] and *Nigam and Bollasina* [2010] indicate an opposite response due to increased heating of aerosols that preclude cloud formation resulting in cooler surface temperatures, slower monsoon propagation, and reduced precipitation over northern India. Assimilation of remotely sensed aerosol observations into aerosol transport models will also help constrain model solutions. Higher spatial and temporal resolution ground-based aerosol measurements are needed to verify aerosol transport models (e.g., GOCART) over in the IGP and complex terrain of the Himalayas (where satellite retrievals are limited) to improve confidence in their depiction of the atmospheric state.

Opportunities still exist to evaluate the 2008-2011 TIGERZ database. For example, *Dumka et al.* [2012, in preparation] will evaluate the multi-year TIGERZ data for the latitudinal distribution of regionally distributed sites to further understand larger spatial scale aerosol variability in the IGP. In addition, the longitudinal aerosol variability across the IGP from Pakistan through northern India still needs to be evaluated to characterize and quantify the spatial and temporal variability of dust and pollution over the region. While aerosol properties from aircraft have been analyzed during the TIGERZ period [*Devi et al.*, 2011], further efforts are needed to analyze data collected also by lidar and aircraft to characterize the aerosol vertical structure over the IGP. The forthcoming Collection 006 MODIS retrieval will have important updates such as an

improved cloud mask and include new aerosol products with 3 km resolution and merged Dark-target and Deep-Blue algorithms. TIGERZ data analysis will be useful in assessing the performance of satellite remote sensing retrievals (e.g., MODIS, MISR, and CALIOP) as well as aerosol transport model output (e.g., GOCART).

Although the absorption and size relationship provides a very good estimation of the dominant mixing states and origins, the exact determination of the dominant mixing state is still not completely conclusive from the absorption and size properties. For example, due to restrictions in the retrieval of single scattering albedo, the aerosol type may be determined when aerosol loading is sufficiently high ( $AOD_{440nm} > 0.4$ ). Thus, the determination of the aerosol type is biased to higher aerosol loading events. Improving the retrieval by reducing the uncertainty (or providing a calculated uncertainty) for each retrieved parameter (e.g., single scattering albedo) may provide the opportunity to include more aerosol events when  $AOD_{440nm} \leq 0.4$ . In addition, use of the absorption Ångström exponent, non-sphericity, or depolarization ratio may allow for further partitioning based on the dominant absorbing type or particle shape [Giles *et al.*, 2011a; Burton *et al.*, 2012]. Improved aerosol classifications by ground-based remote sensing instrumentation should lead to improved satellite retrievals. Vertically integrated in situ measurements from aircraft of single scattering albedo and absorption Ångström exponent obtained during air quality measurement campaigns (e.g. DISCOVER-AQ) will help constrain uncertainty estimates and provide the opportunity to further validate AERONET retrievals.

## Bibliography

- Anderson, T. L., et al. (2005), An “A-Train” Strategy for Quantifying Direct Climate Forcing by Anthropogenic Aerosols, *Bull. Amer. Met. Soc.*, doi:10.1175/BAMS-86-12-1795.
- Ångström, A. (1964), The parameters of atmospheric turbidity, *Tellus*, 16(1), 64–75.
- Arimoto, R., et al. (2006), Characterization of Asian Dust during ACE-Asia, *Global Planet. Change*, 52, doi:10.1016/j.gloplacha.2006.02.013.
- Arola, A., G. Schuster, G. Myhre, S. Kazadzis, S. Dey, and S. N. Tripathi (2011), Inferring absorbing organic carbon content from AERONET data, *Atmos. Chem. Phys.*, 11, doi:10.5194/acp-11-215-2011.
- Basart, S., C. Pérez, E. Cuevas, J. M. Baldasano, and G. P. Gobbi (2009), Aerosol characterization in Northern Africa, Northeastern Atlantic, Mediterranean Basin and Middle East from direct-sun AERONET observations, *Atmos. Chem. Phys.*, 9, 8265-8282, doi:10.5194/acp-9-8265-2009.
- Beegum, S. N., et al. (2008), Characteristics of spectral aerosol optical depths over India during ICARB, *J. Earth Syst. Sci.*, 117, S1, 303-313.
- Bergstrom, R. W., P. B. Russell, and P. Hignett (2002), Wavelength dependence of the absorption of black carbon particles: Predictions and results from the TARFOX experiment and implications for the aerosol single scattering albedo, *J. Atmos. Sci.*, 59, 567–577, doi:10.1175/1520-0469(2002)059<0567:WDOTAO>2.0.CO;2.
- Bergstrom, R. W., P. Pilewskie, P. B. Russell, J. Redemann, T. C. Bond, P. K. Quinn, and B. Sierau (2007), Spectral absorption properties of atmospheric aerosols, *Atmos. Chem. Phys.*, 7, 5937–5943, doi:10.5194/acp-7-5937-2007.
- Bollasina, M., and S. Nigam (2009), Absorbing aerosols and pre-summer monsoon hydroclimate variability over the Indian subcontinent: The challenge in investigating links, *Atmos. Res.*, 94, doi:10.1016/j.atmosres.2009.06.008.
- Boselli A., R. Caggiano, C. Cornacchia, F. Madonna, L. Mona, M. Macchiato, G. Pappalardo, and S. Trippetta (2012), Multi year sun-photometer measurements for aerosol characterization in a Central Mediterranean site, *J. Atmos. Res.*, 104-105, 98-110, doi: 10.1016/j.atmosres.2011.08.002.
- Burton, S. P., R. A. Ferrare, C. A. Hostetler, J. W. Hair, R. R. Rogers, M. D. Obland, C. F. Butler, A. L. Cook, D. B. Harper, and K. D. Froyd (2012), Aerosol classification using airborne High Spectral Resolution Lidar measurements – methodology and examples, *Atmos. Meas. Tech.*, 5, 73-98, doi:10.5194/amt-5-73-2012.

- Cattrell, C., J. Reagan, K. Thome, and O. Dubovik (2005), Variability of aerosol and spectral lidar and backscatter and extinction ratios of key aerosol types derived from selected Aerosol Robotic Network locations, *J. Geophys. Res.*, *110*, D10S11, doi:10.1029/2004JD005124.
- Chaudhry, Z., J. V. Martins, Z. Li, S.-C. Tsay, H. Chen, P. Wang, T. Wen, C. Li, and R. R. Dickerson (2007), In situ measurements of aerosol mass concentration and radiative properties in Xianghe, southeast of Beijing, *J. Geophys. Res.*, *112*, D23S90, doi:10.1029/2007JD009055.
- Chin, M., T. Diehl, O. Dubovik, T. F. Eck, B. N. Holben, A. Sinyuk, and D. G. Streets (2009), Light absorption by pollution, dust, and biomass burning aerosols: a global model study and evaluation with AERONET measurements, *Ann. Geophys.*, *27*, 3439-3464, doi: 10.5194/angeo-27-3439-2009.
- Chinnam, N., S. Dey, S. N. Tripathi, and M. Sharma (2006), Dust events in Kanpur, northern India: Chemical evidence for source and implications to radiative forcing, *Geophys. Res. Lett.*, *33*, L08803, doi:10.1029/2005GL025278.
- Chu, D. A., Y. J. Kaufman, G. Zibordi, J. D. Chern, J. Mao, C. Li, and B. N. Holben (2003), Global monitoring of air pollution over land from the Earth Observing System-Terra Moderate Resolution Imaging Spectroradiometer (MODIS), *J. Geophys. Res.*, *108*(D21), 4661, doi:10.1029/2002JD003179.
- Derimian, Y., A. Karnieli, Y. J. Kaufman, M. O. Andreae, T. W. Andreae, O. Dubovik, W. Maenhaut, I. Koren, and B. N. Holben (2006), Dust and pollution aerosols over the Negev desert, Israel: Properties, transport, and radiative effect, *J. Geophys. Res.*, *111*, D05205, doi:10.1029/2005JD006549.
- Derimian, Y., A. Karnieli, Y. J. Kaufman, M. O. Andreae, T. W. Andreae, O. Dubovik, W. Maenhaut, and I. Koren (2008), The role of iron and black carbon in aerosol light absorption, *Atmos. Chem. Phys.*, *8*, 3623–3637, doi:10.5194/acp-8-3623-2008.
- Devi, J. J., S. N. Tripathi, T. Gupta, B. N. Singh, V. Gopalakrishnan, and S. Dey (2011), Observation-based 3-D view of aerosol radiative properties over Indian Continental Tropical Convergence Zone: implications to regional climate, *Tellus*, *63B*, 971-989, doi: 10.1111/j.1600-0889.2011.00580.x.
- Dey, S., and L. Di Girolamo (2010), A climatology of aerosol optical and microphysical properties over the Indian subcontinent from 9 years (2000-2008) of Multiangle Imaging Spectroradiometer (MISR) data, *J. Geophys. Res.*, *115*, D15204, doi:10.1029/2009JD013395.
- Dey, S., and S. N. Tripathi (2007), Estimation of aerosol optical properties and radiative effects in the Ganga basin, northern India, during the wintertime, *J. Geophys. Res.*, *112*, D03203, doi:10.1029/2006JD007267.

- Dey, S., S. N. Tripathi, and S. K. Mishra (2008), Probable mixing state of aerosols in the Indo-Gangetic Basin, northern India, *Geophys. Res. Lett.*, *35*, L03808, doi:10.1029/2007GL032622.
- Dey, S., S. N. Tripathi, R. P. Singh, and B. N. Holben (2004), Influence of dust storms on the aerosol optical properties over the Indo-Gangetic basin, *J. Geophys. Res.*, *109*, D20211, doi:10.1029/2004JD004924.
- Dey, S., S. N. Tripathi, R. P. Singh, and B. N. Holben (2005), Seasonal variability of the aerosol parameters over Kanpur, an urban site in Indo-Gangetic basin, *Adv. Space Res.*, *36*, doi: doi:10.1016/j.asr.2005.06.040.
- Dickerson, R. R., M. O. Andreae, T. Campos, O. L. Mayol-Bracero, C. Neusuess, and D. G. Streets (2002), Analysis of black carbon and carbon monoxide observed over the Indian Ocean: Implications for emissions and photochemistry, *J. Geophys. Res.*, *107*, D19, doi:10.1029/2001JD000501.
- Diner, D. J., G. P. Asner, R. Davies, Y. Knyazikhin, J.-P. Muller, A. W. Nolin, B. Pinty, C. B. Schaaf, and J. Stroeve (1999), New Directions in Earth Observing: Scientific Applications of Multiangle Remote Sensing, *Bull. Amer. Meteor. Soc.*, *80*, 2209–2228, doi: [http://dx.doi.org/10.1175/1520-0477\(1999\)080<2209:NDIEOS>2.0.CO;2](http://dx.doi.org/10.1175/1520-0477(1999)080<2209:NDIEOS>2.0.CO;2).
- Draxler, R. R., and G. D. Rolph (2010), HYSPLIT (HYbrid Single-Particle Lagrangian Integrated Trajectory) Model access via NOAA ARL READY Website (<http://ready.arl.noaa.gov/HYSPLIT.php>), NOAA Air Resources Laboratory, Silver Spring, MD.
- Dubovik, O. and M. D. King (2000), A flexible inversion algorithm for retrieval of aerosol optical properties from Sun and sky radiance measurements, *J. Geophys. Res.*, *105*, 20 673–20 696.
- Dubovik, O., A. Smirnov, B. N. Holben, M. D. King, Y. J. Kaufman, T. F. Eck, and I. Slutsker (2000), Accuracy assessments of aerosol optical properties retrieved from AERONET Sun and sky-radiance measurements, *J. Geophys. Res.*, *105*, D8, 9791–9806, doi:10.1029/2000JD900040.
- Dubovik, O., B. N. Holben, T. F. Eck, A. Smirnov, Y. J. Kaufman, M. D. King, D. Tanre, and I. Slutsker (2002), Variability of absorption and optical properties of key aerosol types observed in worldwide locations, *J. Atmos. Sci.*, *59*, 590–608, doi:10.1175/1520-0469(2002)059<0590:VOAAOP>2.0.CO;2.
- Dubovik, O., et al. (2006), Application of spheroid models to account for aerosol particle nonsphericity in remote sensing of desert dust, *J. Geophys. Res.*, *111*, D11208, doi:10.1029/2005JD006619.
- Dumka, U. C., S. N. Tripathi, D. M. Giles, T. F. Eck, R. Sagar, and B. N. Holben (2012), Latitudinal Variation of Aerosol Properties from Indo-Gangetic Plain (IGP) to

Central Himalayas Foothills during TIGERZ Campaign, *J. Geophys. Res.*, in preparation.

- Eck, T. F., B. N. Holben, J. S. Reid, O. Dubovik, A. Smirnov, N. T. O'Neill, I. Slutsker, and S. Kinne (1999), Wavelength dependence of the optical depth of biomass burning, urban and desert dust aerosols, *J. Geophys. Res.*, *104*, 31 333–31 350.
- Eck, T. F., B. N. Holben, O. Dubovik, A. Smirnov, I. Slutsker, J. M. Lobert, and V. Ramanathan (2001), Column-integrated aerosol optical properties over the Maldives during the northeast monsoon for 1998–2000, *J. Geophys. Res.*, *106*(D22), 28,555–28,566, doi:10.1029/2001JD000786.
- Eck, T. F., et al. (2003a), Variability of biomass burning aerosol optical characteristics in southern Africa during the SAFARI 2000 dry season campaign and a comparison of single scattering albedo estimates from radiometric measurements, *J. Geophys. Res.*, *108*(D13), 8477, doi:10.1029/2002JD002321.
- Eck, T. F., B. N. Holben, J. S. Reid, N. T. O'Neill, J. S. Schafer, O. Dubovik, A. Smirnov, M. A. Yamasoe, and P. Artaxo (2003b), High aerosol optical depth biomass burning events: A comparison of optical properties for different source regions, *Geophys. Res. Lett.*, *30*(20), 2035, doi:10.1029/2003GL017861.
- Eck, T. F., et al. (2005), Columnar aerosol optical properties at AERONET sites in central eastern Asia and aerosol transport to the tropical mid-Pacific, *J. Geophys. Res.*, *110*, D06202, doi:10.1029/2004JD005274.
- Eck, T. F., et al. (2008), Spatial and temporal variability of column-integrated aerosol optical properties in the southern Arabian Gulf and United Arab Emirates in summer, *J. Geophys. Res.*, *113*, D01204, doi:10.1029/2007JD008944.
- Eck, T. F., et al. (2009), Optical properties of boreal region biomass burning aerosols in central Alaska and seasonal variation of aerosol optical depth at an Arctic coastal site, *J. Geophys. Res.*, *114*, D11201, doi:10.1029/2008JD010870.
- Eck, T. F., et al. (2010), Climatological aspects of the optical properties of fine/coarse mode aerosol mixtures, *J. Geophys. Res.*, *115*, D19205, doi:10.1029/2010JD014002.
- Forester, P. et al. (2007), Changes in Atmospheric Constituents and in Radiative Forcing. *In: Climate Change 2007: The Physical Science Basis. Contributions of Working Group I to the Fourth Assessment Report of the Intergovernmental Panel on Climate Change (IPCC)* [Solomon, S., D. Qin, M. Manning, Z. Chen, M. Marquis, K. B. Averyt, M. Tignor, and H. L. Miller (eds.)]. Cambridge University Press, Cambridge, United Kingdom and New York, NY, USA.
- Garland, R. M., et al. (2008), Aerosol optical properties in a rural environment near the mega-city Guangzhou, China: implications for regional air pollution, radiative forcing and remote sensing, *Atmos. Chem. Phys.*, *8*, 5161-5186.

- Gautam, R., Z. Liu, R. P. Singh and N. C. Hsu (2009), Two contrasting dust-dominant periods over India observed from MODIS and CALIPSO data, *Geophys. Res. Lett.*, *36*, L06813, doi:10.1029/2008GL036967.
- Gautam, R., N. C. Hsu, and K.-M. Lau (2010), Premonsoon aerosol characterization and radiative effects over the Indo-Gangetic Plains: Implications for regional climate warming, *J. Geophys. Res.*, *115*, D17208, doi:10.1029/2010JD013819.
- Giles, D. M., et al. (2010), Identifying Aerosol Type/Mixture from Aerosol Absorption Properties Using AERONET, *Eos Trans. AGU*, *91*(26), West. Pac. Geophys. Meet. Suppl., Abstract A33D-05.
- Giles, D. M., et al. (2011a), Aerosol properties over the Indo-Gangetic Plain: A mesoscale perspective from the TIGERZ experiment, *J. Geophys. Res.*, *116*, D18203, doi:10.1029/2011JD015809. Copyright 2011 American Geophysical Union.
- Giles, D. M., B. N. Holben, T. F. Eck, A. Sinyuk, A. Smirnov, I. Slutsker, R. R. Dickerson, A. M. Thompson, and J. S. Schafer (2011b), Dominant Aerosol Particle Type/Mixture Identification at Worldwide Locations Using the Aerosol Robotic Network (AERONET), Abstract A14E-07 presented at 2011 Fall Meeting, AGU, San Francisco, Calif., 5-9 Dec.
- Giles, D. M., B. N. Holben, T. F. Eck, A. Sinyuk, A. Smirnov, I. Slutsker, R. R. Dickerson, A. M. Thompson, and J. S. Schafer (2012), An Analysis of AERONET Aerosol Absorption Properties and Classifications Representative of Aerosol Source Regions, *J. Geophys. Res.*, *117*, D17203, doi:10.1029/2012JD018127. Copyright 2012 American Geophysical Union.
- Ginoux, P., D. Garbuzov, and N. C. Hsu (2010), Identification of anthropogenic and natural dust sources using Moderate Resolution Imaging Spectroradiometer (MODIS) Deep Blue level 2 data, *J. Geophys. Res.*, *115*, D05204, doi:10.1029/2009JD012398.
- Gobbi, G. P., Y. J. Kaufman, I. Koren, and T. F. Eck (2007), Classification of aerosol properties derived from AERONET direct sun data, *Atmos. Chem. Phys.*, *7*, 453-458, doi:10.5194/acp-7-453-2007.
- Gogoi, M. M., K. Krishna Moorthy, S. S. Babu, and P. K. Bhuyan (2009), Climatology of columnar aerosol properties and the influence of synoptic conditions: First-time results from the northeastern region of India, *J. Geophys. Res.*, *114*, D08202, doi:10.1029/2008JD010765.
- Guo, Z., Z. Li, J. Farquhar, A. J. Kaufman, N. Wu, C. Li, R. R. Dickerson, and P. Wang (2010), Identification of sources and formation processes of atmospheric sulfate by sulfur isotope and scanning electron microscope measurements, *J. Geophys. Res.*, *115*, D00K07, doi:10.1029/2009JD012893.

- Gustafsson, Ö, M. Kruså, Z. Zencak, R. Sheesley, L. Granat, E. Engström, P. S. P. Rao, C. Leck, and H. Rodhe (2009), Brown Clouds over South Asia: Biomass or Fossil Fuel Combustion?, *Science*, *323*, 10.1126/science.1164857.
- Gyawali, M., et al. (2012), Photoacoustic optical properties at UV, VIS, and near IR wavelengths for laboratory generated and winter time ambient urban aerosols, *Atmos. Chem. Phys.*, *12*, 2587-2601, doi:10.5194/acp-12-2587-2012.
- Hay, J. E., and P. W. Suckling (1979), An assessment of the networks for measuring and modeling solar radiation in British Columbia and adjacent areas of western Canada, *Canadian Geography*, *23*, 222-238.
- Holben, B. N., T. F. Eck, and R. S. Fraser (1991), Temporal and spatial variability of aerosol optical depth in the Sahel region in relation to vegetation remote sensing, *Int. J. Remote Sens.*, *12*(6), 1147–1163, doi:10.1080/01431169108929719.
- Holben, B. N., et al. (1998), AERONET—A federated instrument network and data archive for aerosol characterization, *Remote Sens. Environ.*, *66*, 1–16, doi:10.1016/S0034-4257(98)00031-5.
- Holben, B. N., et al. (2001), An emerging ground-based aerosol climatology: Aerosol optical depth from AERONET, *J. Geophys. Res.*, *106*(D11), 12,067–12,097, doi:10.1029/2001JD900014.
- Holben, B. N., T. F. Eck, I. Slutsker, A. Smirnov, A. Sinyuk, J. Schafer, D. Giles, O. Dubovik (2006), AERONET's Version 2.0 quality assurance criteria, in Remote Sensing of Atmosphere and Clouds, *Proc. SPIE Int. Soc. Opt. Eng.*, *6408*, 64080Q, doi:10.1117/12.706524.
- Hsu, N. C., S.-C. Tsay, M. D. King, J. R. Herman (2006), Deep Blue Retrievals of Asian Aerosol Properties During ACE-Asia, *IEEE Trans. Geosci and Rem. Sens.*, *44*, 11, doi:10.1109/TGRS.2006.879540.
- Hyer, E. J., J. S. Reid, and J. Zhang (2011), An over-land aerosol optical depth data set for data assimilation by filtering, correction, and aggregation of MODIS Collection 5 optical depth retrievals, *Atmos. Meas. Tech.*, *4*, doi:10.5194/amt-4-379-2011.
- Ichoku, C., D. A. Chu, S. Mattoo, Y. J. Kaufman, L. Remer, D. Tanre, I. Slutsker, and B. Holben (2002), A spatio-temporal approach for global validation and analysis of MODIS aerosol products, *Geophys. Res. Lett.*, *29* (12), 1616, doi: 10.1029/2001GL013206.
- Ichoku, C., L. A. Remer, and T. F. Eck (2005), Quantitative evaluation and intercomparison of morning and afternoon Moderate Resolution Imaging Spectroradiometer (MODIS) aerosol measurement from Terra and Aqua, *J. Geophys. Res.*, *10*, D10S03, doi:10.1029/2004JD004987.

- Ishimoto, H., Y. Zaizen, A. Uchiyama, K. Masuda, Y. Mano (2010), Shape modeling of mineral dust particles for light-scattering calculations using the spatial Poisson–Voronoi tessellation, *J. of Quant. Spect. and Rad. Trans.*, *111*, 16, doi:10.1016/j.jqsrt.2010.06.018.
- Jacobson, M. Z. (2001), Strong radiative heating due to the mixing state of black carbon in atmospheric aerosols, *Nature*, *409*, 695-697.
- Jeong, M.-J., and Z. Li (2005), Quality, compatibility, and synergy analyses of global aerosol products derived from the advanced very high resolution radiometer and Total Ozone Mapping Spectrometer, *J. Geophys. Res.*, *110*, D10S08, doi:10.1029/2004JD004647.
- Jethva, H., S. K. Satheesh, and J. Srinivasan (2005), Seasonal variability of aerosols over the Indo-Gangetic basin, *J. Geophys. Res.*, *110*, D21204, doi:10.1029/2005JD005938.
- Jethva, H., S. K. Satheesh, and J. Srinivasan (2006), Systematic Bias in MODIS Dust Aerosol Retrieval at Kanpur (AERONET), Indo-Gangetic Basin, *Rem. Sens. Atmos. Clouds, Proc. of SPIE*, *6408*, 640816, doi: 10.1117/12.694952.
- Jethva, H., S. K. Satheesh, and J. Srinivasan (2007a), Evaluation of MODIS C004 aerosol retrievals at Kanpur, Indo-Gangetic basin, *J. Geophys. Res.*, *112*, D14216, doi:10.1029/2006JD007929.
- Jethva, H., S. K. Satheesh, and J. Srinivasan (2007b), Assessment of second-generation MODIS retrieval (Collection 005) at Kanpur, India, *Geophys. Res. Lett.*, *34*, L19802, doi: 10.1029/2007GL029647.
- Jethva, H., S. K. Satheesh, J. Srinivasan, and R. C. Levy (2010), Improved retrieval of aerosol size-resolved properties from moderate resolution imaging spectroradiometer over India: Role of aerosol model and surface reflectance, *J. Geophys. Res.*, *115*, D18213, doi: 10.1029/2009JD013218.
- Johnson, B. T., S. Christopher, J. M. Haywood, S. R. Osborne, S. McFarlane, C. Hsu, C. Salustro, and R. Kahn (2009), Measurements of aerosol properties from aircraft and ground-based remote sensing: A case-study from the Dust and Biomass-burning Experiment (DABEX), *Q. J. R. Met. Soc.*, *135*, doi:10.1002/qj.420.
- Junge, C., (1955), The size distribution and aging of natural aerosols as determined from electrical and optical data on the atmosphere, *J. Meteor.*, *12*, 13–25. doi: [http://dx.doi.org/10.1175/1520-0469\(1955\)012<0013:TSDAAO>2.0.CO;2](http://dx.doi.org/10.1175/1520-0469(1955)012<0013:TSDAAO>2.0.CO;2).
- Kahn, R. A., B. J. Gaitley, J. V. Martonchik, D. J. Diner, and K. A. Crean (2005), Multiangle Imaging Spectroradiometer (MISR) global aerosol optical depth validation based on 2 years of coincident Aerosol Robotic Network (AERONET) observations, *J. Geophys. Res.*, *110*, D10S04, doi:1029/2004JD004706.

- Kahn, R. A., B. J. Gaitley, M. J. Garay, D. J. Diner, T. F. Eck, A. Smirnov, and B. N. Holben (2010), Multiangle Imaging Spectroradiometer global aerosol product assessment by comparison with the Aerosol Robotic Network, *J. Geophys. Res.*, *115*, D23209, doi:10.1029/2010JD014601.
- Kalapureddy, M. C. R., D. G. Kaskaoutis, P. Ernest Raj, P. C. S. Devara, H. D. Kambezidis, P. G. Kosmopoulos, and P. T. Nastos (2009), Identification of aerosol type over the Arabian Sea in the premonsoon season during the Integrated Campaign for Aerosols, Gases and Radiation Budget (ICARB), *J. Geophys. Res.*, *114*, D17203, doi:10.1029/2009JD011826.
- Kar, J., M. N. Deeter, J. Fishman, Z. Liu, A. Omar, J. K. Creilson, C. R. Trepte, M. A. Vaughan, and D. M. Winker (2010), Wintertime pollution over the Eastern Indo-Gangetic Plains as observed from MOPITT, CALIPSO, and tropospheric ozone residual data, *Atmos. Chem. Phys.*, *10*, doi:10.5194/acp-10-12273-2010.
- Kaufman, Y. J., A. Setzer, D. Ward, D. Tanre, B. N. Holben, P. Menzel, M. C. Pereira, and R. Rasmussen (1992), Biomass Burning Airborne and Spaceborne Experiment in the Amazonas (BASE-A), *J. Geophys. Res.*, *97*(D13), 14,581–14,599, doi:10.1029/92JD00275.
- Kaufman, Y. J., D. Tanre, L. A. Remer, E. F. Vermote, A. Chu, and B. N. Holben (1997), Operational remote sensing of tropospheric aerosol over land from EOS moderate resolution imaging spectroradiometer, *J. Geophys. Res.*, *102*, D14, 17 051–17 067.
- Kim, D., M. Chin, H. Yu, T. F. Eck, A. Sinyuk, A. Smirnov, and B. N. Holben (2011), Dust optical properties over North Africa and Arabian Peninsula derived from the AERONET dataset, *Atmos. Chem. Phys.*, *11*, 10733-10741, doi:10.5194/acp-11-10733-2011.
- Kinne, S., T. P. Akerman, M. Shiobara, A. Uchiyama, A. J. Heymsfield, L. Miloshevich, J. Wendell, E. W. Eloranta, C. Purgold, and R. W. Bergstrom (1997), Cirrus Cloud Radiative and Microphysical Properties from Ground Observations and In Situ Measurements during FIRE 1991 and Their Application to Exhibit Problems in Cirrus Solar Radiative Transfer Modeling, *J. Atmos. Sci.*, *54*, doi: 10.1175/1520-0469(1997)054<2320:CCRAMP>2.0.CO;2.
- Kirchstetter, T. W. and T. Novakov (2004), Evidence that the spectral dependence of light absorption by aerosols is affected by organic carbon, *J. Geophys. Res.*, *109*, D21208, doi:10.1029/2004JD004999.
- Kriegler, F.J., Malila, W.A., Nalepka, R.F. and Richardson, W. (1969), Preprocessing transformations and their effect on multispectral recognition, in: *Proc. 6th ISRSE*, University of Michigan, Ann Arbor, MI, pp. 97-131.
- Kumar, S., A. K. Singh, A. K. Prasad, and R. P. Singh (2011), Variability of GPS derived water vapor and comparison with MODIS data over the Indo-Gangetic plains, *J. Phys. Chem. Earth*, doi:10.1016/j.pce.2010.03.040, in press.

- Lack, D. A. and C. D. Cappa (2010), Impact of brown and clear carbon on light absorption enhancement, single scatter albedo and absorption wavelength dependence of black carbon, *Atmos. Chem. Phys.*, *10*, 4207-4220, doi:10.5194/acp-10-4207-2010.
- Lau, K.-M. and K.-M Kim (2006), Observational relationships between aerosol and Asian monsoon rainfall, and circulation, *Geophys. Res. Lett.*, *33*, L21810, doi: 10.1029/2006GL027546.
- Lau, K. M., M. K. Kim, and K. M. Kim (2006), Asian summer monsoon anomalies by aerosol direct forcing: the role of the Tibetan Plateau, *Clim. Dyn.*, *26*, doi:10.1007/s00382-006-0114-z.
- Lau K.-M. et al. (2008), The Joint Aerosol-Monsoon Experiment – A New Challenge for Monsoon Climate Research, *Bull. Amer. Met. Soc.*, *89*, doi:10.1175/BAMS-89-3-369.
- Lau K.-M., M.-K. Kim, K.-M. Kim, and W.-S. Lee (2010), Enhanced surface warming and accelerated snow melt in the Himalayas and Tibetan Plateau induced by absorbing aerosols, *Environ. Res. Lett.*, *5*, 10.1088/1748-9326/5/2/025204.
- Leahy, L. V., T. L. Anderson, T. F. Eck, and R. W. Bergstrom (2007), A synthesis of single scattering albedo of biomass burning aerosol over southern Africa during SAFARI 2000, *Geophys. Res. Lett.*, *34*, L12814, doi:10.1029/2007GL029697.
- Lee J., J. Kim, C.H. Song, S.B. Kim, Y. Chun, B.J. Sohn, and B.N. Holben (2010), Characteristics of aerosol types from AERONET sunphotometer measurements, *Atmos. Environ.*, *44*, 26, doi: 10.1016/j.atmosenv.2010.05.035.
- Lelieveld, J. et al. (2001), The Indian Ocean Experiment: Widespread Air Pollution from South and Southeast Asia, *Science*, *291*, 1031-1036.
- Levy, R., L. A. Remer, J. V. Martins, Y., J. Kaufman, A. Plana-Fattori, J. Redemann and B. Wenny (2005), Evaluation of the MODIS Aerosol Retrievals over Ocean and Land during CLAMS, *J. Atmos. Sci. – Special Section*, *62*, 974-992.
- Levy, R. C., L. A. Remer, and O. Dubovik (2007a), Global aerosol optical properties and application to Moderate Resolution Imaging Spectroradiometer aerosol retrieval over land, *J. Geophys. Res.*, *112*, D13210, doi:10.1029/2006JD007815.
- Levy, R., C., L. A. Remer, S. Mattoo, E. F. Vermote, and Y. J. Kaufman (2007b), Second-generation operational algorithm: Retrieval of aerosol properties over land from inversion of Moderate Resolution Imaging Spectroradiometer spectral reflectance, *J. Geophys. Res.*, *112*, D13211, doi: 10.1029/2006JD007811.
- Lewis, K., W. P. Arnott, H. Moosmüller and C. E. Wold (2008), Strong spectral variation of biomass smoke light absorption and single scattering albedo observed with a novel dual-wavelength photoacoustic instrument, *J. Geophys. Res.*, *113*, D16203, doi:10.1029/2007JD009699.

- Littman, T. (1991), Dust Storm Frequency in Asia: Climatic Control and Variability, *Intl. J. Climatology*, *11*, 393-412.
- Mani, A., O. Chacko, and S. Hariharan (1969), A Study of Angstrom's turbidity parameters from solar radiation measurements in India, *Tellus*, *21*, doi:10.1111/j.2153-3490.1969.tb00489.x.
- Martins, J. V., P. Artaxo, C. Liousse, J. S. Reid, P. V. Hobbs, and Y. J. Kaufman (1998), Effects of black carbon content, particle size, and mixing on light absorption by aerosols from biomass burning in Brazil, *J. Geophys. Res.*, *103*(D4), 32,041-32,050, doi: 10.1029/98JD02593.
- McCormick, M. P., L. W. Thomason, and C. R. Trepte (1995), Atmospheric effects of the Mt Pinatubo eruption, *Nature*, *373*, doi: 10.1038/373399a0.
- McPherson, C. J., J. A. Reagan, J. Schafer, D. Giles, R. Ferrare, J. Hair, and C. Hostetler (2010), AERONET, airborne HSRL, and CALIPSO aerosol retrievals compared and combined: A case study, *J. Geophys. Res.*, *115*, D00H21, doi:10.1029/2009JD012389.
- Mélin, F., and G. Zibordi (2005), Aerosol variability in the Po Valley analyzed from automated optical measurements, *Geophys. Res. Lett.*, *32*, L03810, doi:10.1029/2004GL021787.
- Menon, S., J. Hansen, L. Nazarenko, Y. Luo (2002), Climate Effects of Black Carbon Aerosols in China and India, *Science*, *297*, 2250, doi:10.1126/science.1075159.
- Middleton, N. J. (1986), A Geography of Dust Storms in Southwest Asia, *J. Climatology*, *6*, 183-196.
- Mielonen, T., A. Arola, M. Komppula, J. Kukkonen, J. Koskinen, G. de Leeuw, and K. E. J. Lehtinen (2009), Comparison of CALIOP level 2 aerosol subtypes to aerosol types derived from AERONET inversion data, *Geophys. Res. Lett.*, *36*, L18804, doi:10.1029/2009GL039609.
- Mishra A., A. Jayaraman, and D. Ganguly (2008), Validation of MODIS derived aerosol optical depth over Western India, *J. Geophys. Res.*, *113*, D04203, doi:10.1029/2007JD009075.
- Mitchell, R. M., D. M. O'Brien, and S. K. Campbell (2006), Characteristics and radiative impact of the aerosol generated by the Canberra firestorm of January 2003, *J. Geophys. Res.*, *111*, D02204, doi:10.1029/2005JD006304.
- Moorthy, K. K., and S. S. Babu (2005), Aerosol Characteristics and Radiative Impacts over the Arabian Sea during the Intermonsoon Season: Results from ARMEX Field Campaign, *J. Atmos. Sci.*, *62*, doi:10.1175/JAS-3378.1.
- Moorthy, K. K., P. R. Nair, and B. V. K. Murthy (1989), Multiwavelength solar radiometer network and features of aerosol spectral optical depth at Trivandrum. *Ind. J. Radio Space Phys.*, *18*, 194-201.

- Moorthy, K. K., S. S. Babu, S. K. Satheesh, J. Srinivasan, and C. B. S. Dutt (2007), Dust absorption over the “Great Indian Desert” inferred using ground-based and satellite remote sensing, *J. Geophys. Res.*, *112*, D09206, doi:10.1029/2006JD007690.
- Moorthy, K. K., S. K. Satheesh, S. S. Babu, and C. B. S. Dutt (2008), Integrated Campaign for Aerosols, gases and Radiation Budget (ICARB): An overview, *J. Earth Syst. Sci.*, *117*, S1, 243-262.
- Moosmüller H., R. K. Chakrabarty, and W. P. Arnott (2009), Aerosol light absorption and its measurement: A review, *J. of Quant. Spect. and Rad. Trans.*, *110*, 11, doi:10.1016/j.jqsrt.2009.02.035.
- Moosmüller, H., R. K. Chakrabarty, K. M. Ehlers, and W. P. Arnott, (2011), Absorption Ångström coefficient, brown carbon, and aerosols: basic concepts, bulk matter, and spherical particles, *Atmos. Chem. Phys.*, *11*, 1217-1225, doi:10.5194/acp-11-1217-2011.
- Morys, M., F. M. Mims III, S. Hagerup, S. E. Anderson, A. Baker, J. Kia, and T. Walkup (2001), Design, calibration, and performance of MICROTOPS II handheld ozone monitor and Sun photometer, *J. Geophys. Res.*, *106*, doi:10.1029/2001JD900103.
- Müller, D., et al. (2010), Mineral dust observed with AERONET Sun photometer, Raman lidar, and in situ instruments during SAMUM 2006: Shape-independent particle properties, *J. Geophys. Res.*, *115*, D07202, doi:10.1029/2009JD012520.
- Nigam, S., and M. Bollasina (2010), “Elevated heat pump” hypothesis for the aerosol monsoon hydroclimate link: “Grounded” in observations?, *J. Geophys. Res.*, *115*, D16201, doi:10.1029/2009JD013800.
- Niranjan, K., B. M. Rao, P. S. Brahmanandam, B. L. Madhavan, V. Sreekanth, and K. K. Moorthy (2005), Spatial characteristics of aerosol physical properties over the northeastern parts of peninsular India, *Annales Geophys.*, *23*, 3219-3227.
- Omar, A. H., J.-G. Won, D. M. Winker, S.-C. Yoon, O. Dubovik, and M. P. McCormick (2005), Development of global aerosol models using cluster analysis of Aerosol Robotic Network (AERONET) measurements, *J. Geophys. Res.*, *110*, D10S14, doi:10.1029/2004JD004874.
- O'Neill, N. T., T. F. Eck, B. N. Holben, A. Smirnov, O. Dubovik, and A. Royer (2001), Bimodal size distribution influences on the variation of Angstrom derivatives in spectral and optical depth space, *J. Geophys. Res.*, *106*, 9787-9806.
- O'Neill, N. T., T. F., Eck, A. Smirnov, B. N. Holben, S. Thulasiraman (2003), Spectral discrimination of coarse and fine mode optical depth, *J. Geophys. Res.*, *108*, D17, 4559-4573, 10.1029/2002JD002975.

- O'Neill, N. T., S. Thulasiraman, T. F. Eck, and J. S. Reid (2005), Robust optical features of fine mode size distributions: Application to the Québec smoke event of 2002, *J. Geophys. Res.*, *110*, D11207, doi:10.1029/2004JD005157.
- Orlanski, I. (1975), Rational Subdivision of Scales for Atmospheric Processes, *Bull. Amer. Met. Soc.*, *56*, 5, 527-530.
- Pinker, R. T., B. Zhang, and E. G. Dutton (2005), Do satellites detect trends in surface solar radiation, *Science*, *308*, doi:10.1126/science.1103159.
- Prasad, A. K., and R. P. Singh (2007a), Changes in aerosol parameters during major dust storm events (2001-2005) over the Indo-Gangetic Plains using AERONET and MODIS data, *J. Geophys. Res.*, *112*, D09208, doi:10.1029/2006JD007778.
- Prasad, A. K., and R. P. Singh (2007b), Comparison of MISR-MODIS aerosol optical depth over the Indo-Gangetic basin during the winter and summer seasons (2000-2005), *Remote Sens. Env.*, *107*, doi:10.1016/j.rse.2006.09.026.
- Prasad, A. K., and R. P. Singh (2009), Validation of MODIS Terra, AIRS, NCEP/DOE AMIP-II Reanalysis-2, and AERONET Sun photometer derived integrated precipitable water vapor using ground-based GPS receivers over India, *J. Geophys. Res.*, *114*, D05107, doi:10.1029/2008JD011230.
- Prasad, A. K., R. P. Singh, and M. Kafatos (2006), Influence of coal based thermal power plants on aerosol optical properties in the Indo-Gangetic basin, *Geophys. Res. Lett.*, *33*, L05805, doi: 10.1029/2005GL023801.
- Prasad, A. K., S. Singh, S. S. Chauhan, M. K. Srivastava, R. P. Singh, R. Singh (2007), Aerosol radiative forcing over the Indo-Gangetic plains during major dust storms, *Atmos. Env.*, *41*, doi: 10.1016/j.atmosenv.2007.03.060.
- Qin, Y. and R. M. Mitchell (2009), Characterisation of episodic aerosol types over the Australian continent, *Atmos. Chem. Phys.*, *9*, 1943-1956, doi:10.5194/acp-9-1943-2009.
- Ram, K., M. M. Sarin, and S. N. Tripathi (2010a), Inter-comparison of thermal and optical methods for determination of atmospheric black carbon and attenuation coefficient from an urban location in northern India, *Atmos. Res.*, *97*, doi:10.1016/j.atmosres.2010.04.006.
- Ram, K., M. M. Sarin, and S. N. Tripathi (2010b), A 1 year record of carbonaceous aerosols from an urban site in the Indo-Gangetic Plain: Characterization, sources, and temporal variability, *J. Geophys. Res.*, *115*, D24313, doi:10.1029/2010JD014188.
- Ramanathan, V., and M. V. Ramana (2005), Persistent, Widespread, and Strongly Absorbing Haze Over the Himalayan Foothills and the Indo-Gangetic Plains, *Pure and Appl. Geophys.*, *162*, doi:10.1007/s00024-005-2685-8.

- Ramanathan, V., et al. (2001), Indian Ocean Experiment: An Integrated analysis of the climate forcing and effects of the great Indo-Asian haze, *J. Geophys. Res.*, *106*, 28 371–28 398.
- Ramanathan, V., et al. (2005), Atmospheric brown clouds: Impacts on South Asian climate and hydrological cycle, *PNAS*, *102*, 15, 5326-5333.
- Reddy, M. S., and C. Venkataraman, (2002), Inventory of aerosol and sulphur dioxide emissions from India: I-Fossil fuel combustion, *Atmos. Env.*, *36*, 4, doi: 10.1016/S1352-2310(01)00463-0.
- Reid, J. S., T. F. Eck, S. A. Christopher, P. V. Hobbs, and B. Holben (1999), Use of the Ångström exponent to estimate the variability of optical and physical properties of aging smoke particles in Brazil, *J. Geophys. Res.*, *104*(D22), 27,473–27,489, doi:10.1029/1999JD900833.
- Reid, J. S., et al (2003)., Analysis of measurements of Saharan dust by airborne and ground-based remote sensing methods during the Puerto Rico Dust Experiment (PRIDE), *J. Geophys. Res.*, *108*(D19), 8586, doi:10.1029/2002JD002493.
- Remer, L. A., et al. (2005), The MODIS Aerosol Algorithm, Products, and Validation, *J. of Atmos. Sci. – Special Section*, *62*, 947-973.
- Remer, L. A., et al. (2008), Global aerosol climatology from the MODIS satellite sensors, *J. Geophys. Res.*, *113*, D14S07, doi:10.1029/2007JD009661.
- Remer, L. A., D. Tanre, Y. Kaufman, R. Levy, and S. Mattoo (2009), Algorithm for Remote Sensing of Tropospheric Aerosol From MODIS: Collection 005, Revision 2, Product ID: MOD04/MYD04, Reference Number: ATBD-MOD-96.
- Rolph, G. D. (2010), Real-time Environmental Applications and Display sYstem (READY) Web site (<http://ready.arl.noaa.gov>), NOAA Air Resources Laboratory, Silver Spring, MD.
- Russell, P. B., R. W. Bergstrom, Y. Shinozuka, A. D. Clarke, P. F. DeCarlo, J. L. Jimenez, J. M. Livingston, J. Redemann, O. Dubovik, and A. Strawa (2010a), Absorption Ångström Exponent in AERONET and related data as an indicator of aerosol composition, *Atmos. Chem. Phys.*, *10*, 1155–1169, doi:10.5194/acp-10-1155-2010.
- Russell, P., et al. (2010b), Identifying Aerosol Type from Space: Absorption Ångström Exponent as a Foundation for Multidimensional Specified Clustering and Mahalanobis Classification, Abstract A11E-0091 presented at 2010 Fall Meeting, AGU, San Francisco, Calif., 13-17 Dec.
- Sano, I., S. Mukai, Y. Okada, B. N. Holben, S. Ohta, and T. Takamura (2003), Optical properties of aerosols during APEX and ACE-Asia experiments, *J. Geophys. Res.*, *108*(D23), 8649, doi:10.1029/2002JD003263.

- Satheesh, S. K., K. K. Moorthy (2005), Radiative effects of natural aerosols: A review, *Atmos. Environ.*, *39*, 11, 2089-2110, doi:10.1016/j.atmosenv.2004.12.029.
- Satheesh, S. K., K. K. Moorthy, S. S. Babu, V. Vinoj, V. S. Nair, S. N. Beegum, C. B. S. Dutt, D. P. Alappattu, and P. K. Kunhikrishnan (2009), Vertical structure and horizontal gradients of aerosol extinction coefficients over coastal India inferred from airborne lidar measurements during the Integrated Campaign for Aerosol, Gases and Radiation Budget (ICARB) field campaign, *J. Geophys. Res.*, *114*, D05204, doi:10.1029/2008JD011033.
- Schafer, J. S., T. F. Eck, B. N. Holben, P. Artaxo, and A. F. Duarte (2008), Characterization of the optical properties of atmospheric aerosols in Amazônia from long-term AERONET monitoring (1993–1995 and 1999–2006), *J. Geophys. Res.*, *113*, D04204, doi:10.1029/2007JD009319.
- Schmid, B., K. J. Thome, P. Demoulin, R. Peter, C. Mätzler, and J. Sekler (1996), Comparison of modeled and empirical approaches for retrieving columnar water vapor from solar transmittance measurements in the 0.94- $\mu\text{m}$  region, *J. Geophys. Res.*, 101(D5), doi:10.1029/96JD00337.
- Schmid, B., et al. (2001), Comparison of columnar water-vapor measurements from solar transmittance methods, *Applied Optics*, *40*, 12, doi:10.1364/AO.40.001886.
- Shaw, G. E. (1980), Transport of Asian Desert Aerosol to the Hawaiian Islands, *J. Appl. Met.*, *19*, 1254-1259.
- Shaw, G. E. (1983), Sun Photometry, *Bull. Amer. Met. Soc.*, *64*, 4-10.
- Singh, R. P. (2010), Interactive comment on “Inferring absorbing organic carbon content from AERONET data” by A. Arola et al., *Interactive Comment on Atmos. Chem. Phys. Discuss.*, *10*, 18365.
- Singh, R. P., S. Dey, and B. Holben (2003), Aerosol behavior in Kanpur during Diwali festival, *Curr. Sci.*, *84* (10), 1302-1304.
- Singh, R. P., S. Dey, S. N. Tripathi, V. Tare, and B. Holben (2004), Variability of aerosol parameters over Kanpur, northern India, *J. Geophys. Res.*, *109*, D23206, doi:10.1029/2004JD004966.
- Singh, S., S. Nath, R. Kohli, and R. Singh (2005), Aerosols over Delhi during pre-monsoon months: Characteristics and effects on surface radiative forcing, *Geophys. Res. Lett.*, *32*, L13808, doi:10.1029/2005GL023062.
- Sinyuk, A., et al. (2007): Simultaneous retrieval of aerosol and surface properties from a combination of AERONET and satellite data, *Rem. Sens. of Environ.*, *107*, 1-2, 10.1016/j.rse.2006.07.022.
- Smirnov, A., B. N. Holben, T. F. Eck, O. Dubovik, and I. Slutsker (2000), Cloud-screening and quality control algorithms for the AERONET database, *Remote Sens. Environ.*, *73*, 337–349, doi:10.1016/S0034-4257(00) 00109-7.

- Smirnov, A., B. N. Holben, Y. J. Kaufman, O. Dubovik, T. F. Eck, I. Slutsker, C. Pietras, R. N. Halthore (2002), Optical Properties of Atmospheric Aerosol in Maritime Environments. *J. Atmos. Sci.*, *59*, doi: 10.1175/1520-0469(2002)059<0501:OPOAAI>2.0.CO;2.
- Smirnov, A., B. N. Holben, A. Lyapustin, I. Slutsker, and T. F. Eck (2004), AERONET processing algorithms refinement, paper presented at AERONET Workshop, El Arenosillo, Spain, 10-14 May.
- Smirnov, A., et al. (2009), Maritime Aerosol Network as a component of Aerosol Robotic Network, *J. Geophys. Res.*, *114*, D06204, doi:10.1029/2008JD011257.
- Sokolik, I. N., and O. B. Toon (1999), Incorporation of mineralogical composition into models of the radiative properties of mineral aerosol from UV to IR wavelengths, *J. Geophys. Res.*, *104*(D8), 9423–9444, doi:10.1029/1998JD200048.
- Tanré, D., Y. J. Kaufman, B. N. Holben, B. Chatenet, A. Karnieli, F. Lavenu, L. Blarel, O. Dubovik, L. A. Remer, and A. Smirnov (2001), Climatology of dust aerosol size distribution and optical properties derived from remotely sensed data in the solar spectrum, *J. Geophys. Res.*, *106*(D16), 18,205–18,217, doi:10.1029/2000JD900663.
- Tanré, D., J. Haywood, J. Pelon, J. F. Le´on, B. Chatenet, P. Formenti, P. Francis, P. Goloub, E. J. Highwood, and G. Myhre (2003), Measurement and modeling of the Saharan dust radiative impact: Overview of the Saharan Dust Experiment (SHADE), *J. Geophys. Res.*, *108*(D18), 8574, doi:10.1029/2002JD003273.
- Toledano, C., et al. (2011), Optical properties of aerosol mixtures derived from sun-sky radiometry during SAMUM-2, *Tellus*, Ser. B, *63*, 635–648, doi:10.1111/j.1600-0889.2011.00573.x.
- Tripathi S. N., S. Dey, S. Srivastava, R. P. Singh, and B. N. Holben (2005a), Comparison of MODIS and AERONET derived aerosol optical depth over the Ganga Basin, India, *Annales Geophys.*, *23*, 1093-1101.
- Tripathi, S. N., S. Dey, V. Tare, and S. K. Satheesh (2005b), Aerosol black carbon radiative forcing at an industrial city in northern India, *Geophys. Res. Lett.*, *32*, L08802, doi:10.1029/2005GL022515.
- Tucker, C. J., 1979, Red and photographic infrared linear combinations for monitoring vegetation, *Rem. Sens. Env.*, *8*, 2, 127150, doi:10.1016/0034-4257(79)90013-0.
- Vaughan, M., S. Young, D. Winker, K. Powell, A. Omar, Z. Liu, Y. Hu, and C. Hostetler (2004), Fully automated analysis of space-based lidar data: an overview of the CALIPSO retrieval algorithms and data products, *Proc. SPIE*, *5575*, 16-30.
- Voronoi, G. F. (1908), New parametric applications concerning the theory of quadratic forms - Second announcement, *J. Reine Agnew. Math.*, *134*, 198-287.

Watson, J. G. (2002), Visibility: Science and Regulation, *J. Air Waste Manag. Assoc.*, 52:6, doi:10.1080/10473289.2002.10470813.

Yang, M., S. G. Howell, J. Zhuang, and B. J. Huebert (2009), Attribution of aerosol light absorption to black carbon, brown carbon, and dust in China – interpretations of atmospheric measurements during EAST-AIRE, *Atmos. Chem. Phys.*, 9, doi:10.5194/acp-9-2035-2009.